

INFORMATION TO USERS

This manuscript has been reproduced from the microfilm master. UMI films the text directly from the original or copy submitted. Thus, some thesis and dissertation copies are in typewriter face, while others may be from any type of computer printer.

The quality of this reproduction is dependent upon the quality of the copy submitted. Broken or indistinct print, colored or poor quality illustrations and photographs, print bleedthrough, substandard margins, and improper alignment can adversely affect reproduction.

In the unlikely event that the author did not send UMI a complete manuscript and there are missing pages, these will be noted. Also, if unauthorized copyright material had to be removed, a note will indicate the deletion.

Oversize materials (e.g., maps, drawings, charts) are reproduced by sectioning the original, beginning at the upper left-hand corner and continuing from left to right in equal sections with small overlaps.

Photographs included in the original manuscript have been reproduced xerographically in this copy. Higher quality 6" x 9" black and white photographic prints are available for any photographs or illustrations appearing in this copy for an additional charge. Contact UMI directly to order.

**ProQuest Information and Learning
300 North Zeeb Road, Ann Arbor, MI 48106-1346 USA
800-521-0600**

UMI[®]

**A PHYSICALLY-BASED SNOW MODEL COUPLED TO A
GENERAL CIRCULATION MODEL FOR HYDRO-
CLIMATOLOGICAL STUDIES**

By
Jiming Jin

Copyright © Jiming Jin 2002

A Dissertation Submitted to the Faculty of the
DEPARTMENT OF HYDROLOGY AND WATER RESOURCES

In Partial Fulfillment of the Requirements
For the Degree of

DOCTOR OF PHILOSOPHY
WITH A MAJOR IN HYDROLOGY

In the Graduate College

THE UNIVERSITY OF ARIZONA

2002

UMI Number: 3050315

**Copyright 2002 by
Jin, Jiming**

All rights reserved.

UMI[®]

UMI Microform 3050315

**Copyright 2002 by ProQuest Information and Learning Company.
All rights reserved. This microform edition is protected against
unauthorized copying under Title 17, United States Code.**

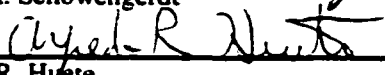
**ProQuest Information and Learning Company
300 North Zeeb Road
P.O. Box 1346
Ann Arbor, MI 48106-1346**

THE UNIVERSITY OF ARIZONA ©
GRADUATE COLLEGE

As members of the Final Examination Committee, we certify that we have read the dissertation prepared by JIMING JIN

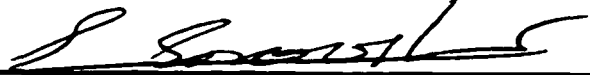
entitled A PHYSICALLY-BASED SNOW MODEL COUPLED TO A GENERAL
CIRCULATION MODEL FOR HYDRO-CLIMATOLOGICAL STUDIES

and recommend that it be accepted as fulfilling the dissertation requirement for the Degree of Doctor of Philosophy

 _____	<u>4/1/02</u> Date
Dr. Soroosh Sorooshian	
 _____	<u>4/1/02</u> Date
Dr. Xiaogang Gao	
 _____	<u>04-01-02</u> Date
Dr. Roger C. Bales	
 _____	<u>4/01/02</u> Date
Dr. Robert A. Schowengerdt	
 _____	<u>4/1/02</u> Date
Dr. Alfredo R. Huete	

Final approval and acceptance of this dissertation is contingent upon the candidate's submission of the final copy of the dissertation to the Graduate College.

I hereby certify that I have read this dissertation prepared under my direction and recommend that it be accepted as fulfilling the dissertation requirement.



Dissertation Director
Dr. Soroosh Sorooshian

4/1/02
Date

STATEMENT BY AUTHOR

This dissertation has been submitted in partial fulfillment of requirements for an advanced degree at The University of Arizona and is deposited in the University Library to be made available to borrowers under rules of the Library.

Brief quotations from this dissertation are allowable without special permission, provided that accurate acknowledgment of source is made. Requests for permission for extended quotation from or reproduction of this manuscript in whole or in part may be granted by the copyright holder.

SIGNED: Jiming Jin

ACKNOWLEDGEMENTS

This dissertation could not be completed without the long-term support from many institutions and persons when I was studying in the University of Arizona, first as a visiting student and then, as a Ph.D. student. I am grateful to the awards of the John W. Harshbarger fellowship (8/1997-7/1999) from the World Laboratory in Lausanne, Switzerland and the research assistantship (8/1999-5/2002) of NASA/EOS Interdisciplinary Research Program (NAG5-3640 and NAG NAG5-11044).

I must thank my primary advisor Professor Soroosh Sorooshian who always encouraged me to pursue my ideas. His unparalleled expertise and unmatched wisdom guided me through my dissertation research. I would like to thank my co-advisor Dr. Xiaogang Gao for his unceasing guidance and continual commitment to this work. I thank Professor Roger C. Bales for his innumerable suggestions, advice, and thoughts and Professor Robert A. Schowengerdt and Professor Alfredo R. Huete for their valuable remote-sensing knowledge and creative insights.

I would like to thank Dr. Zong-Liang Yang, Dr. Yongkang Xue, Dr. Kuolin Hsu, and Dr. Qi Hu for sharing their thoughtful insights and knowledge. I also thank Dr. Hoshin Gupta and Dr. Bisher Imam for their suggestions and advice. Special thanks go to my previous advisors Dr. Guoxiong Wu and Dr. Shufen Sun for their continual encouragement and support.

I appreciate the assistance of Dr. Qingyun Duan and Ms. Yuqiong Liu in setting up the SCE automatic calibration algorithm. Next thanks go to Dr. Martyn Clark for providing me the snowcourse data. I thank Dr. Andrea Hahmann for her assistance in NCL and numberless discussions. I also want to thank Dr. Bart Nijssen and Ms. Laura C. Bowling for permitting me to use the PILPS2e figures.

I would like to thank my friends and colleagues Weiping Li, Guoyue Niu, Han Yi, Shunli Zhang, Yang Hong, Shayesteh E. Mahani, Steven Fassnacht, Quanfu Fan, Huiling Yuan, Feyzan Misirli, Kristie Franz, Jialun Li, Thomas Pagano, Terri Sue Hogue, Holly Hartmann, and Newsha Khodatalab for their assistance and friendship.

Particularly, I thank Dan Braithwaite and Jim Broermann for their patient and consistent computer assistance, Corrie Thies and Terrie Thompson for their kindness and administrative support, and Ralph R. Ramsey for his friendship and help in my English. I owe special thanks to Cas Sprout for her kindness and assistance in my dissertation writing.

I wish to thank my wife, Jingli Dong, for her love, enduring patience, sacrifices, and support. I would like to thank my parents, sisters, and parents-in-law for their tremendous love and unselfish acts of kindness.

TABLE OF CONTENTS

LIST OF TABLES	8
LIST OF ILLUSTRATIONS	9
ABSTRACT	12
1. INTRODUCTION	14
1.1 Role of snowpack in hydrological cycle	15
1.1.1 Evaporation and sublimation.....	15
1.1.2 Runoff.....	16
1.1.3 Soil moisture and groundwater recharge.....	16
1.1.4 Precipitation	18
1.2 Role of snowpack in climate	18
1.2.1 Interactions between snow and climate.....	18
1.2.2 Effects of global warming on snow cover.....	20
1.2.3 Relationship between ENSO and snow cover.....	21
1.3 Overview of snow models.....	23
1.4 Problem statement and objectives.....	27
2. SNOW-ATMOSPHERE-SOIL TRANSFER MODEL FOR VEGETATED SURFACES.....	31
2.1. Introduction.....	31
2.2. Development of SAST Model.....	33
2.2.1 Mass Conservation (Continuity) Equation in SAST	37
2.2.2 Energy Conservation Equation in SAST.....	38
2.3 SAST Model Evaluation	43
2.3.1 French Data Set	43
2.3.2 BOREAS Data Set.....	47
2.4 Discussions.....	52
2.5 Conclusion	53
3. IMPACTS OF MODEL CALIBRATION ON HIGH-LATITUDE LAND-SURFACE PROCESSES.....	55
3.1. Introduction.....	55
3.2 Model Description.....	58
3.3 Uncalibrated Results	60
3.4 Calibrated Results	66
3.4.1 Calibrated Parameters.....	66
3.4.2 Calibrated Runoff.....	69
3.4.3 Vegetation Cover.....	71
3.4.4 Vegetation Roughness Height.....	74
3.4.5 Soil Moisture	76

TABLE OF CONTENTS – *Continued*

3.5	Overall evaluation of SAST model in PILPS2e experiments	78
3.6	Discussion and Conclusion	84
4.	ASSIMILATION OF REMOTELY SENSED SNOW DEPTH IN GCM OVER THE ROCKY MOUNTAINS	87
4.1	Introduction	87
4.2	Model	89
4.3	Data and Methodology	90
4.4	Results	94
	4.4.1 Geographic distribution of the difference between simulated and observed snow depth over North America	94
	4.4.2 Surface air temperature at 2 m	95
	4.4.3 Energy balance	98
	4.4.4 Precipitation	102
	4.4.4.1 Variations of seasonal precipitation	102
	4.4.4.2 Geographic distribution of precipitation	104
4.5	Conclusions and discussions	109
5.	CORRELATION BETWEEN SNOWPACK IN THE WESTERN U.S. AND TROPICAL PACIFIC SST	112
5.1	Introduction	112
5.2	Model	115
5.3	Data	116
5.4	Results	118
	5.4.1 Relationship between snow depth in the western U.S. and tropical Pacific SST	118
	5.4.2 SST anomaly patterns corresponding to the SWE anomalies in the western U.S.	119
	5.4.3 500 mb geopotential height anomalies during the years of anomalous snow in the western U.S.	123
	5.4.3.1 NWA and NWB	126
	5.4.3.2 SWA and SWB	127
	5.4.4 500 mb wind field anomalies during the periods of anomalous snow in the western U.S.	128
	5.4.4.1 NWA and NWB	128
	5.4.4.2 SWA and SWB	132
	5.4.5 Precipitation and temperature	133
	5.4.5.1 NWA and NWB	136
	5.4.5.2 SWA and SWB	138
5.5	Discussions and conclusions	141
6.	CONCLUSIONS	144

TABLE OF CONTENTS – *Continued*

APPENDICES.....	148
APPENDIX A. Surface albedo formulations	149
APPENDIX B. Nomenclature.....	145
APPENDIX C. Publications.	152
REFERENCES.....	153

LIST OF TABLES

<u>Table</u>	<u>Page</u>
Table 1.1 Comparison of several snow models.....	25
Table 2.1 Three snow compaction processes in SAST.....	37
Table 2.2 Calculations for the right-hand terms in the governing equations and boundary equations in SAST.....	42
Table 2.3 Snow surface fluxes in SAST	43
Table 2.4 Parameters of soil and vegetation in SAST (Dickinson et al. 1993).....	44
Table 3.1 List of selected parameters and their ranges for calibration (F = Forest region, M = Mountain region).....	64
Table 3.2 Optimized parameters obtained through the SCE automatic calibration method...	66
Table 4.1 The seasonal biases between model output and observations for both runs (unit: °C) and CTR is control run and ASS is assimilation run.	96
Table 5.1 Anomalies of Niño-3.4 SST.....	120
Table 5.2 Sample numbers for the NWA, NWB, SWA, and SWB cases.....	122

LIST OF ILLUSTRATIONS

<u>Figure</u>	<u>Page</u>
Figure 2.1 Concept illustration of snow, vegetation, and soil and their fractional coverage in a grid square in the SAST model.....	36
Figure 2.2 Determination among H , f_{ice} , and T in an ice-liquid water system in the SAST model	39
Figure 2.3, Comparison of snow depth and skin temperature from the SAST model output with observations in the grassland at Col de Porte, France.....	44
Figure 2.4 Comparison of snow surface temperature and skin temperature from the SAST model output with observations at Col de Porte, France.....	46
Figure 2.5 Comparison of snow surface albedo and surface albedo from the SAST model output with observations at Col de Porte, France.....	46
Figure 2.6 Comparison of (a) snow depth and (b) surface net radiation from the SAST model output with observations, (c) observed air temperature, and (d) observed snowfall snow in old aspen region of SSA at Boreal, Canada	48
Figure 2.7 SAST model output: (a) Net heat flux for open area snow and under canopy snow, and (b) fraction of vegetation under canopy snow and open area snow in old aspen region of SSA at Boreal, Canada.	50
Figure 2.8 SAST model output: (a) Modeled skin temperature and observations and (b) surface turbulent fluxes in old aspen region of SSA at Boreal, Canada.	51
Figure 2.9 Deposition of surface energy fluxes into vegetation, snow, and bare soil contributions. SAST model output: (a) sensible heat flux, (b) latent heat flux, and (c) fractional coverage of vegetation, snow, and bare soil.	52
Figure 3.1 Comparison of daily and monthly runoff predicted by the uncalibrated SAST scheme with the observation during 1989-1990, for the forest sub-basin (a, b and c) and mountain sub-basin (d, e, and f)	62
Figure 3.2 Comparison of daily runoff predicted by the calibrated SAST scheme with observations during 1989-1990 for (a) the forest sub-basin and (b) the mountain sub-basin	68
Figure 3.3 Comparison of 10-year runoff predicted by the uncalibrated and calibrated SAST scheme with observations for the forest sub-basin (a) uncalibrated and (b) calibrated, for the mountain sub-basin (c) uncalibrated and (d) calibrated.....	70
Figure 3.4 Comparison of the calibration results of (a) runoff, (b) SWE, and (c) snowmelt (1989-1990) with the sensitivity results with vegetation coverage reduced from the calibrated values to the BATS values for the forest sub-basin	73
Figure 3.5 Comparison of the calibration results of the major energy components on snow surface: (a) net solar radiation, (b) net long wave radiation (positive for downward flux), and (c) net sensible heat flux (positive for upward flux) for the forest sub-basin (1989-1990)	74

LIST of ILLUSTRATIONS – *Continued*

Figure 3.6 Comparison of the calibration results of (a) runoff, (b) SWE, (c) snowmelt, and (d) net sensible heat flux on snow surface with the sensitivity results with vegetation roughness height reduced from the calibrated values to the BATS values for the forest sub-basin.....	75
Figure 3.7 Comparison of 10-year soil-moisture variations predicted by the SAST and VISA models: (a) top soil layer (0-0.1 m depth), (b) root zone layer (0-1 m depth), and (c) total layer (0-5 m).	76
Figure 3.8 Mean monthly observed (dots) and simulated (lines) discharge for the Kalix and Torne river basins (Nijssen et al. 2002).....	80
Figure 3.9 Flow duration curves based observed (dots) and simulated (lines) daily flows from 1989-1998 (Nijssen et al. 2002)	81
Figure 3.10 Talor diagram of daily flows from 1989-1998. Upper-case letters represent flows at the mouth of the Kalix, lower-case letters represent flows at the mouth of the Torne (Nijssen et al. 2002).....	82
Figure 3.11 Mean annual basin-wide turbulent heat fluxes. The dashed line shows the water balance based estimate of the latent heat flux over the basin (Nijssen et al. 2002).....	83
Figure 4.1 Area for the assimilation of snow depth in CCM3 over the Rocky Mountains....	93
Figure 4.2 Differences in snow depth between CCM3 output and SMMR data over North America (model output minus SMMR data).....	93
Figure 4.3 Surface air temperature differences between CCM3 output and observations before (solid line) and after (dashed line) snow depth assimilation (CCM3 output minus observations).....	95
Figure 4.4 Differences between components in energy balance equation from the assimilation and control runs (assimilation minus control), a) solar (solid line), long-wave (dashed line), and net (dotted line) radiations, b) sensible (solid line), latent (dashed line) heat fluxes, and sensible plus latent (dotted line) heat fluxes, and c) ground flux to soil	97
Figure 4.5 (a) Differences of vegetation and cloud fraction and albedo between the assimilation and control runs (assimilation minus control); (b) comparison of soil moisture from NCEP reanalysis data (dotted line), CCM3 control (solid line), and assimilation (dashed line) runs	98
Figure 4.6 Comparison of monthly precipitation from CCM3 control (solid line) and assimilation (dashed line) runs and observations (dotted line)	103
Figure 4.7 Geographic distributions of precipitation differences between CCM3 control run and observations in (a) winter and (b) summer and between CCM3 control and assimilation runs in (c) winter and (d) summer.....	104
Figure 4.8 500 mb height differences between CCM3 output and NCEP reanalysis data averaged over (a) December, January, and (b) February and June, July, and August, respectively.....	105
Figure 4.9 Downward solar radiation (thick lines) and SWE (thin lines) from CCM3 control (solid lines) and assimilation (dashed lines) runs	109

LIST of ILLUSTRATIONS – *Continued*

Figure 5.1 Correlation coefficients between Niño-3.4 SST and (a) SWEs from CCM3 output and (b) observed snowcourse data in western U.S. Values in stippled areas pass the 95% significance Student's <i>t</i> test.....	118
Figure 5.2 SST anomalies during the years of (a) NWA, (b) NWB, (c) SWA, and (d) SWB. Stippled areas pass the 90% significance Student's <i>t</i> test.....	121
Figure 5.3 Simulated 500 mb height anomalies during the years of (a) NWA, (b) NWB, (c) SWA, and (d) SWB. Stippled areas pass the 90% significance Student's <i>t</i> test.....	124
Figure 5.4 Observed 500 mb height anomalies during the years of (a) NWA, (b) NWB, (c) SWA, and (d) SWB. Stippled areas pass the 90% significance Student's <i>t</i> test.....	125
Figure 5.5 Simulated 500 mb wind and temperature anomalies during the years of (a) NWA, (b) NWB, (c) SWA, and (d) SWB. Stippled areas pass the 90% significance Student's <i>t</i> test.....	130
Figure 5.6 Observed 500 mb wind and temperature anomalies during the years of (a) NWA, (b) NWB, (c) SWA, and (d) SWB. Stippled areas pass the 90% significance Student's <i>t</i> test.....	131
Figure 5.7 Simulated precipitation anomalies during the years of (a) NWA, (b) NWB, (c) SWA, and (d) SWB. Stippled areas pass the 90% significance Student's <i>t</i> test.....	134
Figure 5.8 Observed precipitation anomalies during the years of (a) NWA, (b) NWB, (c) SWA, and (d) SWB. Stippled areas pass the 90% significance Student's <i>t</i> test.....	135
Figure 5.9 Simulated temperature anomalies during the years of (a) NWA and (b) NWB. Stippled areas pass the 90% significanc Student's <i>t</i> test.....	136
Figure 5.10 Comparison of precipitation anomalies from CCM3 output, observations from Climate Research Unit (CRU), United Kingdom, and NCEP reanalysis data.	139

ABSTRACT

A Snow-Atmosphere-Soil Transfer (SAST) model has been developed to extend the point snowmelt model to vegetated areas using the parameterization concepts of the Biosphere-Atmosphere Transfer Scheme (Dickinson et al. 1993). The model applications for short-grass and forest fields show that the simulated surface temperature, albedo, and snow depth have close agreement with observations. In addition, because of biases in simulated runoff in the high-latitudes, a Shuffled Complex Evolution (Sorooshian et al. 1993) scheme for automatic calibration has been connected with the SAST model to determine the realistic distribution of runoff components from different soil layers and search the optimized parameter set. The calibrated runoff closely matches observations.

Because the Community Climate Model version 3 (CCM3) coupled with the SAST model overestimates snow depth and precipitation and underestimates surface temperature over the Rocky Mountains, remotely sensed snow depth data have been assimilated in the model to alleviate model discrepancies based on energy and mass balances. The improved surface temperature simulations result from the decreased snowmelt and albedo in winter and spring and from the weakened evaporation in summer due to drier soil. Meanwhile, modeled summer precipitation over the Rocky Mountains has a minor improvement.

The relationship between the variations of tropical Pacific SST and snowpack anomalies in the western United States (U.S.) has been studied by comparing observations and CCM3 output. The results indicate that in the northwestern U.S., the

warm tropical Pacific phase of the El Niño-Southern Oscillation (ENSO) is associated with diminished snowpack while its cool phase is related to enhanced snowpack. This relationship is largely determined by winter precipitation variability for the observations; however, it relies heavily on the variations of temperature due to the biases in atmospheric patterns for the model output. In the southwestern U.S., positive snowpack anomalies for both observations and simulations result from the strong warm phase of the ENSO and negative ones are connected with exaggerated local precipitation in fall.

1. INTRODUCTION

Snow plays an important role in regional water resources and global climate because of its special properties different from other land types. Cohen (1994) summarized snow properties in five ways. (i) The high surface reflectance of snow, ranging from 30% to 90%, greatly reduces solar radiation absorption at the surface and lowers the surface temperature. (ii) Due to its saturated surface, snow supplies water vapor to the atmosphere through sublimation and evaporation. Meanwhile, snowmelt is an important source of soil moisture, groundwater recharge, and the river system water. (iii) The low thermal conductivity of snow prevents heat content stored in the ground from being released to the overlying atmosphere through long-wave radiation. McFadden and Ragotzkie (1967) have estimated that the temperature of the soil surface with snow is 1.6°C higher than that without snow. (iv) The phase changes of snow usually consume tremendous energy. For example, at 0° C, 334,000 Joules of energy are needed to melt 1 kg of snow and 2,834,000 Joules are used for evaporating the same amount of snow (Cohen and Rind 1991). (v) Snow has a higher thermal emissivity than most other natural surfaces, which tends to amplify outgoing long-wave radiation at the snow surface and thus, decrease surface temperature (Wagner 1973). These special properties of snow are believed to have an impact on climate variability and affect water resources.

1.1 Role of snowpack in hydrological cycle

The hydrological cycle is composed of evaporation, sublimation, runoff, soil moisture, groundwater recharge, and precipitation. Snow variability is a significant contributor to the variations of these components.

1.1.1 Evaporation and sublimation

Evaporation of the snow surface is the phase change from liquid water to water vapor. This usually takes effect during the snowmelt season, when melting snow produces significant liquid water. Because higher surface reflectance and stronger thermal emission reduce the absorption of net radiation, the snow surface often has a low temperature, which usually suppresses evaporation. However, when snow is melting in spring, the liquid water increases the soil moisture leading to strong evaporation, although the surface temperature is still cold (around 0° C).

Sublimation indicates the phase change from solid ice to water vapor and occurs during the entire snow season. A recent study by Bowling et al. (2002) suggests that, model-predicted winter snow sublimation significantly affects snow accumulation when a large number of land-surface models were compared. They found that in the high latitudes the models with higher rates of sublimation predicted thinner snow water equivalent (SWE), which resulted in lower annual runoff on a watershed scale. However, this conclusion still needs a further investigation using observed evidence. The importance of snow sublimation in the hydrological cycle, therefore, can not be clearly seen.

1.1.2 Runoff

Snow plays a significant role in affecting annual runoff. In the western United States (U.S.), 75% - 80% of the annual discharge of most of the major streams is from melting mountain snowpack (Palmer 1988) because 50%-70% of the annual precipitation falls as snow and is largely stored through the winter season in the region (Serreze et al. 1999). Bowling et al. (2002) and Nijssen et al. (2002) also indicate that melting snow water is a major source of annual runoff in high latitude regions. Thus, the amount of snow mass will seriously affect the water management in areas where melting snow water is an important water resource. For example, el-Ashry and Gibbons (1988) indicate that due to the contraction of the snow cover and the growing water demand, the lower Colorado River Basin may not supply sufficient water for human use and economic development in a dry period. On the other hand, a surplus of snow mass has a potential to cause severe flooding and property damages. In spring 1983, flooding of the lower Colorado River Basin resulted in \$80 million in economic losses (Rhodes et al. 1984).

1.1.3 Soil moisture and groundwater recharge

In seasonal snow covered areas, soil moisture is heavily affected by snowmelt. Except for water evaporating back to the atmosphere from the surface, almost all other snowmelt water infiltrates the soil to become soil moisture. Eventually, the water in the soil percolates to the deep soil layer and forms groundwater, evaporates to the atmosphere from the soil and/or from vegetation transpiration, or is directly used by vegetation. Soil moisture is vitally important in both supporting agricultural production

and defining natural vegetative type and extent. Any changes in climate, such as the alteration of precipitation patterns or the evapotranspiration regime, will directly affect soil-moisture storage, runoff, and ground recharge dynamics. In the Sacramento Basin in northern California, a study identified reductions in summer soil moisture of 30% or more because of a decrease in winter and spring snow mass caused by the warmer climate (Gleick 1986, 1987a,b).

Groundwater accounted for 22% of the total U.S. freshwater withdrawals in 1995 (Solley et al. 1998). In some areas, current levels of groundwater use are already unsustainable. For example, declining aquifer levels and higher pumping lifts have increased water costs in the southern High Plains, leading farmers to remove millions of acres from production in recent decades. Groundwater overdrafts in California in the drier years of the 1990s averaged nearly 1.5 million acre-feet per year (California Department of Water Resources 1998). In some semi-arid or arid regions such as the western U.S., the amount of snow mass is a critical factor for sustaining the groundwater level because snow is the main water source for groundwater recharge. Thus, groundwater level is dependent on snowpack variability in these regions. Panagoulia and Dimou (1996) indicate that the temperature-induced changes in snowfall and snowmelt patterns greatly impact the groundwater-streamflow interactions over a mountainous basin in central Greece during spring and summer months.

1.1.4 Precipitation

Precipitation is a very difficult variable to predict in climate, weather, and hydrological studies. It can be divided into convective and large-scale precipitations. The snowpack results in a colder land surface, leads to a more stable atmospheric column, and reduces convective precipitation. At same time, because the water vapor in the atmospheric column is easier to condense due to the snow surface cooling process, large-scale precipitation, which occurs under conditions of a stable atmospheric column, may increase. Since the increase in large-scale precipitation is often greater than the decrease in convective precipitation, net total precipitation will increase. Snowpack is also a source of winter air moisture which leads to stronger precipitation. The increased precipitation will further amplify the snow mass on the ground when precipitation falls as snow. Thus, snowpack has positive correlations with the precipitation (McCabe and Wolock 1999).

1.2 Role of snowpack in climate

1.2.1 Interactions between snow and climate

Snow cover causes the largest variations in surface conditions, both spatially and temporally. Its high albedo reflects a large amount of solar radiation and leads to lower surface temperatures. The colder surface cools the atmospheric column, strengthens water vapor condensation, and increases cloud fraction. The larger cloud fraction can block solar radiation to the surface and also increases downward long-wave radiation. Meanwhile, the cooled atmospheric column emits less long-wave radiation to the surface.

The net downward long-wave radiation usually decreases because temperature exerts stronger effects on the long-wave radiation. Thus, the net radiation at the surface will decrease and further lower the surface temperature, which indicates that the snowpack produces a positive feedback to the atmosphere. Namias (1985) and Klein (1985) indicate that the snow cover results in a 5 ° C decrease in surface temperature based on observed evidence. A modeling study performed by Walsh and Ross (1988) shows that snow cover could cause a 10° C decrease in surface temperature; however, Cohen and Rind (1991) obtained a 1-2° C decrease in surface temperature caused by snow cover in their model.

Extensive snow cover seriously affects the atmospheric patterns. Lamb (1972) pointed out that snow cover leads to contraction of the atmospheric layer. He found that the thickness of the atmospheric layer from 1000 to 500 mb is meaningfully smaller over snow-covered surfaces. Contraction of the atmospheric layer will produce or maintain a cold trough due to the snow cover's cooling processes. On the west side of the trough, the prevailing northerlies or northwesterlies contribute cold air to the trough and cause intensification of the trough (Lamb 1972). Namias (1964) indicates that a lack of snow cover causes a rapid increase in surface temperature, reinforcing the temperature gradient between ocean and continent. The amplified temperature gradient can result in a blocking pattern or sustain an existing blocking over land near a cold ocean.

Snow cover has a strong correlation with summer monsoon rainfall (Hahn and Shukla 1976; Wu et al.1993). As mentioned above, snow cover commonly strengthens the density of the overlying atmosphere by cooling. The dense atmospheric layer related to stronger sea level pressures inhibits monsoon circulation, which favors weaker sea

level pressures. Hahn and Shukla (1976) pointed out that the Asian summer monsoon rainfall is negatively correlated with Eurasian snow cover based on observations. A modeling study by Wu et al. (1993) showed that the timing of snowmelt on the Tibetan Plateau impacts the onset of the summer monsoon. They found that an earlier-than-normal snow melting in the region leads to an earlier monsoon onset and gives rise to a drier and warmer climate in southern China; conversely, a later snow melting postpones the start of the Asian summer monsoon and results in a moister and colder climate in southern China.

1.2.2. Effects of global warming on snow cover

The effect of global warming on snow cover is a disputed issue in climate studies. The conventional standpoint is that snow feedback is expected to amplify the global warming caused by increasing concentrations of atmospheric greenhouse gases. The warmer climate will contribute to smaller snow cover, resulting in a darker land surface that absorbs more solar radiation and leads to less snow cover. However, Cess et al. (1991) intercompared 17 General Circulation Models (GCMs) and found that some models had a strong positive feedback while others had a weak negative one due to an artificial increase of sea surface temperature (SST). The additional amplification or moderation may be caused by both cloud interactions and long-wave radiation, contrary to conventional explanations.

A recent study by McCabe and Wolock (1999) showed that both Canadian and Hadley GCMs produce large decreases in April 1 snowpack for all snow sites in the

western U.S. because of the warming, with the exception of the central Rocky Mountain region in the Hadley model where increases in temperature still did not force winter temperatures above the freezing point. In some of the more extreme cases, model snowpack is completely eliminated by the end of this century.

The results from McCabe and Wolock (1999) are similar to those obtained by Hamlet and Lettenmaier (1999) for the Columbia River basin. Hamlet and Lettenmaier used a regional hydrological model driven by GCM climate output and found that by 2045, the spring snowpack will be substantially reduced because of higher temperatures. Overall, the timing of runoff peaks shifts dramatically from spring to winter, with increases of about 50%, followed by decreases in spring and summer runoff. By 2095, the Hadley climate model suggests that the Columbia River basin will no longer be dominated by snowmelt dynamics.

However, these studies are based on GCM output and have not been validated with observational data. The application of remote-sensing data has alleviated the problem, but it is still not sufficient due to the short time series of data.

1.2.3 Relationship between ENSO and snow cover

The anomalies of snow cover are often related to variations in climate pattern due to their influences on temperature and precipitation. The El Niño-Southern Oscillation (ENSO) is a significant factor affecting climate variability (Redmond and Koch 1991; Cayan and Webb 1992) and is believed to affect snow cover. Their studies indicate that the warm tropical Pacific phase of ENSO during the Northern Hemisphere winter is

associated with diminished snow cover and streamflow in the northwestern U.S. and enhanced snow cover and streamflow in the southwestern U.S. Cayan (1996) used the winter Southern Oscillation Index (SOI) as a measure of ENSO to study its association with anomalies of the snowpack in the western U.S. He found that the negative SOI (warm Tropics) yields a strong negative anomalous snowpack in the northern Rocky Mountains, and a weak positive anomalous snowpack in Utah and southern Colorado. The opposite behavior was found during the cool phase of ENSO. Clark et al. (2001) examined the influence of ENSO in the tropical Pacific Ocean on the seasonal snowpack evolution in the Columbia and Colorado River basins. They found significant effects of ENSO on the seasonal snowpack evolution for various parts of these basins and used this information to predict annual runoff. The predictions exhibited only modest accuracy when based solely on El Niño or La Niña conditions. At almost all sites, predictions based on antecedent snowpack accumulations were more reliable than those based on the ENSO information alone. However, combining observations of mid-winter snowpack conditions with the ENSO indices improved predictions for those basins in which the ENSO signals exhibit strong seasonality. McCabe and Dettinger (2001) indicate that the climate pattern associated with snowpack anomalies in the northwestern U.S. is different from that related to snowpack anomalies in the southwestern U.S. during the ENSO, which implies that the varying amplitude of the ENSO cycle probably affects the distribution of snowpack anomalies in the western U.S.

Tropical Pacific SST anomalies and snowpack variations in the western U.S. are connected through the anomalies of midlatitude atmospheric circulation. Clark et al.

(2001) found that the ENSO exerted influence on the snowpack in the western U.S. through drifted midlatitude circulation. Therefore, in order to understand the relationship between the ENSO and snowpack in the western U.S., the mechanisms of the ENSO on the midlatitude atmospheric pattern should first be investigated. Lau and Nath (1994) performed GCM experiments to investigate the effects of tropical Pacific SST variations on midlatitude atmosphere. They found that the model could reproduce the Pacific-North-America (PNA) circulation patterns (Barnston and Liveszey 1987) only when forced by strong tropical Pacific SST anomalies during El Niño. The extratropical SST anomalies had minor effects on the midlatitude climate circulation patterns (Lau and Nath 1994, 1996, and 2001). Some observational (Horel and Wallace 1981; among others) and modeling studies (Sardeshmukh and Hoskins 1988; among others) also found a strong relationship between tropical Pacific SST anomalies and midlatitude atmosphere. Therefore, ENSO-induced anomalies of atmospheric patterns can lead to temporal and spatial variations of snowpack in the western U.S., which is investigated in Chapter 5 through comparison of GCM output and observations.

1.3 Overview of snow models

Various snow models have been developed for decades to improve snow studies. A snow model built by Anderson (1976) includes the most advanced snow hydrology research of that time. Based on Anderson's model, Jordan (1991) developed a one-dimensional thermodynamic snow model (SNTHERM), primarily to predict the snow surface temperature. This model is one of the most sophisticated snow models to date and

includes detailed processes of snow physics. Its parameterization schemes, such as snow density calculation, solar radiation transfer within the snowpack, snow grain size estimation, etc., have been adopted by many other snow models (Jin et al. 1999a; Loth et al. 1993; Dai et al. 2001). Jordan's model and many others with similar structures and physics (Anderson 1976; Morris 1982; Kondo and Yamazaki 1990) are usually used for watershed runoff and/or weather prediction. It is difficult for them to be used in climate studies because of the considerable computation cost and numerical instability. Meanwhile, vegetation dynamics is not considered in these models. Dickinson et al. (1993) developed a snow sub-model in the Biosphere-Atmosphere Transfer Scheme (BATS). This model is accurate for large-scale applications in climate models (Yang et al. 1999). However, it produces some bias for point applications (Jin et al. 1999b) due to its simple model structure and neglects some important physical processes. Similar models were developed by Bonan (1996) and Tarboton and Luce (1996). Some sophisticated snow models at an intermediate level of complexity have been developed by Loth et al. (1993), Lynch-Stieglitz (1994), Jin et al. (1999b), and Dai et al. (2001). These models are designed for extensive applications in hydrology, weather, and climate. The comparison of some representative snow models are shown in Table 1.1.

Table 1.1 Comparison of several snow models.

Model developer Name/host GCM	Physical Equations	Water Phases	Layering	Liquid Water Treatment	Snow Density
Jordan (1991) SNTHERM/No GCM (U.S.A.)	Energy-mass balance	Ice Liquid water Vapor	Multi- layers	Gravitational flow	Function of mass balance and compaction
Loth (1993) /ECHAM (Germany)	Energy-mass balance	Ice Liquid water Vapor Dry air	2-5 layers	Liquid water- holding capacity as function of snow density	Function of mass balance and compaction
Sun et al. (1999) Jin et al. (1999a) SAST/GOALS (China)	Energy-mass balance	Ice Liquid water	3 layers	Liquid water- holding capacity as function of snow density	Function of mass balance and compaction
Lynch-Stieglitz (1994) GISS-LS/GISS (U.S.A)	Energy-mass balance	Ice Liquid water	3 layers	Constant liquid water- holding capacity	Function of snow age
Verseghy (1991) CLASS/CCC (Canada)	Surface energy balance for snowmelt Mass balance for SWE change Energy balance for no- melting temperature	Ice Liquid water	1 layer	Constant liquid water- holding capacity	Function of snow age
Bonan (1996) LSM/CCM3(U.S.A)	Surface energy balance for snow melt Mass balance for SWE change Energy balance for no- melting temperature	Ice	1 layer	No	Constant
Dickinson et al. (1993), BATS/CCM2,3 (U.S.A) Sellers et al. (1986) SiB/GFDL (U.S.A) Pitman et al. (1991) BEST/BMRC (Australia)	Surface energy balance for snow melt Mass balance for SWE change Force-restore for no-melting temperature	Ice	2 snow- soil composite layers	No	Function of snow age in BATS Const. in SiB and BEST

The one-dimensional SNTHERM model (Jordan 1991) was developed for predicting properties and processes within strata of snow and frozen soil. The model uses a mixture theory to describe the dynamic and thermal processes of five mixture constituents: dry air, dry soil, and the three phases of water. Snowmelt is assumed to drain by gravity, and water vapor is assumed to move along the temperature gradient.

Water and energy exchanges at the surface and bottom of a snowpack and internal snow processes such as ice grain growth, snow ablation, densification, and metamorphosis are modeled through the numerical solution of mass and heat-transfer equations. To simulate such detailed physics, SNTHERM uses a large number of snow layers and executes calculations at short time steps (5-900 seconds). Because vegetation influences and spatial distribution of snow are not considered in SNTHERM, the model conceptually applies to snowpack overlying bare soil.

Compared to SNTHERM, the BATS snow submodel (Dickinson et al. 1993; Yang et al. 1997) is a greatly simplified approach designed for use in GCMs that focus on long-term climate. In BATS, snow is lumped into a single uniform layer that lies over homogeneous soil, and the extended force-restore method (Dickinson, 1988) is used to calculate surface temperature (at a depth subject to diurnal variation) and subsurface temperature (at a depth subject to seasonal variation) for the composite snow and soil layer. Snowmelt is estimated using an energy balance for surface snow. Internal radiative and thermodynamic snowpack processes are omitted; key snowpack properties such as surface albedo, ice-grain size, and snow density are parameterized as functions of surface snow age. Vegetation effects on snow cover and subgrid snow fractional coverage over various land-surface types are modeled in order to realistically represent snow processes over a large-scale ($\sim 2.8^\circ \times 2.8^\circ$) grid.

The Snow-Atmosphere-Soil Transfer (SAST) model (Sun et al., 1999; Jin et al., 1999b) is one of multiple efforts to simplify SNTHERM to a point where it can be used to describe the variation of snow cover for a wide region, especially for both long-term

and short-term atmosphere modeling (Loth et al., 1993; Lynch-Stieglitz, 1994). In the model, dry air and water vapor components in snowpack are neglected. The gravitational flow of meltwater is replaced by the concept of water-holding capacity: meltwater in a layer will remain there until it exceeds the layer's holding capacity; after that, the excess is delivered to the lower layer. With both ice and liquid water phases in a snowpack, the three snow compaction processes of SNTHERM (metamorphism, weight, and melting-refreezing) are retained in SAST to simulate the variability of snow density. Because SAST neglects the vapor phase, ice-grain size is parameterized as a function of snow density. In SAST, only three layers are used to describe a snowpack. The top two layers are within 20 cm below the snow surface to simulate density, temperature gradients, and snowmelt; the third layer represents the remaining body of the snowpack. When solving the energy equation, SAST uses heat content as a prognostic variable instead of snow temperature. By assuming that 0° C water possesses zero heat content, this approach can simplify the representation of meltwater and treat the melting and re-freezing process easily. The same approach was employed by Lynch-Stieglitz (1994) and Tarboton and Luce (1996).

1.4 Problem statement and objectives

Research shows that vegetation strongly affects snowpack. Bonan (1996) found the destruction of vegetation in the boreal region will expose more snow surface exposing to the atmosphere, increasing surface albedo and lowering surface temperature during the snow seasons. The colder climate will enlarge sea ice extent in the high latitudes and

result in much a lower surface temperature. The colder climate also increases the ratio of snowfall to rainfall and strengthens snow accumulation. However, the vegetation mode is neglected in some complicated snow models (Jordan 1991; Anderson 1976; Loth 1993) and the snow scheme is over-simplified in other models that include vegetation dynamics (Dickinson 1993; Bonan 1996). Thus, the vegetation mode taken from BATS is incorporated in SAST to study the snow and vegetation dynamics.

Model parameters are as important as model structures. In order to search for optimized parameters, the Shuffled Complex Evolution (SCE) Scheme developed by Sorooshian et al. (1993) is connected with the SAST model. Except for finding the optimized parameters, which is the major focus in previous studies (Duan 1992; Sorooshian et al. 1993), the objective of this study is to investigate how variations of model parameters affect physical processes. In this study, observed runoff is used for model calibration. Because snowpack has a considerable contribution to runoff in our study area, the Torne/Kalix basins in Sweden (Bowling et al. 2002), those parameters affecting snowpack simulations are mainly discussed. In addition, the original runoff algorithm designed for GCMs (Dickinson et al. 1993) is re-formulated for watershed applications.

The above two studies are off-line applications of the SAST model and do not include climate feedback. To investigate interactions between snowpack and climate, the SAST model is incorporated into the Community Climate version 3 (CCM3) developed by the National Center for Atmospheric Research (NCAR). Based on model output, we found that snowpack over the Rocky Mountains is greatly overestimated. Stronger

precipitation and colder surface air temperature are also found in model output when compared to observations. To isolate the role of snowpack in these biases, remotely sensed snowpack data are assimilated into the model. In the assimilation process, the energy and mass balances are fully considered.

Although the effects of tropical Pacific SSTs on the snowpack in the western U.S. have been investigated by many researchers (McCabe and Dettinger 2001; Clark et al. 2001), most work is related to observational studies. Our research examines the relationship between tropical Pacific SSTs and snowpack in the western U.S. by comparing observations and model output and includes research on how the varying amplitude of the ENSO cycle is correlated to the different anomalous snowpack pattern in the western U.S.

This dissertation summarizes five aspects of the hydro-climatological studies relevant to snow-atmosphere interactions: (1) developing the physically-based SAST model for the vegetated land surface, (2) evaluating the SAST model at several snow-measurement field sites and especially, testing the model performance for high-latitude land surface processes for the international Project for Intercomparison of Land Surface Parameterization Scheme Phase 2e (PILPS 2e), (3) coupling the SAST model to the CCM3/NCAR, (4) assimilating the large-scale remote-sensing snow depth over the Rocky Mountains into the SAST land surface scheme of CCM3, and (5) studying the relationship between snowpack in the western U.S. and the tropical Pacific SST.

The SAST model represents more physical processes of snowpack than the early versions of snow models in land surface schemes, which include explicitly describing the

liquid and ice phases of snow, improving parameterization of snow properties, especially snow density variability to compaction mechanisms, and parameterizing heterogeneous land surface of snow, soil, and vegetation patches. The model description and primary evaluation have been published in Jin et al. (1999 a, b), Yang et al. (1999), and Sun et al. (1999) and also is addressed in Chapter 2. During the PILPS 2e, the SAST model was further improved with more realistic subsurface runoff processes to better describe runoff generation mechanisms at a river-basin scale. The runoff improvement and SAST performances in the PILPS 2e experiments are discussed in Chapter 3 and in Jin et al. (2002), Bowling et al., (2002), and Nijssen et al. (2002).

CCM3 coupled with the SAST model is used for two studies. First, a reliable remote-sensing snow dataset is assimilated in this coupled model over the Rocky Mountains to study the role of snow in hydrology and climatology. Second, the teleconnection between the variations of the tropical Pacific SST and snow anomalies in the western U.S. are investigated using the coupled model. These two issues are presented in Chapters 4 and 5, respectively, and also in preparation of two manuscripts for peer-reviewed journals. Conclusions are given in Chapter 6.

2. SNOW-ATMOSPHERE-SOIL TRANSFER MODEL FOR VEGETATED SURFACES

2.1 Introduction

Snow cover on land alters the energy and water interactions among the atmosphere, vegetation, and land, and provides significant water resources for many large-scale regions. Because of the importance of snow in global and regional climate and hydrology, a snow model is an essential component in coupled atmosphere and land-surface models. In the early versions of GCM snow models (Dickinson et al. 1993; Bonan 1996), snow temperatures were calculated using the modified force-restore method for a composite with a snow layer overlying soil (Dickinson 1988). Diurnal variations were treated by including a layer of approximately the diurnal penetration depth (about 0.1 m) in the snow-soil composite; over a season, penetration depth is on the order of a few meters. The corresponding heat flux to the bottom of the snow is neglected. Snowmelt is calculated through the surface energy balance. In addition, because heterogeneity across the landscape is important for both albedo and conductive and atmospheric flux transfers, the functions of soil, vegetation, and snow in a GCM grid square are parameterized.

Because the diurnal and seasonal time scales are important for climate modeling, and from the climate and hydrological viewpoint, the most crucial time for snow modeling is during the spring snowmelt period, many studies for improvements have been done recently to involve a more detailed physical description of snow processes in GCMs (Verseghy 1991; Loth et al. 1993; Marshall et al. 1994; Lynch-Stieglitz 1994;

Douville et al. 1995; Pollard and Thompson 1995; Bonan 1996; Walland and Simmonds 1996). These developments show many incorporated factors which can be found in the “point” snow property and process models (e.g., Anderson 1976; Jordan 1991). They are: (1) using coupled snow and soil heat transfer models instead of the force-restore approach for the snow-soil composite, (2) improving parameterization of snow properties, especially relating snow density to various compaction mechanisms, (3) describing the influences of the liquid phase on snow properties and processes, while using the concept of liquid water-holding capacity to simplify the simulation of water flow, and (4) using limited snow layers to reduce the model bias caused by the great variation in temperature and density along the snow depth.

A three-layer SAST model which is a simplification of the complex one-dimensional snow property and process model (SN THERM) of Jordan (1991) and is developed for use in GCMs. The original “point” model of SN THERM assumes that the snow cover overlies a homogeneous surface, say, over a bare flat soil, and requires a large number of computations to describe the multi-phase physical details in the snowpack. To represent snow cover over more realistic areas with a heterogeneous surface and to make the snow computation compatible to a large-scale coupled atmosphere and land-surface model, work is needed to extend and modify the SN THERM model. First, three major simplifications were made in the structure of SN THERM to reduce computations. The SAST model has been tested in a bare soil case against field data. The results are in good agreement with observations and with Jordan’s model (Jin et al. 1999b). Second, the SAST model coupled with a soil model (Dickinson, personal communication 1999)

substitutes for the force-restore calculation in BATS (the vegetation model is the same). Finally, in SAST, we treat the heterogeneous surface by parameterizing snow, soil, and vegetation patches into an areal mixture with fractional coverage for each surface type, which is taken from the concept of BATS (Dickinson et al. 1993; Yang et al. 1997). However in BATS, separate vegetation and soil models are coupled, but as described above, snow and soil are treated as a composite, except in the calculations of grid albedo and drag coefficient. We test the SAST model using field data from France (grass) and BOREAS (forest) to see the performance of this model in these two different land covers.

2.2 Development of SAST model

In order to extend the point SAST model to one representing a grid square, the landscape heterogeneity of soil, vegetation, and snow cover must be represented. Here, we adopted the parameterization approach of BATS. Without snow, the soil surface of a grid square is partially covered with vegetation, which is described by the fractional foliage coverage (f_{veg}). As f_{veg} varies with the vegetation type and seasons, the same percentage of soil surface is treated as soil “under the canopy”, and the remaining portion of soil surface ($1 - f_{veg}$) is “open to the atmosphere”, called “bare soil” (Figure 2.1). During a snow season, snow covers both the vegetation and bare soil, but the fractions of snow cover for these two grid portions need to be estimated separately and then combined together. For the bare soil portion, the fraction of snow cover (f_{snow}^{soil}) is estimated by a

ratio between the averaged snow depth (d_s) and the surface roughness height (R_{ough}) (Dickinson et al. 1993):

$$f_{snow} = \frac{d_s}{d_s + 10 \cdot R_{ough}} \quad (1)$$

where f_{snow} is snow fraction, and $R_{ough} = 0.01$ m for bare soil. The calculated (f_{snow}^{soil}) is the fraction of snow cover within the bare soil portion which is $(1 - f_{veg})$ of the grid square; and, this part of the snow cover is open to the atmosphere. For the vegetation portion of the grid square, two kinds of snow cover are described. The first one occupies a fraction of the original vegetation portion and becomes open to the atmosphere (instead of “under the canopy”). This fraction of open-area snow cover in the vegetation portion (f_{snow}^{veg}) is also estimated by Equation (1) with R_{ough} equal to the roughness height of the grid vegetation. Then, the total fraction of open-area snow cover in the grid square is the summation: $f_{snow}^{soil} \cdot (1 - f_{veg}) + f_{snow}^{veg} \cdot f_{veg}$. As shown in Figure 2.1, with snow cover added into a grid square, the fractional foliage coverage and bare soil coverage for the grid square will vary correspondingly. The fractions of bare soil, vegetation, and open-area snow cover are used as areal weight to calculate skin (grid-averaged surface) properties for the atmospheric model, such as albedo, drag coefficient, but the open-area snow cover is not the entire snow cover in the grid square. In the vegetation portion, there is a second fraction of “under the canopy” snow cover which is also estimated using Equation (1) with $R_{ough} = 0.01$ m. A combination of these three snow covers, two open-areas and one under the canopy, constitutes the single snow cover of the grid square and

will be described by the SAST model. In SAST, the snow cover is divided vertically into layers, but the snow state variables are assumed to be homogeneous horizontally, and then water and energy balance equations are used to solve the state variables for all snow layers. It is crucial to identify the fractions of snow surface in the open area and under the canopy because, when calculating the energy and water fluxes, these fractions of snow surface will deal with different environmental conditions (Figure 2.1): surface fluxes from snow surface in the open area are calculated through temperature (T_a), humidity (q_a), wind speed (V_a), and radiation of the low-level atmosphere, while surface fluxes from under the canopy snow cover are calculated through the corresponding canopy-air variables (with subscript of “ a' ”) calculated by the vegetation models of the land-surface schemes.

A conceptual illustration of the three land-surface components--snow cover, vegetation, and soil-- and their fractional coverage in the modified SAST are shown in Figure 2.1. The visible location separations of surface types in Figure 2.1 is not the real picture of modeling; in modeling, the snow, soil, and vegetation are uniformly blended according to their fractional coverage.

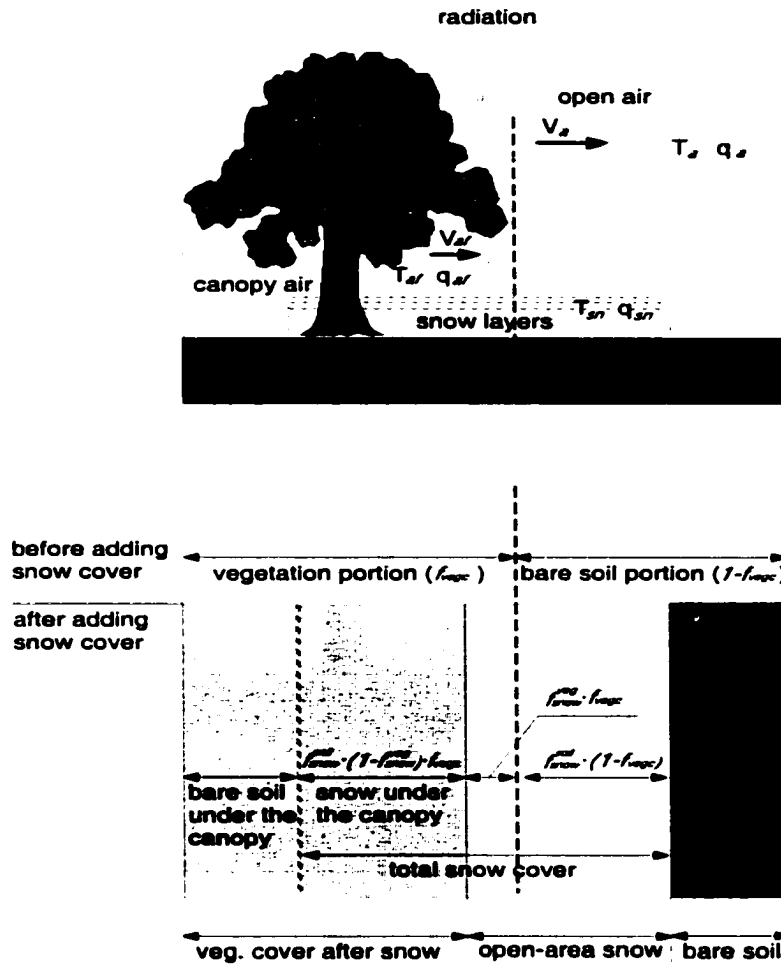


Figure 2.1 Concept illustration of snow, vegetation, and soil and their fractional coverage in a grid square in the SAST model .

Three prognostic variables of snow density (ρ_s), heat content (H), and snow layer thickness (Δz) are solved through the mass and energy equation and the snow compaction model (adopted from the revised SNTHERM codes) (Table 2.1).

Table 2.1 Three snow compaction processes in SAST.

	Metamorphism	Overburden	Melt
Snow compaction (Jordan, 1991) ($\frac{1}{\Delta z} \frac{\partial \Delta z}{\partial t}$)	$-2.8 \times 10^{-6} c_3 c_4 e^{-(273.15-T)/25}$	$-\frac{P_s}{\eta_0} e^{-c_5(273.15-T)} e^{-c_6 \rho_s}$	$-\frac{\text{melt-rate}}{\gamma_s \Delta z} \quad \gamma_s < 250 \text{kgm}^{-3}$
	$c_3 = c_4 = 1 \quad (\gamma_i = 0, \gamma_i \leq 150)$	$c_5 = 0.08 \quad K^{-1}$	$0 \quad \gamma_s \geq 250 \text{kgm}^{-3}$
	$c_3 = e^{-0.046(\gamma_i - 150)} \quad (\gamma_i > 150)$ $c_4 = 2 \quad (\gamma_i > 0)$	$c_6 = 0.023 \quad m^3 / kg$	

2.2.1 Mass Conservation (Continuity) Equation in SAST

The snow density (ρ_s , including both liquid and ice phases described by the mass ice fraction of snow f_{ice}) changes because of snow compaction and flow of liquid water, R_f :

$$\frac{\partial \rho_s}{\partial t} + \frac{\rho_s}{\Delta z} \frac{\partial \Delta z}{\partial t} = \frac{\partial R_f}{\partial z} \quad (2a)$$

where z is the vertical coordinate, t is time, and Δz is snow node thickness (m). $z = 0$ at the snow-soil interface (couple with the soil model) and $z = d_s$ at the snow surface (couple with the atmospheric model). The boundary condition is:

$$R_f \Big|_{z=d_s} = P_o - E \quad (2b)$$

where P_o is the rate of precipitation (downward) ($\text{kg m}^{-2}\text{s}^{-1}$), and E denotes the rate of evaporation (upward) ($\text{kg m}^{-2}\text{s}^{-1}$). Note: because of using the concept of “liquid water-holding capacity”, R_f needs no boundary condition at $z = 0$ (see below).

2.2.2 Energy Conservation Equation in SAST

The heat content (H) for a unit snow volume changes because of ice heat conduction and penetration of net solar radiation, R_s (in W m^{-2}):

$$\frac{\partial H}{\partial t} = \frac{\partial}{\partial z} \left(K \frac{\partial T}{\partial z} + R_s \right) \quad (3a)$$

where T is snow temperature (K), and K is snow thermal conductivity ($\text{Wm}^{-1}\text{K}^{-1}$). The boundary conditions (fluxes) at the surface and bottom of snow cover are expressed as:

$$\left(K \frac{\partial T}{\partial z} + R_s \right) \Big|_{z=d_s} = R_s^n + L_{net} - I_{sen} - L_{lv} \cdot E + I_{prec}, \quad (3b)$$

$$K \frac{\partial T}{\partial z} \Big|_{z=0} = - \frac{2 \cdot K^l \cdot K_{soil} \cdot (T^l - T_{soil})}{K_{soil} \cdot \Delta z^l + K^l \Delta z_{soil}}$$

where R_s^n and L_{net} are net solar and long-wave radiation at snow surface (Wm^{-2}); I_{sen} is sensible heat flux (Wm^{-2}); L_{lv} denotes latent heat of evaporation (Jkg^{-2}); I_{prec} is the heat flux of precipitation (Wm^{-2}); K_{soil} is soil thermal conductivity ($\text{Wm}^{-1}\text{K}^{-1}$); K^l is the thermal conductivity of bottom snow layer ($\text{Wm}^{-1}\text{K}^{-1}$); and T^l and T_{soil} are temperatures from the bottom snow layer Δz^l and the top soil layer Δz_{soil} , respectively.

In Equation (3a), the heat content (H in $\text{J m}^{-3}\text{K}$) is expressed as:

$$H = C_v \cdot (T - 273.15) - f_{ice} \rho_s L_{li} \quad (4)$$

where C_v is the volumetric specific heat of snow ($\text{J m}^{-3}\text{K}^{-1}$), and L_{li} is the heat of fusion (J kg^{-1}).

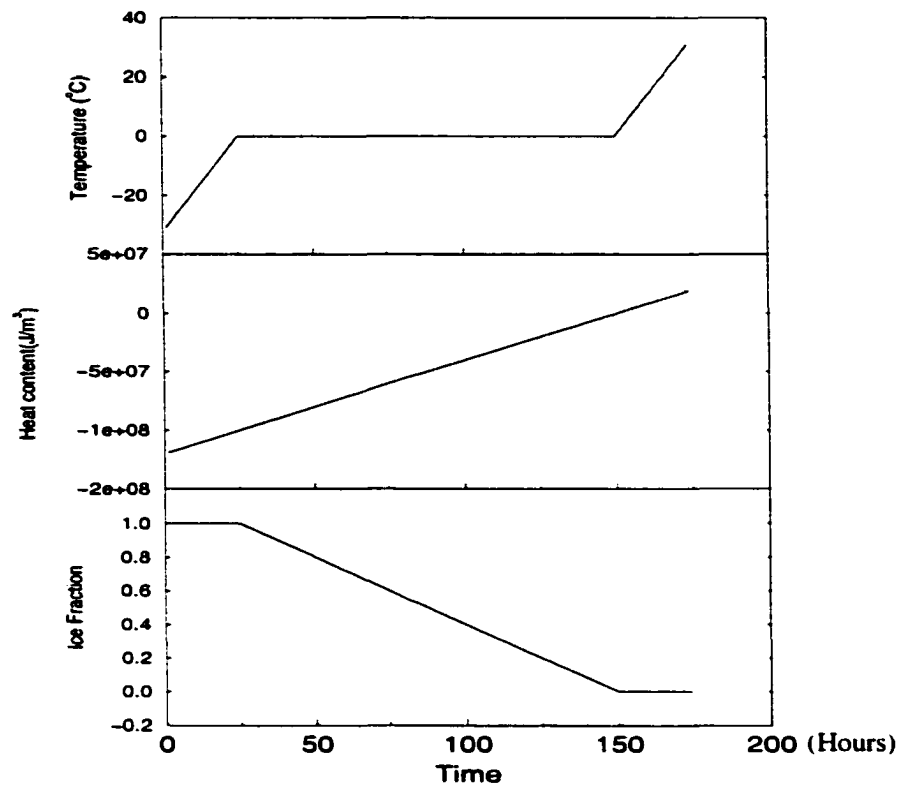


Figure 2.2 Determination among H , f_{ice} , and T in an ice-liquid water system in the SAST model.

Note that (a) H includes the internal energy of liquid water or ice as well as the energy of the phase change between liquid water and ice, and (b) the internal energy of liquid water at the melting point (273.15 K) is set at zero (a relative value). Figure 2.2 illustrates how the variables H , T , and f_{ice} of Equation (4) change when a unit volume of pure ice is uniformly heated to pure liquid water. When H has a zero or positive value, the system is in the pure liquid phase ($f_{ice} = 0$), with temperature at or above the melting point; if H has a negative value equal to or less than $-\rho_s L_{li}$, the system is in the pure ice phase ($f_{ice} = 1$) with the temperature at or below the melting point, otherwise, the system

is a mixture of liquid water and ice at the melting temperature, and the fractional variable (f_{ice}) is determined by the value of H . The continuous feature of H during phase change simplifies computation. In addition, by assuming liquid water energy equal to zero at the melting point, the energy of the melt water flow becomes constant at zero and does not show in the energy equation (Equation 3a); it only remains in the mass equation (Equation 2a). The method was also used by Lynch-Stieglitz (1994) and Tarboton and Luce (1996).

In order to solve variables ρ_s , H , and Δz , we need to define the right-hand terms in the governing equations, i.e., liquid flow, ice heat conduction, and radiation penetration, as well as those in the boundary condition equations, i.e., the surface fluxes.

Anderson's (1976) formula for computing liquid water-holding capacity (C^R) from snow density is adopted in the SAST model:

$$C^R = \begin{cases} C_{\min}^R & \gamma_i \geq \gamma_e \\ C_{\min}^R + (C_{\max}^R - C_{\min}^R) \frac{\gamma_e - \gamma_i}{\gamma_e} & \gamma_i < \gamma_e \end{cases} \quad (5)$$

where $C_{\min}^R = 0.03$, $C_{\max}^R = 0.1$, $\gamma_e = 200$ (kgm^{-3}), and $\gamma_i = \rho_s f_{ice}$ is partial density of ice (kgm^{-3}). The liquid water transport in the snowpack is not dynamically described. If the liquid water content in a snow layer exceeds the water-holding capacity, the excess amount drains to the underlying layer. Hence, flow of liquid water (R_f) is:

$$R_f = \begin{cases} 0 & f_{ice} \geq \frac{1}{1+C^R} \\ [1 - f_{ice}(1+C^R)] \frac{\rho_s \cdot \Delta z}{\Delta t} & f_{ice} < \frac{1}{1+C^R} \end{cases} \quad (6)$$

There is no constraint applied at the bottom of snowpack ($z = 0$). Infiltration of snowmelt water into frozen and unfrozen soils might be quite different, which needs to be further explored.

The calculations relevant to the right-hand terms in the governing equations (i.e., thermal conductivity, solar radiation entering a snowpack) and those in the boundary equations (i.e., mass ice fraction of precipitation, partial density of ice in snowfall) are given in Table 2.2. Table 2.3 shows the differences in calculating fluxes on snow surfaces under the canopy and in the open area. The total flux is the area-weighted summation of fluxes from both portions. The calculations for snow albedo (Dickinson et al. 1993) in SAST are given in the Appendix A.

Table 2.2 Calculations for the right-hand terms in the governing equations and boundary equations in SAST.

Thermal conductivity of snow (K) (Yen, 1965)	$K = 3.2217 \times 10^{-6} \cdot (\rho_s)^2 \quad (w m^{-1} K^{-1})$
Volumetric specific heat capacity of snow (C_v) (Verseghy, 1991)	$C_v = 1.9 \times 10^6 \frac{\rho_s}{\rho_i} \quad (JK^{-1}m^{-3})$
Solar radiation in a snowpack (R_s) (Jordan, 1991)	$R_s(z) = \begin{cases} R_s^n \cdot [e^{-0.002\beta_{nr}} (e^{-\beta_{vis}(d,-z)} - 1) + 1] & \text{Top node} \\ R_s^n \cdot e^{-\beta_{nr}(d,-z) - 0.002\beta_{nr}} & \text{Interior nodes} \end{cases}$ <p>Extinction coefficients: $\beta_{nr} = 400.0$ $\beta_{vis} = \frac{0.003795 \cdot \rho_s}{\sqrt{d}}$</p>
Ice mass fraction of precipitation (f_{ice}) (Referenced in code)	$f_{ice} = \begin{cases} 0.0 & T_{air} > 2.5^\circ C \\ 0.6 & 2.0^\circ C < T_{air} \leq 2.5^\circ C \\ 1 - [54.62 - 0.2(T_{air} + 273.15)] & 0.0^\circ C < T_{air} \leq 2.0^\circ C \\ 1.0 & T_{air} \leq 0.0^\circ C \end{cases}$
Partial density of ice in snowfall (γ_i) (LaChapelle, 1961)	$\gamma_i = \begin{cases} 0.0 & T_{air} > 2.5^\circ C \\ 189.0 & 2.0^\circ C < T_{air} \leq 2.5^\circ C \\ 50.0 + 1.7(T_{air} + 14.99)^{1.5} & -15^\circ C < T_{air} \leq 2.0^\circ C \\ 50.0 & T_{air} \leq -15^\circ C \end{cases}$
Heat flux of precipitation (I_{prec})	$I_{prec} = \begin{cases} C_i P_0 (T_p - 273.15) & \text{for rainfall} \\ C_v \frac{\Delta z_p}{\Delta t} (T_p - 273.15) - P_0 L_{fi} & \text{for snowfall} \end{cases}$ <p>where new snow thickness $\Delta z_p = \frac{P_0 \Delta t f_{ice}}{\gamma_i}$</p>

Table 2.3 Snow surface fluxes in SAST.

(W/m ²)	Snow under the canopy	Snow on bare soil
Net surface solar radiation (R_s^n)		$I_s^\downarrow \cdot (1 - \alpha)$
Net long-wave radiation (L_{net})	$\epsilon_f \sigma T_f^4 - \sigma T_{sn}^4$	$\epsilon_{air} \sigma T_{air}^4 - \sigma T_{sn}^4$
Latent heat flux ($L_{iv}E$)	$\rho_a W_C f_g (q_{sn} - q_{af})$	$\rho_a W_G (q_{sn} - q_{air})$
Sensible heat flux (H_s)	$\rho_a c_p W_C (T_{sn} - T_{af})$	$\rho_a c_p W_G (T_{sn} - T_{air})$

2.3 SAST Model Evaluation

2.3.1 French Data Set

The Centre d'Etude de la Neige in Grenoble, France measures both atmospheric forcing and snow properties at hourly intervals at the Col de Porte (45°N, 6°E, 1320 m asl) in the French Alps (Brun et al. 1992). This site is characterized by a continuous snow cover in winter, usually lasting from late autumn to late spring, with loamy soil and short-grass vegetation. Meteorological forcing data include air temperature, specific humidity, wind speed, precipitation amount, snow/rain index, downwelling solar, and long-wave radiation. Measured snow properties are snow depth, surface temperature, and daily albedo. The parameters for vegetation and soil types were selected from the BATS global soil/vegetation data base (Table 2.4). The simulation period was from December 17, 1988 to May 7, 1989.

Table 2.4 Parameters of soil and vegetation in SAST (Dickinson et al. 1993).

	Col de Porte	BOREAS Southern Study Area
Vegetation type	Short grass (type 2)	Deciduous broadleaf tree (type 5)
Soil texture class	Type 4 (loam)	Type 6
Soil color	Type 1	Type 3

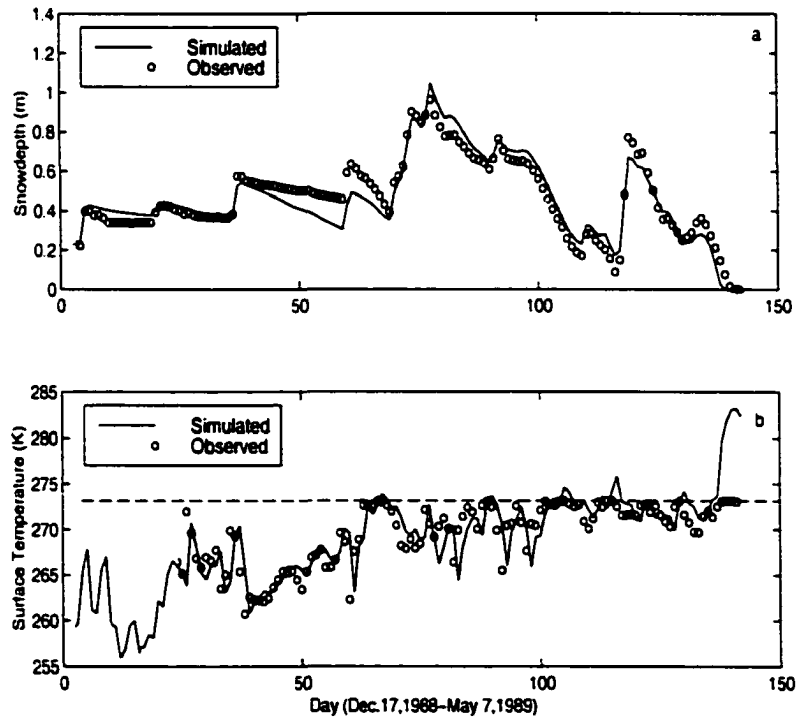


Figure 2.3 Comparison of snow depth and skin temperature from the SAST model output with observations in the grassland at Col de Porte, France.

Simulated snow depths agree well with observations (Figure 2.3a); however, simulated daily skin temperatures were slightly different from observed surface temperature (Figure 2.3b). On some days, simulated skin temperatures were above the melting point, while the observed temperatures remained at or below the melting point.

This suggests that observed temperature was measured in a small snow-covered area, while the modeled skin temperature is the area-weighted mean of three different surface composites, i.e., snow, vegetation, and bare soil. Figure 2.4 shows that the diurnal skin temperature differed from the snow surface temperature, and the latter closely matched with the observations, especially during the day. In Figure 2.5, because of the low values of vegetation and bare soil albedo, the grid surface albedo was consistently lower than the observations while the modeled snow surface albedo varied around the mean of the observed (Figure 2.5). Except for high-frequency variations in observed albedo, the simulation albedo as a function of surface snow age (Dickinson et al. 1993) was quite satisfactory. Because observed albedo was not very reliable (Eric, personal communication 1998), further adjusting the model to match observed albedo was not performed.

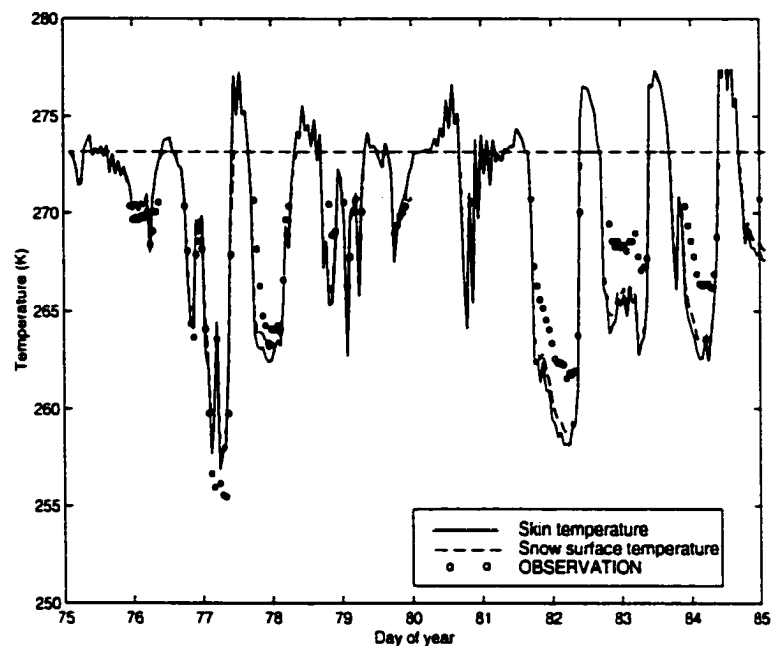


Figure 2.4 Comparison of snow surface temperature and skin temperature from the SAST model with observations at Cold de Porte, France.

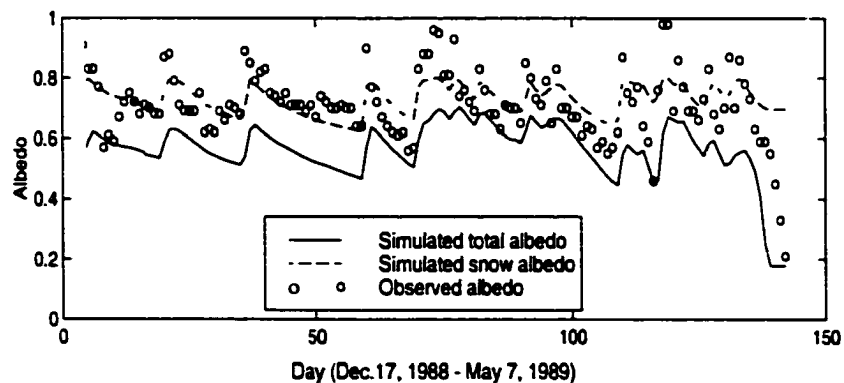


Figure 2.5 Comparison of snow surface albedo and surface albedo from the SAST model with observations at Col de Porte, France.

2.3.2 BOREAS Data Set

The second set of observations were collected at the southern intensive study area of the Boreal Ecosystem Atmosphere Study (BOREAS) (<http://boreas.gsfc.nasa.gov>), located on the southern edges of the Canadian boreal forest, 600 km from Prince Albert, Saskatchewan. BOREAS is a large-scale field investigation to study interactions between the boreal forest biome and the atmosphere, clarifying their roles in global change. The Southern Study Area (SSA) covers a domain large enough to allow the acquisition of useful airborne flux measurements and satellite observations, but small enough to conserve a reasonable density of surface instrumentation, including six towers of 20 m height for flux and meteorological measurements. In the BOREAS study area, snow cover exists more than 100 days a year, and the forests of aspen and pines provide strong interaction among the atmosphere, land surface, and snow cover. Because the BOREAS data are still under processing and only open to the project investigators, we were only able to use limited data in this very primary study. The 15-minute interval meteorological forcing and snow data at the old aspen site (53.628° N and 106.196° W) of the SSA were used in this study. The simulation period was January 1 (DOY 1) to April 20 (DOY 111), 1994. Model parameter values were taken from the BATS database.

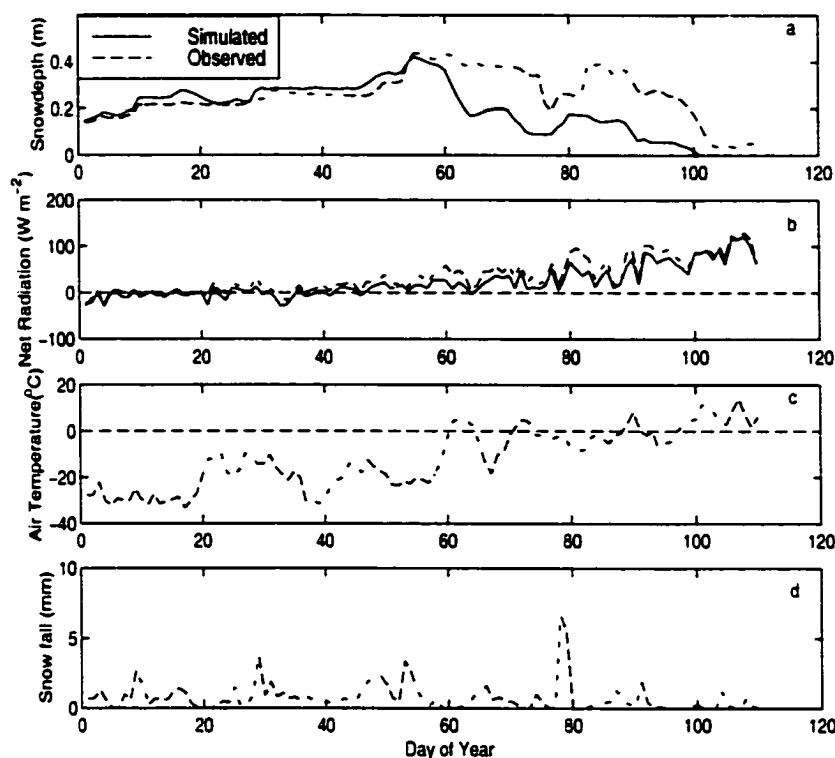


Figure 2.6 Comparison of (a) snow depth and (b) surface net radiation with observations, (c) observed air temperature, and (d) observed snowfall snow in old aspen region of SSA at Boreal, Canada.

In Figure 2.6a, before DOY 60, i.e., March 2 (the winter period), modeled and observed snow depth matched well while, after March 2 (the spring period), the model severely underestimated snow depth, even though the modeled net radiation (a main energy source for snowmelt) in the spring period was still lower than the observed radiation (Figure 2.6b). In the spring season, net solar radiation was increased gradually, while the increase of air temperature involved four warm waves in which temperatures were above 0°C for a few days (Figure 2.6c). Each of these warm waves corresponded to a marked reduction in modeled snow depth (Figure 2.6a), but not as severe as in the

observed snow depth. Snow protected by the canopy does not melt as quickly as in the open area and might still keep a thick snow depth, which could possibly be what was observed. Figure 2.7a indicates that during the spring, the modeled net surface energy for the open-area snow was several times stronger than that for the under-canopy snow. Within the model, the sensible heat during these warm waves produced significant snowmelt in the open area, which consequently reduced the modeled (average) snow depth. In Figure 2.7b, the fraction of snow under the canopy varied following that of the open-area snow, which indicates that the canopy snow could unrealistically “smear” to the open area, because the model was designed for simulating the averaged snow depth. Differences between the observed and modeled snow depth in the spring period may be due in part to the area observed being only a subset of that modeled. First, the snow depth data at the Prince Albert old jack pine site in the same SSA (Way et al. 1997) showed a rapid decline in snow depth in the first warm period (DOY 60-63), which did not show in Figure 2.6a. Second, from Figure 2.6d, there seemed to be an insufficient amount of snowfall during DOY 81-83 to create an increase in snow depth shown in Figure 2.6a. Third, the snowfall and snow depth were measured at different places (Berry, personal communication 1998).

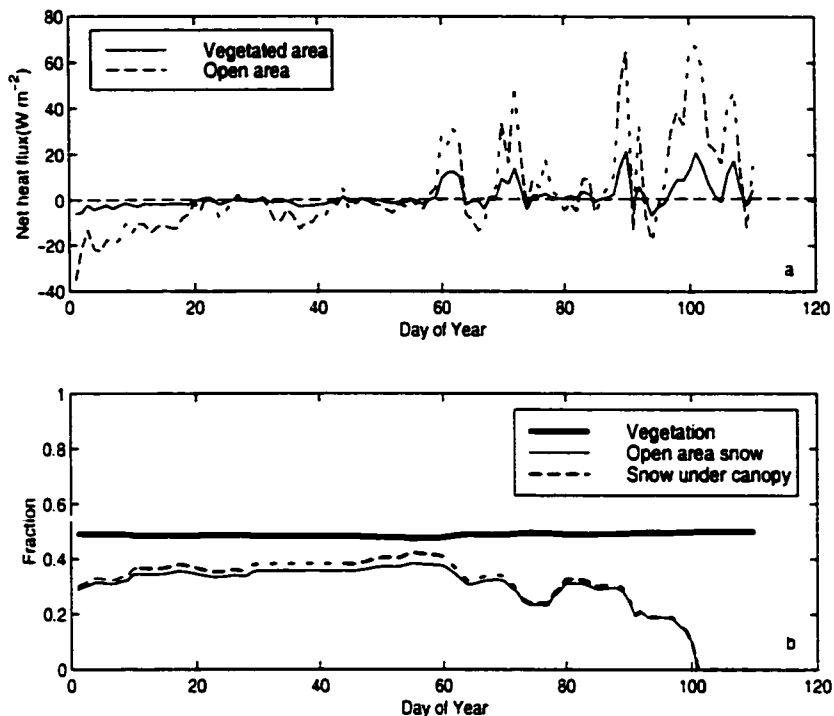


Figure 2.7 SAST model output: (a) Net heat flux for open area snow and under canopy snow, and (b) fraction of vegetation under canopy snow and open area snow in old aspen region of SSA at Boreal, Canada.

The simulated skin temperature matched with the observed surface temperature measured from the tower (Figure 2.8a). Figure 2.9 shows that the model simulated surface fluxes over vegetation, bare soil, and snow surface, separately, and also simulated a fraction of each. In the winter period, snow cover increased and the surface exchanges were depressed, while in the spring period, exchanges at the surface became important. Vegetation warmed and started to have upward sensible and latent heat fluxes. In contrast, the snow surface and bare soil became wetter than before but still colder than the air temperature; therefore, they had upward latent heat fluxes and downward sensible heat

fluxes. The net result was a positive latent heat flux in spring and a highly variable sensible heat flux (Figure 2.8b). Unfortunately, because of equipment problems during cold weather, observations were not available (Berry, personal communication 1998). It is clear that, with such complex temporal variability and spatial heterogeneity over the forest landscape, a model with a separate simulation of different components is both necessary and useful.

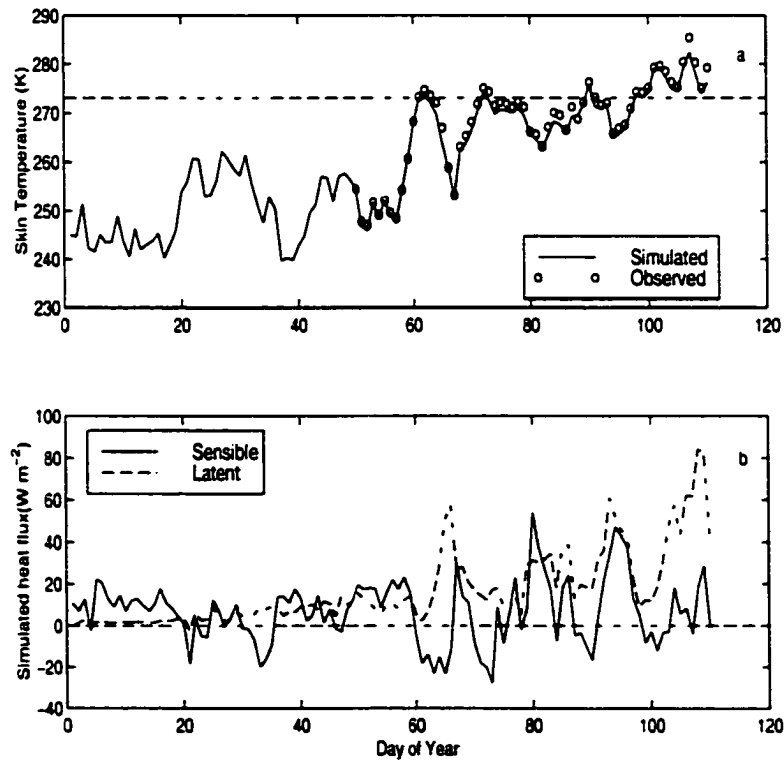


Figure 2.8 SAST model output: (a) Skin temperature and observations and (b) surface turbulent fluxes in old aspen region of SSA at Boreal, Canada.

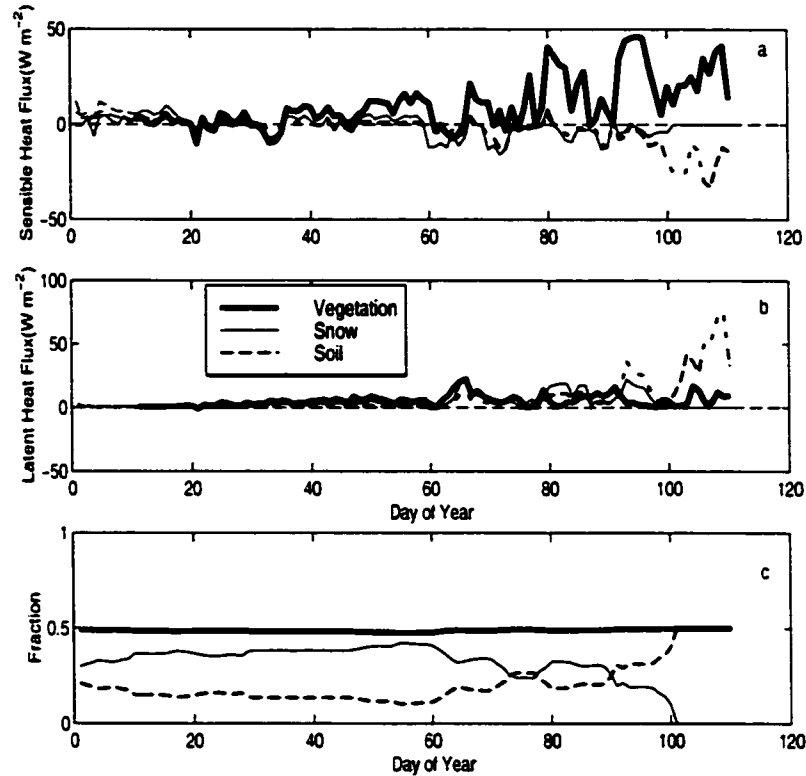


Figure 2.9 Deposition of surface energy fluxes into vegetation, snow, and bare soil contributions. SAST model output: (a) sensible heat flux, (b) latent heat flux, and (c) fractional coverage of vegetation, snow, and bare soil.

2.4 Discussions

We realized that the setting of parameter values could substantially affect the simulation results. After comparing the soil and vegetation parameter values provided by the BOREAS documents (Coughlan and Running 1994) with those used from the BATS data base, we found that they were close. Because most of the BOREAS document values were not measured in the field, we decided to use only the BATS parameter values.

The SAST model presented here is not a point model, but represents the average features of an area characterized by the BATS database. Because field observations are

usually conducted at sites much smaller than the modeled area, they are expected to be different from the area means. Therefore, the comparison between the modeled results and field observations must be analyzed carefully to explore the suitability of the model, and the model should not be judged simply by agreement or disagreement. In this study, the model was driven by the observed meteorological forcing, and the model parameters were fixed without “tuning”. We found that the simulations matched observations under two conditions: (a) when the study area was relatively uniform, such as in the short grass land in France, and (b) when the observations contained some kind of area-average features, such as the surface temperature and net radiation measured from a high tower. These provide the evidence that the model and its parameters are generally suitable for these study sites. The disagreements (besides caused by various errors) essentially resulted from the different scales between modeling and observation. Recently, in a BOREAS study, Hardy et al. (1997) showed that snow depth possessed substantial spatial variability, even around a single tree. Therefore, they used SN THERM coupled with a geometric optical-radiative transfer model (Li et al. 1995) to conduct a series of point simulations along the observation locations.

2.5 Conclusions

Introducing parameterization of subgrid heterogeneity into the SAST model is a way of extending the point model to areas. The good agreement between modeled and observed skin temperature and albedo, and the reasonable explanation for the complicated responses of surface fluxes, indicate that this approach captured the essentials of sub-grid

heterogeneity, and its formulations and parameter values are representative. This chapter has been published in *Hydrological Processes* (Jin et al. 1999a).

3. IMPACTS OF MODEL CALIBRATION ON HIGH-LATITUDE LAND-SURFACE PROCESSES

3.1. Introduction

This chapter is one of the studies for the Project for Intercomparison of Land-Surface Parameterization Schemes phase 2e (PILPS 2e). In the first stage of PILPS 2e experiments, participants were instructed to make calibration-validation runs for two representative sub-basins (Ovre Lansjarv and Ovre Abiskojokk) in the study area of the Tome-Kalix River basin using 10-year (1989-1998) streamflow observation data, and then apply the calibrated model to the entire river basin. The objective of the experiments was to evaluate the performance of uncoupled land-surface schemes in high-latitude environments, in a context that allows evaluation of their ability to capture key physical processes spatially (Bowling et al. 2002). In the GEWEX/ACSYS workshop report (WCRP 1999), the goals of these intercomparison experiments are specified as (1) to quantify the accuracy with which current land-surface schemes represent high-latitude land processes, (2) provide information about pathways for model improvements, and (3) provide information about the accuracy with which land-surface schemes can be used to estimate runoff from ungauged areas draining to the Arctic Ocean. Following this guideline, our land-surface model, the Snow Atmosphere Soil Transfer (SAST) scheme, greatly benefited from the calibration-validation experiments. The performance of the snow hydrology scheme in the high-latitude environments was tested, and the runoff generation scheme was improved to better respond to the spring snowmelt events. The

capability of runoff prediction of the calibrated model verified very well in the applications to the two validation sub-basins (Pello and Kaalasjarvi) as well as the entire Torne-Kalix River basin (Bowling et al. 2002).

The SAST land-surface scheme was developed to improve the snowmelt process in GCMs by the inclusion of critical physical properties and snow processes (Chapter 2; Jin et al. 1999a; Sun et al. 1999). From the climate viewpoint, the most crucial time for snow modeling is during the spring snowmelt period. This same period is also critical for hydrologic predictions. Over this period, solar fluxes are large, and drastic albedo variations with the removal of the snow have a major effect on land-surface processes. Further, the timing of snowmelt has a major influence on the timing of water removal by runoff. A better description of this spring snowmelt period could contribute substantially to understanding the relationships between snow cover, atmospheric processes, and surface energy and water budgets during normal and anomalous snow cover regimes (Marshall et al. 1994; Cayan 1996; Walland and Simmonds 1996; Leese 1997; WCRP 1999; Kripalani and Kulkarni 1999; Giorgi et al. 2001). The new snow scheme of SAST has simplified the U.S. Army Cold Regions Research and Engineering Laboratory (CRREEL) snow property and process model (Jordan 1991) and also has extended this point model to vegetated areas using the parameterization concepts of BATS (Dickinson et al. 1993). In the current SAST land-surface scheme, the descriptions of other physical processes including biological, radiative and thermal transfers, and soil hydrology are based on BATS with certain modifications (discussed later). The snowmelt processes of SAST have been tested in off-line mode using the observation data from Mammoth

Mountain in the eastern Sierra Nevada, California (Jin et al. 1999b) and two vegetated fields--a short grassland in the French Alps and an old aspen forest in the southern study area of BOREAS (Jin, et al. 1999a). However, until the PILPS 2e experiments, the model had not been tested for runoff generation in cold regimes responding to the heavy spring snowmelt. When SAST was applied to the uncalibrated runs of PILPS 2e, the model was deficient in predicting the pattern and quantity of runoff from the heavy spring snowmelt events. These model deficiencies were resolved by modifying the runoff scheme and parameter calibration which significantly improved the accuracy of runoff prediction and showed high potential to estimate runoff from ungauged areas draining into the Arctic Ocean.

In the current PILPS 2e experiments, the only observation data available for calibration are the long-term streamflow data, which are insufficient to evaluate the accuracy of land-surface schemes in representing many high-latitude land-surface processes. As summarized in Bowling et al. (2002), the participant land-surface schemes, even after calibration with the observational runoff data, still showed very diverse results in many crucial physical variables: runoff, snow cover, soil moisture, and surface water and energy fluxes. Therefore, more aspects of observation data and a more detailed examination of internal physical processes are needed to improve the future PILPS 2e experiments.

In this chapter, the knowledge relevant to these issues learned from our participation in the first-stage of PILPS 2e experiments using the SAST model is addressed. The scope of this chapter is as follows. In Section 3.2, the SAST land-surface

scheme is concisely described. In Section 3.3, uncalibrated results are analyzed, which leads to the necessary modification and calibration of the model. Validation results of the revised model are presented in Section 3.4, Section 3.5 includes the overall evaluation of the SAST model in the PILPS 2e study, and Section 3.6 contains discussions and conclusions.

3.2. Model Description

The SAST model has been described in detail in Chapter 2. Here, a simple summary for this model is given as follows. The snow sub-model in the SAST land-surface scheme is one of multiple efforts to use physically-based snow properties and processes models to describe the variation of snow cover for a wide region, especially for both long-term and short-term atmosphere modeling (Verseghy 1991; Loth et al. 1993; Lynch-Stieglitz 1994; Douville et al. 1995; Bonan 1996; Hardy et al. 1997; Sun et al. 1999). The developments of the SAST snow scheme include: (1) using coupled snow and soil heat transfer models, (2) improving parameterization of snow properties, especially relating snow density to three compaction mechanisms (metamorphism, overburden, and melt), (3) explicitly describing influences of the liquid phase on snow properties and processes, (4) using three snow layers to reduce the model bias caused by the great variation in temperature and density along the snow depth, and (5) parameterizing heterogeneous land surface of snow, soil, and vegetation patches into an areal mixture with fractional coverage for each surface type, which is taken from the concepts of BATS

(Dickinson et al. 1993). More detailed descriptions of the snow scheme can be found in Jin et al. (1999a) and Sun et al. (1999).

In the BATS version on which the SAST scheme is based (Dickinson, personal communication), only one major change has been made from version 1e (Dickinson et al. 1993): the original force-restore method for soil-temperature calculation has been modified to solve heat-transfer equations in soil layers. The soil moisture calculated from the Richards equation is for three nested layers from surface to different depths: the top layer from surface to 0.1 m; the root zone layer from surface to 1 m, and the total (deep) layer from surface to 5 m. In BATS, the freezing process of soil is not explicitly simulated; it only sets the saturated soil hydraulic conductivity to zero (cease the water flow in soil) when the soil temperature reaches the freezing point. Obviously, this could be a shortcoming of the model when applied to the high-latitude region. Another possible shortcoming is that the runoff generation mechanisms consist of only two components: the surface (overland) runoff and deep drainage as shown in the following equations:

$$R_1 = G(\rho_w)^a \quad a = 4 \quad (T_g \geq 273.15); \quad a = 1 \quad (T_g < 273.15) \quad (1)$$

$$R_2 = K_s \rho_{tw}^{2b+3} \quad (2)$$

where R_1 and R_2 represent the surface runoff and deep drainage, respectively; G is the net surface water; K_s is the saturated soil hydraulic conductivity; b is the exponent for different soil type; ρ_w is the mean soil water saturation in the top and root zone layers; and ρ_{tw} is the soil water saturation in the total layer.

In the SAST scheme, except the snow part, all of the equations and parameters are adopted from BATS without changes because our intension has been to focused on the impact of snow process on coupled GCM results.

The PILPS 2e document (Bowling et al. 2002) provided the 1979-1998 daily meteorological data at $\frac{1}{4}^{\circ}$ (latitude-longitude) grid resolution for off-line forcing of the model runs and the parameter values of soil and vegetation properties for reference (Bowling et al. 2002). The Ovre Lansjarv (forest) sub-basin includes ten $\frac{1}{4}^{\circ}$ -grids, the Ovre Abiskojokk (mountain) sub-basins includes seven $\frac{1}{4}^{\circ}$ -grids and the whole Torne-Kalix River basin includes 218 $\frac{1}{4}^{\circ}$ -grids. For simplicity, in the uncalibrated and calibrated runs, the $\frac{1}{4}^{\circ}$ -grids in each sub-basin were lumped together as a single basin using the average forcing and uniform parameters. Then, the calibrated model was applied to each of the 218 grids for validation of the whole Torne-Kalix River basin. Because the PILPS 2e document only provided 10-year (1989-1998) streamflow data to the participants, the 1989-1990 streamflow data were used for calibration and the remaining 8-year data were saved for validation. The initial conditions were determined after a long-term run when the deep soil moisture reached quasi-equilibrium.

3.3 Uncalibrated Results

When applying the model with the parameters used in BATS to the Ovre Lansjarv (forest) and the Ovre Abiskojokk (mountain) sub-basins for 1989-1990, serious discrepancies appear between the simulated and observed runoff, as shown in Figure 3.1. The observed streamflow (solid line) in both the forest and mountain sub-basins started in

the mid-spring season, but the simulated runoff (dashed line) occurred much earlier than the observations. In the daily results (Figures 3.1b and e), the model generated many intense and short “spike-like” streamflows as responses to the strong rainfall and snowmelt events, which were not consistent with the observations. In monthly averaged data (Figures 3.1c and f), although these “spikes” were smoothed, the phases of peak flow in the simulations occurred about a month earlier than the observations, and the average annual runoff was about 20-50% less than the observations. The statistics, (Root Mean Square Error, RMSE and Correlation) calculated from the time series show poor matching between the simulation and observation data.

The results expose model deficiencies in simulating the runoff and hydrological processes for the cases provided by the PILPS 2e experiments. Figure 3.1 shows that, after almost ceasing streamflow and accumulating snowfall in the cold winter, starting from mid-spring, large amounts of runoff were generated by high-frequency intense snowmelt events (Figures 3.1a-b and d-e). The daily streamflow observations indicate that both sub-basins were capable of delaying the runoff release for almost ten days to respond to the strong snowmelt events. Snowmelt was concentrated in April and May and extended to June. The streamflow reached the annual peaks in May and, afterwards, rapidly reduced and kept low-level recession during the summer and fall. The patterns of streamflows were also complicated due to the temporal freezing of the soil layers and water storage in lakes, which has not been explicitly simulated in the model. Therefore, model modification is needed.

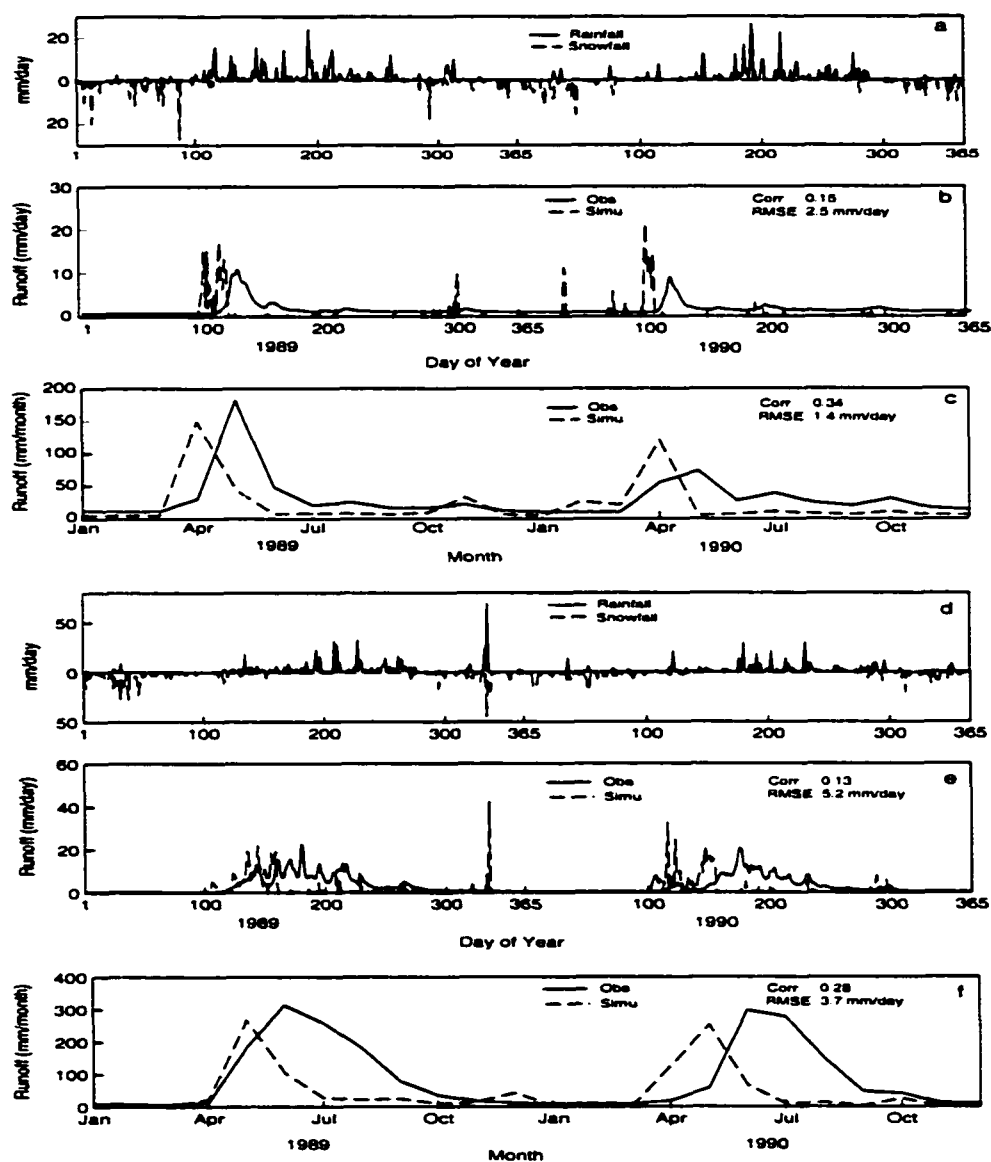


Figure 3.1 Comparison of daily and monthly runoff predicted by the uncalibrated SAST scheme with the observation during 1989-1990, for the forest sub-basin (a, b and c) and mountain sub-basin (d, e, and f).

First, as described above, the runoff formulations of the model only include overland flow (Eq. 1) and the deep drainage (Eq. 2); the subsurface runoff is not presented. Because overland flow produces no-delay runoff from the surface water provided by rainfall and snowmelt (G in Eq. 1), and because deep drainage only affects the baseflow, subsurface runoff with different response times is crucial to the runoff simulations in the PILPS 2e cases. A set of revised equations representing different runoff components with weighting factors (C_1 , C_2 , C_3 , and C_4) are proposed in the calibration runs:

$$R_1 = C_1 G (\rho_w)^a \quad a = 4 \quad (T_g \geq 273.15); \quad a = 1 \quad (T_g < 273.15) \quad (3)$$

$$R_2 = C_2 K_s \rho_{rw}^{2b+3} \quad (4)$$

$$R_3 = C_2 (\rho_{sw} - \rho_0)^3 \quad (\rho_{sw} \geq \rho_0) \quad \text{or} \quad R_3 = 0 \quad (\rho_{sw} < \rho_0 \quad \text{or} \quad T_g < 273.15) \quad (5)$$

$$R_4 = C_2 (\rho_{sw} - \rho_0)^3 \quad (\rho_{sw} \geq \rho_0) \quad \text{or} \quad R_4 = 0 \quad (\rho_{sw} < \rho_0 \quad \text{or} \quad T_g < 273.15) \quad (6)$$

$$R_t = R_1 + R_2 + R_3 + R_4 \quad (7)$$

where, only Eqs. 5 and 6 are new: R_3 and R_4 represent the subsurface runoffs from the soil to the 0.1-m depth and 1-m depth, respectively; ρ_{sw} and ρ_{rw} are the soil water saturation in these layers and ρ_0 is the soil wilting point (saturation). Eqs. 5 and 6 indicate that subsurface runoff is related to the “available” soil moisture, $(\rho_{s,rw} - \rho_0)$, in the soil layers. Through model calibration, it is expected to determine the weighting factors (C_1 , C_2 , C_3 , and C_4) to find the realistic partitions of the runoff in the streamflow.

Second, the model parameters representing the physical properties of soil and vegetation have strong influences on the hydrological processes. In Table 3.1, the values of these parameters recommended by the PILPS 1e document and used by BATS at the

GCM grids are listed. The BATS values seem quite different from the PILPS recommendation, which is considered to be another major reason for the poor uncalibration results. However, direct replacements of BATS parameter values with those recommended by PILPS 2e can also cause inconsistency because, although they possess common physical definitions, the functions and significance of these parameters in models are quite “model-dependent”. It is assumed that proper parameter values are within the physical ranges given by these two data sets and need to be found through calibration.

Table 3.1 List of selected parameters and their ranges for calibration (F = Forest region, M = Mountain region).

No.	Parameter	F/M	F/M	F/M	Explanation of Parameters
		Default	Lower	Upper	
1	Vegc	0.8	0.6	1.0	Max. vegetation fraction [-]
2	Seasf	0.2/0.3	0.0	0.3	Seasonal change of vegetation fraction [-]
3	Rough	0.8/0.1	0.5/0.05	1.5/0.2	Vegetation roughness [m]
4	Dewmx	0.1	0.01	0.5	Max. allowed dew [mm]
5	Cthk	1.0	0.1	10.	Coefficient for thermal conductivity
6	C1	0.5	0.0	1.0	Coefficient for surface runoff
7	C2	0.5	0.0	1.0	Coefficient for top layer runoff
8	C3	0.5	0.0	1.0	Coefficient for root zone runoff
9	C4	0.5	0.0	1.0	Coefficient for bottom drainage
10	Ssw	10	0.01	40	Initial water in upper soil layer [mm]
11	Rsw	100	5	400	Initial water in root zone layer [mm]
12	Tsw	1000	50	2000	Initial water in total soil layer [mm]
13	Xmohyd	3.47e-3	1e-5	1e-1	Max. hydraulic cond. of soil [mms ⁻¹]
14	Xmopor	0.43/0.39	0.33	0.50	Soil porosity [-]

In Table 3.2, 10 parameters representing soil and vegetation properties and runoff partition factors are selected for calibration. Table 3.2 also provides the feasible variation ranges for these parameters. The objective of calibration is to determine a unique set of parameter values by “best” matching the model streamflow (total runoff) to the observation (i.e., to minimize the RMSE between model and observation runoff for the 2-year calibration period). The key process of calibration is to search the “global optima” for these parameters through the high-dimensional domain of parameters. Obviously, this calibration cannot be done with manual “tuning” of model parameters. An automatic calibration technique, the Shuffled Complex Evolution (SCE) scheme (Duan et al. 1992) was used. By linking the model with the SCE scheme, SCE will conduct a large number of test runs with randomly selected parameter values in the search domain and, through several rounds of evolution, the searching will converge to the optimized values of the parameters.

Table 3.2 The optimized parameters obtained through the SCE automatic calibration method.

No.	Parameters	Forest Region	Mountain Region
1	vegc [-]	0.997	0.981
2	seasf [-]	2.9e-3	0.28
3	rough [m]	1.07	0.0834
4	dewmx [mm]	0.235	0.146
5	Cthk [-]	8.7	9.81
6	C1[-]	8.31e-4	1.99e-4
7	C2[-]	1.53e-6	1.44e-5
8	C3[-]	1.49e-3	4.53e-4
9	C4[-]	0.781	1.66e-2
10	Ssw[mm]	10.6	25.5
11	Rsw[mm]	71.6	26.6
12	Tsw[mm]	190.0	954.0
13	xmohyd[mms^{-1}]	8.38e-2	9.82e-2
14	xmopor[-]	0.487	0.33

3.4. Calibrated Results

3.4.1 Calibrated Parameters

The parameter values obtained through calibration for the two sub-basins are listed in Table 3.2. The maximum vegetation fraction for the majority land cover in the forest sub-basin (woodland, 71% coverage, based on the PILPS 2e document) was changed from 0.8 in BATS (mixed woodland) to about 1.0 (full coverage) and its seasonal variation from 0.2 in BATS to 0.0 (no variation). The mountain sub-basin is mainly covered by shrub (64.3%, PILPS 2e document). The calibrated maximum vegetation fraction increased to 0.97 from 0.8 in BATS (deciduous shrub), and its seasonal variation (0.28) is close to that in BATS (0.30). In the experiment, for both vegetations, the Leaf Area Index (LAI) values (Table 3.1) were prescribed as recommended by PILPS 2e,

which were derived from the satellite NDVI data (Myneni et al. 1997; Nijssen et al. 2001) and considered more realistic than the LAI values provided by BATS. Table 3.2 also shows that (1) values of roughness height for woodland increased to 1.07 m from 0.8 m in BATS (1 m recommended by PILPS 2e) and for shrub decreased to 0.09 m from 0.1 m; (0.15 m recommended by PILPS 2e), and (2) vegetation interception increased to 0.24 mm for woodland and 0.15 mm for shrubs from original 0.1 mm in BATS. Previous studies (such as Pitman et al. 1999; Gao et al. 1996) indicate that vegetation parameters are sensitive to land-surface hydrology; however, there is no sufficient observation data to quantify the correct values. The changed values after calibration indicate that forest has smaller seasonal variation of coverage and higher precipitation interception than shrubs, which seems fairly realistic.

It is well known that soil parameters are sensitive to the performance of land-surface models and many efforts have been made to “standard” soil parameters (FAO 1995; Mitchell et al. 1999; Gerakis 1999). The PILPS 2e project recommended three sets of soil parameter values of Clapp and Hornberger (1978), Cosby et al. (1984), and Rawls et al. (1982), which are relatively close to the values used in BATS based on Campbell (1984) and Clapp and Hornberger (1978). The calibrated values for the selected two soil parameters: porosities and saturated soil hydraulic conductivities, for both sub-basins are comparable to those recommended in PILPS 2e (sandy loam) and used in BATS (soil #4). The calibrated soil porosity for the mountain sub-basin (0.33) is smaller than that for the forest sub-basin (0.48) because the mountain sub-basin has abundant sand (~70%) with smaller voids compared with the soil (~54% sand) in the forest sub-basin.

The calibration results for the runoff partition factors (C_1 , C_2 , C_3 , and C_4) indicate that the root zone subsurface flow (R_4) contributed 97% of runoff to the total streamflows in both sub-basins. The values of C_2 were very small (<0.01) to remain the low deep drainage and relatively high (deep layer) soil moisture in the sub-basins. Both C_1 and C_3 were close to zero, which means that the quick runoff components of overland flow and top-layer subsurface runoff were insignificant in the streamflows.

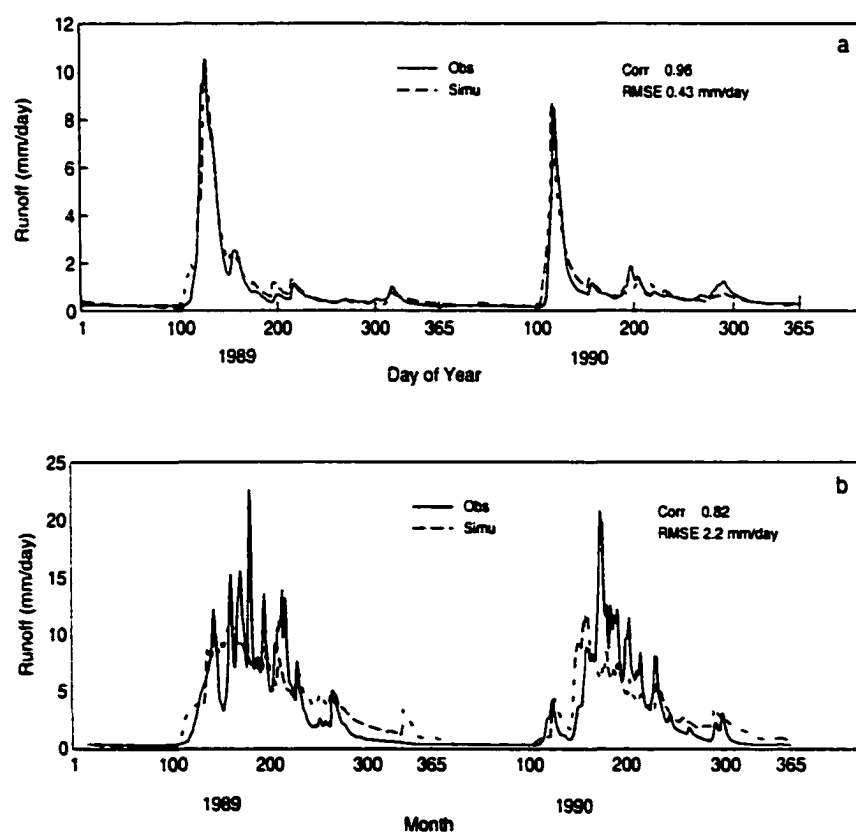


Figure 3.2 Comparison of daily runoff predicted by the calibrated SAST scheme with observations during 1989-1990 for (a) the forest sub-basin and (b) the mountain sub-basin.

3.4.2 Calibrated Runoff

The calibration results of daily runoff in the sub-basins for 1989-1990 are plotted in Figure 3.2. Comparing with the uncalibration results (Figures 3.1b and c), the accuracy (RMSE and Correlation) of runoff simulation was substantially improved. The 10-year (1989-1998), uncalibrated vs. calibrated-validated runoff results for the two sub-basins are compared in Figure 3.3. The RMSE (basin area average) and correlation for the 10-year calibration-validation data are 0.40 m/s and 0.94 for the forest sub-basin and 0.59 m/s and 0.92 for the mountain sub-basin, respectively. These long-term results indicate that the accuracy for runoff prediction was significantly improved through the model modification and calibration and that the runoff formulation and parameters in the revised model seem representative of the two sub-basins. It is important to understand how these parameter adjustments affected the runoff simulations and what internal physical processes changed. To address these issues, the calibration results were compared with the results of “sensitivity runs” in which one or two parameter values were perturbed from the calibration values to the uncalibration values (given in BATS). For simplicity, only the hydrology in the forest sub-basin is presented.

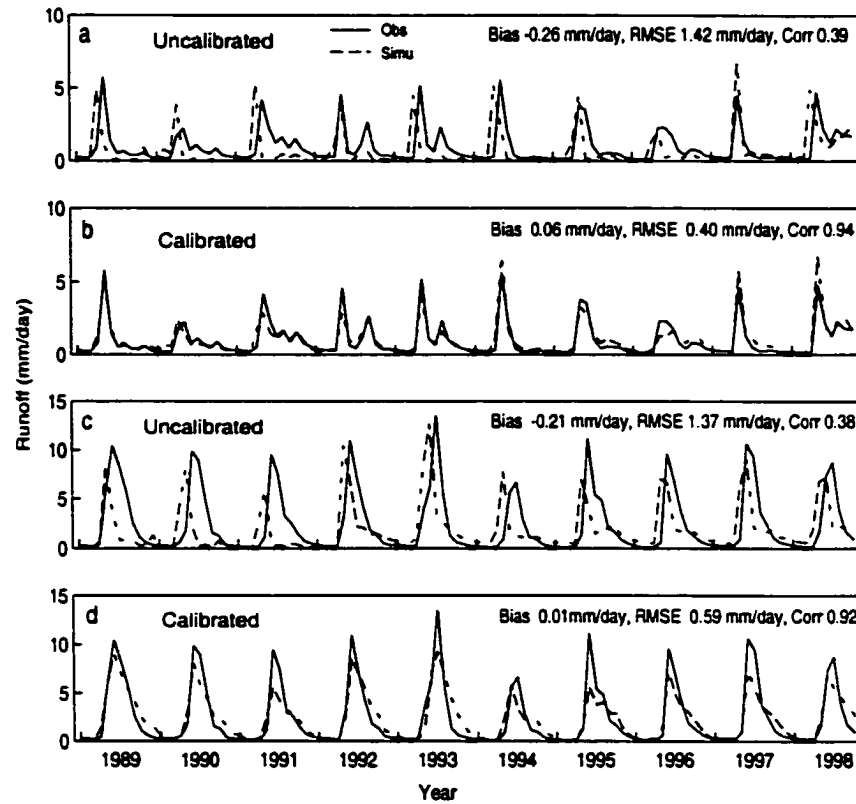


Figure 3.3 Comparison of 10-year runoff predicted by the uncalibrated and calibrated SAST scheme with observations for the forest sub-basin (a) uncalibrated and (b) calibrated, for the mountain sub-basin (c) uncalibrated and (d) calibrated.

3.4.3 Vegetation Cover

In Figures 3.4 and 3.5, the 1989-1990 calibration results for the forest sub-basin are compared with the sensitivity results with the values of maximum vegetation fraction and its seasonal variation changed from the calibration values (1.0 and 0.0) to uncalibration (BATS) values (0.8 and 0.2). This sensitivity run is to test the impacts of varying (decreasing in this case) vegetation coverage on the hydrological processes in the forest sub-basin. In Figure 3.4, the (10-day averaged) variations of runoff, snow (snow water equivalent, SWE), and snowmelt (SM) are presented. The runoff data (Figure 3.4a) indicate that the decrease in vegetation cover resulted in an RMSE increase from 0.40 m/day (calibration vs. observation) to 1.45 m/day (sensitivity vs. observation). The runoff in the sensitivity case (dashed line) reached peak flow about 20 days earlier than in the calibration case (solid line) and, in 1989, annual runoff in the sensitivity case was larger than in the calibration case but in 1990, the situation was reversed. In Figures 3.4b-c, the snow (SWE) and snowmelt data shows that, in 1989, more snow accumulated before the spring melting in the sensitivity case because the smaller vegetation cover reduced the snow interception and allowed more snowfall to reach the ground. In 1990, certain early snowmelt events occurred during the snow accumulation period, and the melting was stronger in the sensitivity case than in the calibration case; therefore, less snow was available for the spring runoff. Figures 3.4b-c also show that, in the sensitivity case, snowmelt ended about 10 days earlier than in the calibration case. To explain the cause of such snowmelt features, the major net energy fluxes at snow surface are presented in Figure 3.5. From Figure 3.5a, it appears that, in the calibration case (solid line), the snow

surface received no solar radiation because it was almost fully covered by forest canopy, and the weak solar radiation at the high latitude site was unable to penetrate the canopy to the ground surface. Meanwhile, in the sensitivity case (dashed line), the shrunk vegetation cover caused the snow cover to be partially exposed to the open air to receive direct short-wave radiation. Notice that (1) the net solar radiation (although received by a portion of snow cover) provided the major energy for the spring snowmelt in the sensitivity case, and (2) the net solar radiation on the snow surface became almost negligible in the winter due to the very weak solar radiation in high-latitude. The situation of net long-wave radiation (Figure 3.5b) was just the opposite: in the calibration case (solid line), net long-wave radiation turned from negative to positive in spring (because of the warm-up of the canopy) and provided energy for snowmelt, however, in the sensitivity case (dashed line), the net long-wave radiation remained negative (because the snow cover partially emitted to the open air). Sensible heat flux is another major energy component affecting snow cover in the region (Figure 3.5c, upward flux as positive). In the calibration case (solid line), the direction of sensible heat flux kept downward (negative), which warmed the snow. In the sensitivity case, the downward sensible heat flux was even stronger. However, sometime during later fall and early winter, the upward sensible heat fluxes on the snow surface (cooling the snow) occurred because of the cold temperature of the open air. Clearly, the description of vegetation cover in the model could sensitively influence the radiation transfer and surface energy processes and result in significant discrepancies in hydrology.

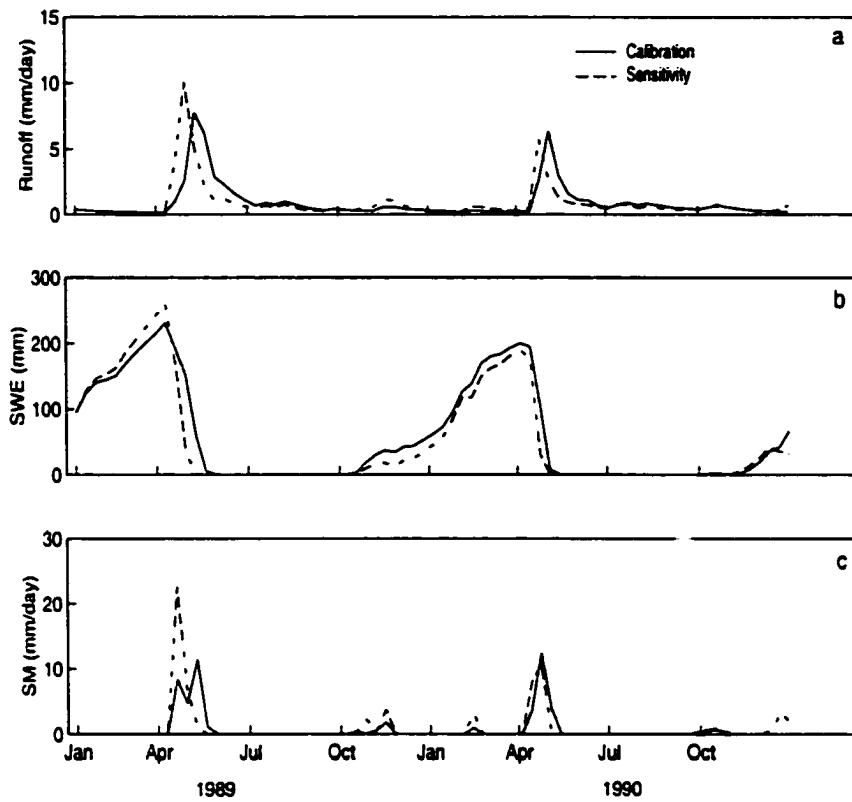


Figure 3.4 Comparison of the calibration results of (a) runoff, (b) SWE, and (c) snowmelt (1989-1990) with the sensitivity results with vegetation coverage reduced from the calibrated values to the BATS values for the forest sub-basin.

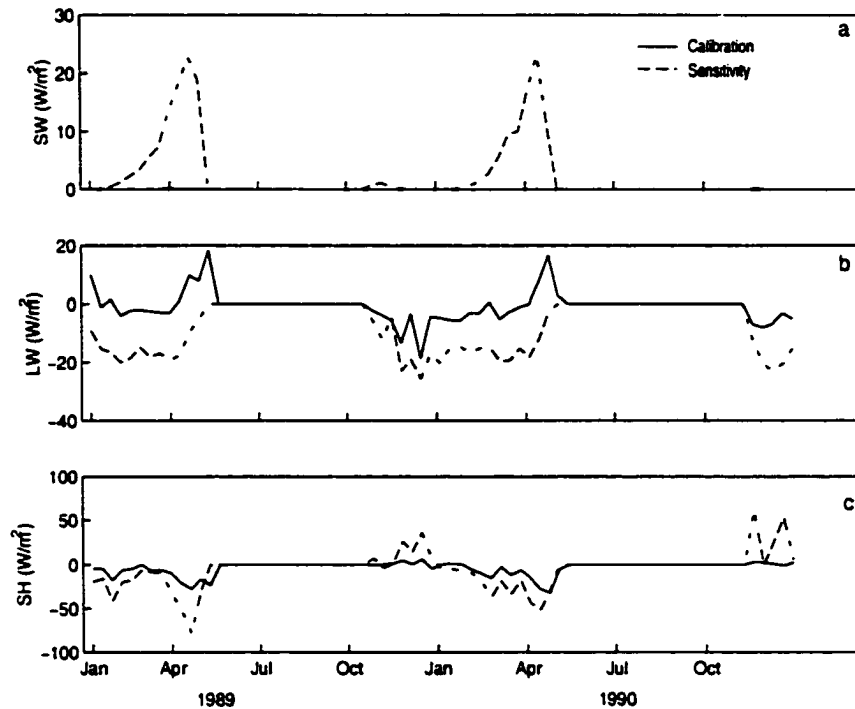


Figure 3.5 Comparison of the calibration results of the major energy components on snow surface: (a) net solar radiation, (b) net long wave radiation (positive for downward flux), and (c) net sensible heat flux (positive for upward flux) for the forest sub-basin (1989-1990).

3.4.4 Vegetation Roughness Height

After changing the calibration values (1.07 m) of vegetation roughness to the uncalibrated (BATS) value (0.8 m), the RMSE of runoff in the sensitivity case increased from 0.40 m/s to 0.49 m/s. In Figure 3.6, the decrease in roughness height (dashed line) resulted in a delay of about 10 days of the peak runoff, more snow accumulated before mid-spring, and slower snowmelt than in the calibration case (solid line). The examination of energy balance at the snow surface indicates that the decrease in vegetation roughness height resulted in smaller downward sensible heat flux on the snow

surface (Figure 3.6d) because of the depression of the mass and energy exchange between snow surface and overlying atmosphere (surface drag coefficient). The decreased downward sensible heat flux led to slower snowmelt rates and higher snow depth, which was responsible for the later runoff peak flow.

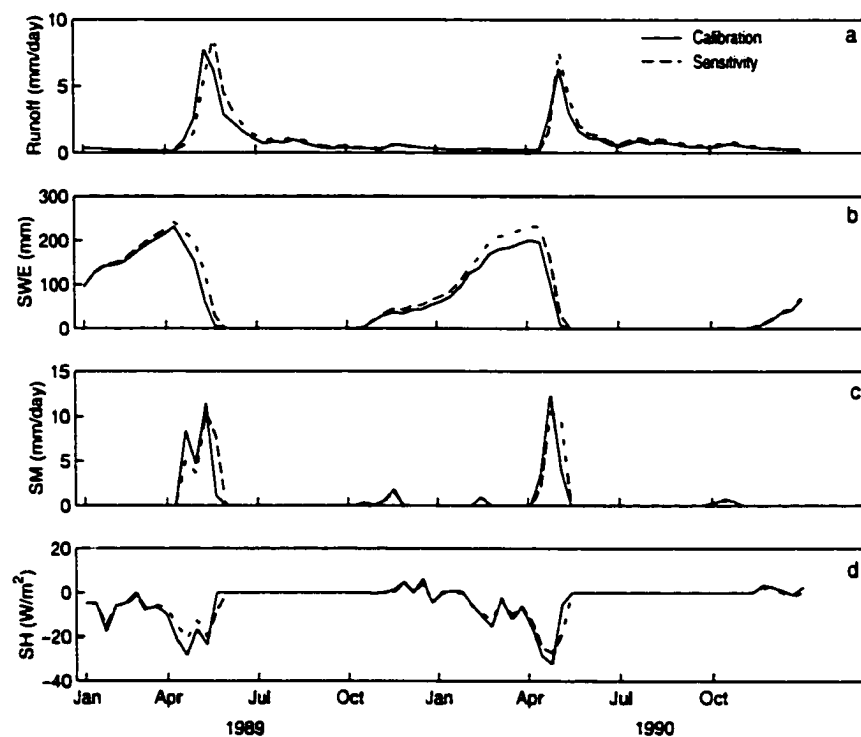


Figure 3.6 Comparison of the calibration results of (a) runoff, (b) SWE, (c) snowmelt, and (d) net sensible heat flux on snow surface with the sensitivity results with vegetation roughness height reduced from the calibrated values to the BATS values for the forest sub-basin.

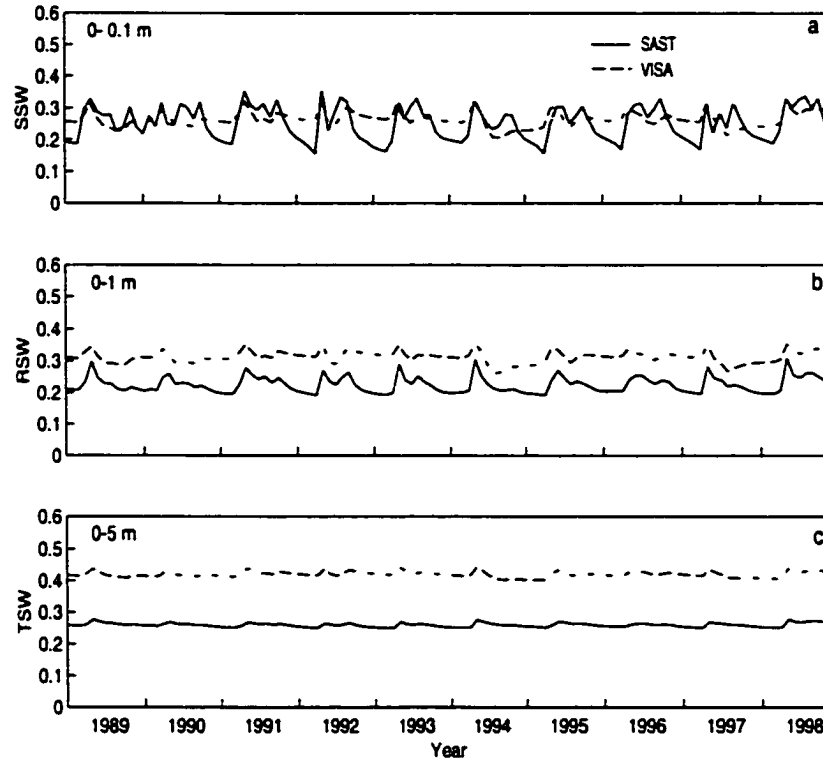


Figure 3.7 Comparison of 10-year soil-moisture variations predicted by the SAST and VISA models: (a) top soil layer (0-0.1 m depth), (b) root zone layer (0-1 m depth), and (c) total layer (0-5 m).

3.4.5 Soil Moisture

The variations of monthly-mean soil moisture (solid line) during the calibration-validation period (1989-1998) are plotted in Figure 3.7. In the top layer (surface to 0.1 m depth), the annual averaged soil water density (SSW, in m/m) was 0.28, slightly wetter than the soil field capacity (0.26); the top layer was frequently saturated (soil porosity: 0.48) during the spring snowmelt events (days). In the root zone layer (surface to 1 m depth) and the deep layer (surface to 5 m depth), the soil water density changed to 0.25

and 0.27, respectively. The interannual patterns of soil-moisture variation indicate that the water balance of land surfaces in the simulation reached the quasi-equilibrium condition. The seasonal pattern of soil moisture was typical for the three layers: it reached peak values rapidly in mid-spring due to the heavy snowmelt and dried out substantially afterwards; in summer, there were several wetting surges on the drying tendency responding to the residual snowmelt and rainfall events, but in fall and winter, the soil kept drying at a slow course after the freezing of soil. This simulated variation of soil moisture seems reasonable. However, when the 10-year-averaged annual soil moisture was compared with the soil moisture predicted by the (calibrated) VISA model (Niu and Yang 2002) for the same sub-basin (dashed line), significant diversity was discovered. The VISA soil moisture was much wetter and less variable than that of SAST. The reason is that, model runoff formulation is related to soil moisture in SAST, but to water table height in VISA. It is also found that, the parameter value ρ_0 in Eqs. 5 and 6 is sensitive to the mean values of soil moisture in the layers. If increasing the value ρ_0 , and re-calibration the model, the mean soil moisture can be raised and the accuracy of runoff prediction still keeps the same. Currently, there were no measurement data in the region available for evaluation, but it can be concluded that, for a land-surface model, matching runoff well with observations is not sufficient to determine the correct status of soil moisture described in the model. More aspects of land-surface hydrology should be checked through observation data.

3.5 Overall evaluation of SAST model in PILPS2e experiments

With the re-formulated runoff scheme and the optimized parameter set, performances of the SAST model over entire PILPS2e study area are evaluated in comparison with observations and the outputs from the other 20 land-surface models participating in the experiments. PILPS2e study area includes Torne and Kalix watersheds in northern Scandinavia, with a total area of about 58,000 km². Observations over these two watersheds used in PILPS2e experiments were collected by the Swedish and Finnish meteorological and hydrological institutions. Detailed descriptions of experimental design, forcing data, ground observations, and submitted results have been carried out by Bowling et al. (2002) and Nijssen et al. (2002). In this section, we mainly discuss runoff and surface turbulent flux simulations from 21 models. The figures are taken from Nijssen et al. (2002) with permission. Figure 3.8 shows that observed and simulated monthly runoff over Kalix and Torne basins. All models capture the basic trend of seasonal changes in runoff, which usually reaches peak during the snowmelt season and is very low in other seasons. Therefore, snowmelt water is a major contributor to the discharge in these two water basins. Some models such as CLASS from Canada, HY-SSIB from NASA, and SWAP from Russia overestimate the peak flow while some others such as ECMWF, MOSES, and MOSES-CEH from United Kingdom intend to predict lower peak flow, which result from biases in simulated snow amounts in these models (Figure not shown). The SAST model has a very good agreement with observations from the Kalix and Torne basins on a monthly time scale. Figure 3.9 shows exceedance frequency versus daily discharge, which indicates the frequency at which thresholds for

daily discharge are exceeded. Usually, peak flows have a low frequency because they mainly occur in snowmelt season while base flows have a high frequency since they exist almost in all seasons. Thus, exceedance frequency can be used to evaluate modeled peak and base flows in comparison with observations. Figure 3.9 shows that all models have good simulations for peak flows, while about half models do not simulate well for base flows. The SAST model performs well over the entire frequency domain. Simulated discharge on a daily scale can be evaluated by a Taylor diagram (McAvaney et al. 2001) in Figure 3.10. In this figure, distance from the origin to a plotted point stands for a standard deviation for simulated discharge which has been normalized by that for observations, while cosine of azimuth angle represents the correlation between daily flow anomalies from observations and simulations. The coordinates for the SAST model from both Kalix and Torne basins (N and n) are very close to observations at (1,1). However, the models with an earlier snow melt are poorly correlated with the observed daily runoff (NOAA: P and p, ECMWF: S and s, MOSES: T and t, and MOSES-CEH: U and u) while those with a higher peak flow demonstrate a greater variance than observations (SPONSOR: A and a, CLASS: G and g, IBIS: H and h, CHASM: I and i, HY-SSIB: L and l, and SWAP: Q and q). Figure 3.11 illustrates modeled latent and sensible heat fluxes. The averaged latent heat flux over the Torne and Kalix watersheds from the SAST model (N) agrees well with an estimated latent heat flux based on water balance. Sensible heat flux simulations show a strong diversity. The models A-J have positive values and other models give about zero or negative values. The SAST model (N) has

about -5.0 W/m^2 sensible heat flux. It is difficult to make a reliable evaluation to the models because of absence of observation for this variable.

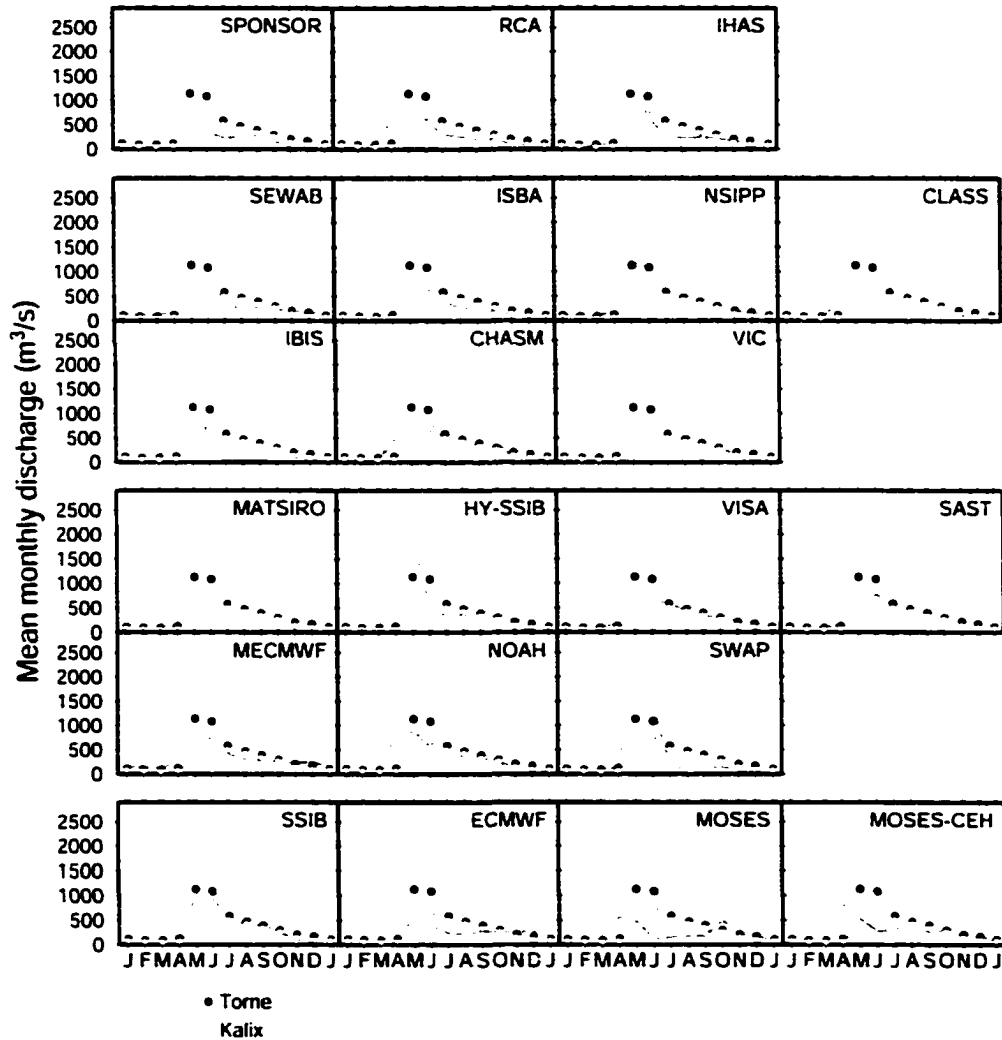


Figure 3.8 Mean monthly observed (dots) and simulated (lines) discharge for the Kalix and Torne river basins (Nijssen et al. 2002).

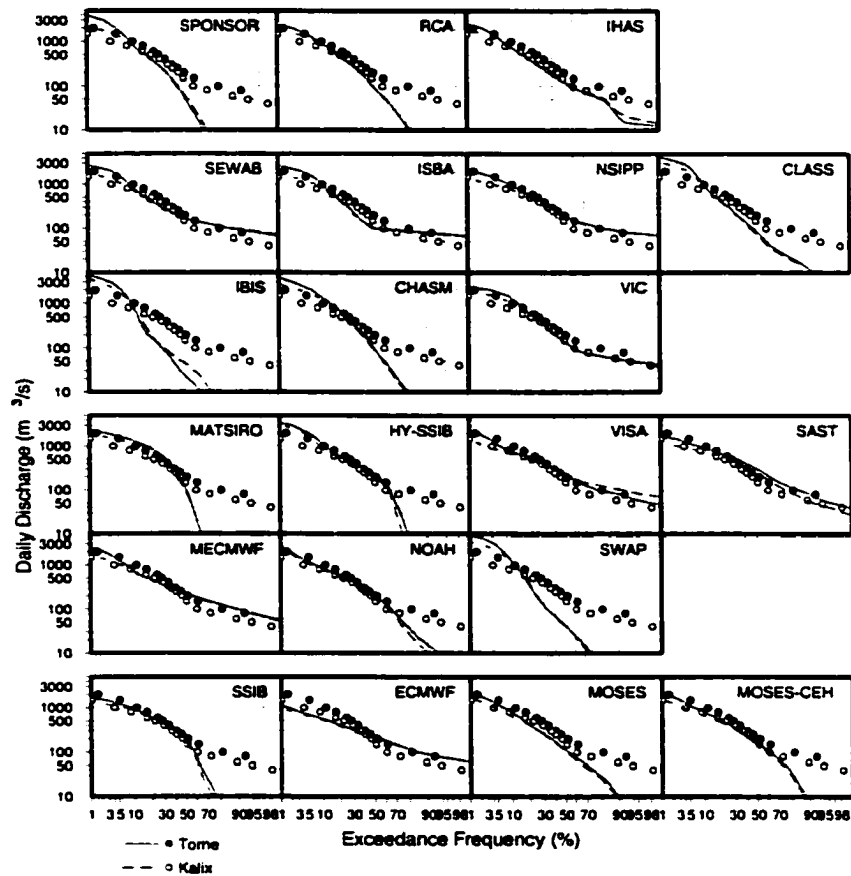


Figure 3.9 Flow duration curves based observed (dots) and simulated (lines) daily flows from 1989-1998 (Nijssen et al. 2002).

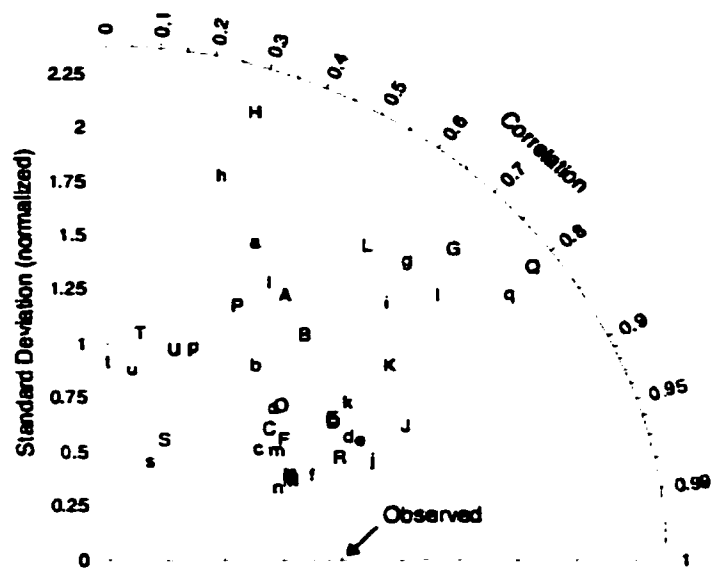


Figure 3.10 Talor diagram of daily flows from 1989-1998. Upper-case letters represent flows at the mouth of the Kalix, lower-case letters represent flows at the mouth of the Torne (Nijssen et al. 2002).

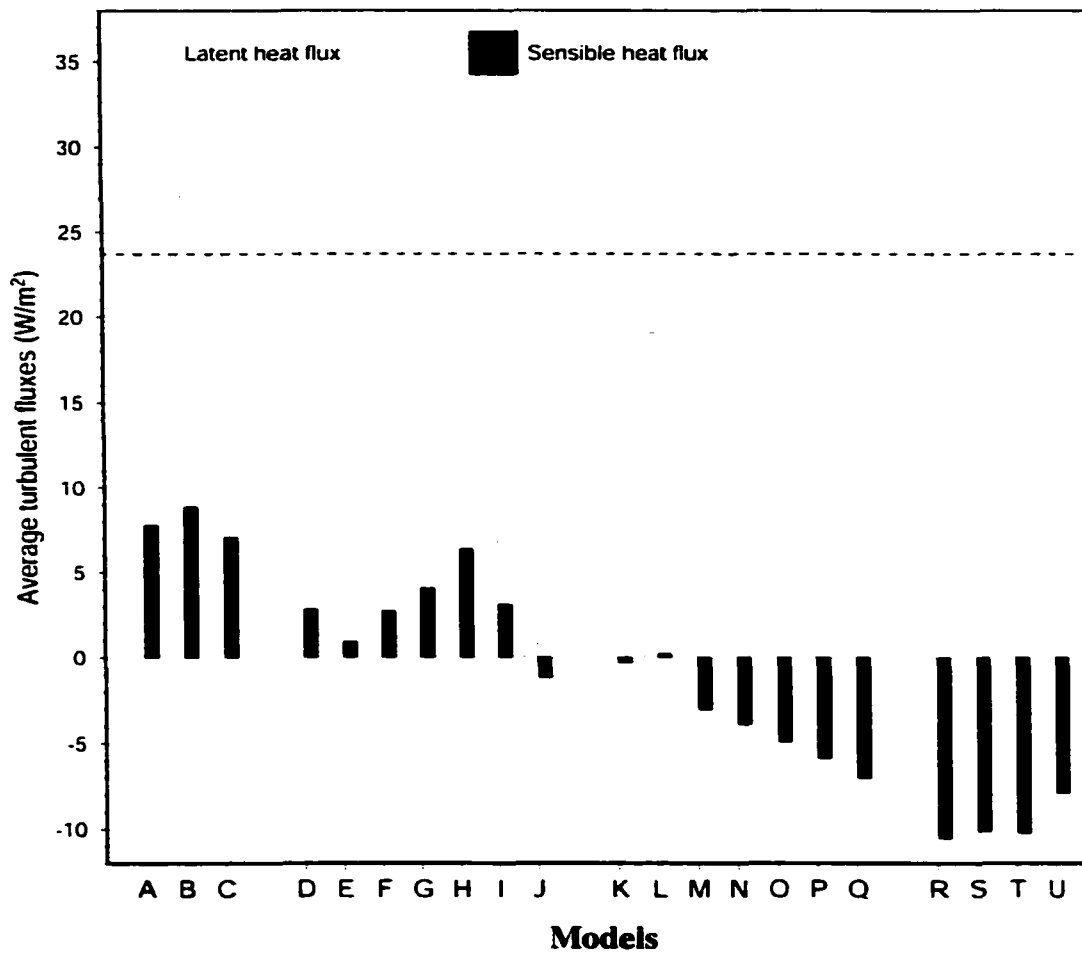


Figure 3.11 Mean annual basin-wide turbulent heat fluxes. The dashed line shows the water balance based estimate of the latent heat flux over the basin. Letter 'N' is the SAST model (Nijssen et al. 2002).

3.6 Discussion and Conclusions

In this study, the performances and improvements of the SAST model through the PILPS 2e calibration-validation experiments are addressed. First, the uncalibration results exposed significant model deficiencies to accurately simulate streamflow patterns and quantities observed in the sub-basins. These model deficiencies were recognized, including two major issues: (1) the model runoff formulation misses subsurface runoff with proper response time to match the phase features of peak runoff responding to the heavy spring snowmelt events in the sub-basins, and (2) the values of soil and vegetation parameters prescribed by the model were different from those recommended by the PILPS 2e document which are based on historical and observation data. Through modification in the runoff-generation scheme and calibration of parameters, the revised model showed significant improvements in runoff simulation, and the capability of runoff prediction for the sub-basins was verified well through the results of an 8-year extended run. As to model performance of other aspects of hydrology, there were no observation data to evaluate; however, model-described snow processes regarding the mass and energy transfer in the land-surface were plausible.

The automatic calibration scheme of SCE was found to be not only helpful in searching the parameter set for the “best” model performance, but in identifying some realistic features in the land surface hydrology. The determination of the runoff weight factors through calibration explored the realistic partition of runoff components in the sub-basins. It also seemed realistic that, after calibration, the seasonal variation of forest coverage in the region was less than that of shrubs, which indicates that the dominant

snowmelt energy in the forest fields is the downward sensible heat flux and canopy long-wave radiation, while the major snowmelt energy in the shrub fields is the solar radiation. However, it should be pointed out that the values of parameters could be highly “model-dependent”. For example, the parameters of vegetation fractional coverage are used in the SAST and BATS models to determine the fraction of solar radiation on the ground surface. The sensitivity experiment indicates that the values of these parameters need to be adjusted for better performance (especially after the vegetation LAI values has been prescribed to NDVI-based values as suggested by PILPS 2e document). However, for some other land-surface schemes (such as Bonan 1996; Zeng et al. 2000), vegetation fraction coverage was fixed, and the effect of solar radiation on the surface was sensitive to LAI. Therefore, the explanation and transfer of calibrated parameter values should remain for the same model.

Correct soil-moisture calculation is one of the major objectives of using land-surface parameterization schemes in the coupled atmospheric model. The soil-moisture data and their spatial and temporal variation patterns simulated by the revised SAST model seem reasonable; however, when compared with the results of other models, such as VISA, significant diversity was discovered. This diversity indicates that in addition to runoff and precipitation, more aspects of land-surface hydrology should be observed to evaluate the performance of a land-surface model.

The general evaluation of the models participating in PILPS 2e experiments indicates that the SAST model has a very good performance for monthly and daily runoff simulations as well as peak and base flow simulations. This model also captures the

characteristics of latent heat flux over the basin in comparison with an estimated value based on the water balance.

Finally, the SAST model is developed for the use of GCMs, and the model deficiencies were discovered when the model was applied to the environment very different from those in GCMs. First, the PILPS 2e runoff was from a small river basin, but GCM runoff is from a much larger grid cell. Many studies have indicated that BATS runoff scheme performed relatively well in large scale simulation (Oki et al. 1999; Hahmann and Dickinson 2000); second, because previous studies have shown that the features of GCM precipitation generated from the atmospheric model are very different from those of observations, which are in extreme high frequency and low intensity (Gao et al. 1994; Chen et al. 1996), therefore, whether or not the revision of the model will improve its performance in coupled GCM application is a topic for the future study.

4. ASSIMILATION OF REMOTELY-SENSED SNOW DEPTH IN GCM OVER THE ROCKY MOUNTAINS

4.1. Introduction

Nearly 85% of the total annual streamflow over western North America is derived from the snowpack in the Rocky Mountains (Grant and Kahan, 1974). Therefore, understanding the mechanisms of snow variability is important for streamflow forecast and climate studies. Many authors indicate that snow variations in the region result mainly from anomalous atmospheric circulation patterns (Cayan 1996; McCabe and Dettinger 2001; Changnon et al.1993). Using the principal component analysis (PCA), Cayan (1996) found that the loadings of the first five components of PCA could represent five different snow regions in the western U.S. The snow variations in these five regions resulted from anomalous precipitation that was associated with the different atmospheric circulation patterns and temperatures had a secondary effect on the snowpack, which implies that precipitation variability is a key issue for snow variations. McCabe and Dettinger (2001) found that atmospheric patterns connected with snowpack variability in the western U.S. related to indices of Pacific Ocean climate.

Anomalies of the snowpack also affect surface climate variability and the thermal and dynamic structure of the atmosphere. Yeh et al. (1983) found that decreased soil moisture resulting from a sudden removal of snow cover in a simplified GCM persisted for the entire spring and summer. At the same time, the increase in surface temperature caused by the snow-free surface extends into the upper troposphere thereby reducing both

meridional temperature gradient and zonal wind in high latitudes. Cess et al. (1991) intercompared 17 general circulation models. They found that snow feedback amplified global warming in some models and moderated it in others. These feedbacks result mainly from both cloud interactions and long-wave radiation instead of albedo. Groisman et al. (1994) indicate that the snow-induced increase in surface air temperature over the Northern Hemisphere has been greater in spring than in any other season on the basis of an analysis of satellite-derived snow cover, radiative balance, and surface air temperature. An observational study by Namias (1985) also indicates that the variability of snow in the Rocky Mountains exerted strong influences on climate fluctuation of local and down stream regions.

Our study indicates that CCM3 greatly exaggerates snow depth over the Rocky Mountains. In addition, the model output shows that winter and spring precipitation has been overestimated and surface air temperature underestimated in the region. The same conclusion was also drawn by Bonan (1998). As we know, thicker snow is usually connected with colder climate (Namias, 1985) and stronger precipitation (McCabe and Wolock 1999). Thus, the percentage of contribution of the overestimated snowpack to erroneous surface air temperatures and precipitation in CCM3 is an important part of local climate variability and model development. The problem is identified through the assimilation of remote-sensing data. The reliability of the dataset used in this chapter was verified by Chang et al. (1990) and Forster et al. (1987) and its only shortcoming is that its time series is short for climate studies. In this chapter, monthly remotely-sensed snow

depth data are averaged over ten years (1978-1987) to approximately represent snow depth climatology.

4.2.Model

We use CCM3 (Kiehl et al.,1996) with 18 vertical atmospheric levels extending from the surface boundary layer to the 2.9mb level, and a horizontal grid of approximately $2.8^\circ \times 2.8^\circ$. The original land surface model (LSM) (Bonan, 1996) is replaced by SAST (Sun et al. 1999; Jin et al. 1999b) in which the sophisticated physical processes of snow and soil are addressed. This SAST has three snow layers complied with energy and mass balances. In snowpack, liquid water is treated as a concept of the liquid water-holding capacity parameterized as a function of snow density, and water vapor is ignored. The grain size of snow used for calculating liquid water transfer is also treated as a function of snow density. A snow depth of less than 5-mm is included with soil. Soil is divided into 10 layers in which temperature and moisture are solved with energy and mass balance equations. Thermal conductivity and heat capacity of soil when the temperature is below the freezing point is modified for frozen soil. We use BATS (Dickinson et al., 1993) for vegetation.

Vegetation, soil, and snow are mixed in a grid square of 2.8° by 2.8° . The methodology of fraction calculations is adopted from BATS. Maximum and minimum vegetation fractions are prescribed and the variations between them are a function of soil temperature at 1 m. Snow fraction is a function of roughnesses of vegetation and soil and bare soil fraction is the part of the grid box excluding snow and vegetation.

4.3. Data and Methodology

Two model runs were performed using the same initial and boundary conditions except for snow depth. The two runs were started on September 1 and forced with a climatological annual cycle of SST for 12.3 model years. The first 16 months of simulation were discarded from our analysis and the remaining 11 years of data were averaged as climatological data. For convenience, the original model run is defined as 'control run' and the model run connected with remotely- sensed data is the 'assimilation run'.

The snow depth data used for assimilation is the passive microwave data derived from the Nimbus-7 Scanning Multi-channel Microwave Radiometer (SMMR) (Chang et al. 1990); Forster et al. 1987). This monthly dataset is from 1978 to 1987 and has a $0.5^\circ \times 0.5^\circ$ horizontal resolution for global land. The data were averaged for snow climatology as mentioned above and interpolated to CCM3 resolution for the purpose of the assimilation. Observed snow water equivalent was estimated from the snow depth by assuming a snow density equal to 300 kg/m^3 (Foster et al. 1996; Fei and Robinson 1998). For convenience, the snow water equivalent used in this chapter is defined as "snow depth" and the real snow depth will not be addressed.

The monthly reanalysis data for the 500 mb geopotential height and zonal wind fields and the soil moisture field for the 2 m soil depth obtained from National Centers for Environmental Prediction (NCEP) have been used to evaluate CCM3 output. Originally having a $1.875^\circ \times 1.875^\circ$ horizontal resolution and a 18-year length from 1979

to 1996, this dataset was interpolated to CCM3 resolution and averaged as the climatology.

Legates and Willmott (1990a,b) global climatologies for precipitation and 2 m height surface air temperature were used to evaluate CCM3 output from both runs, where land for both fields is based on historical measurements from global meteorological stations.

The assimilation process we use is an artificial method which is an organic mixture of observations and numerical modeling. As mentioned above, this SAST coupled with CCM3 is an energy and mass balance model. The heat fluxes absorbed by snowpack are from vegetation and/or atmosphere as well as soil surface, which firstly are used to change snow temperature. Then, if the snow temperature is at the melt point, the extra heat fluxes are applied to melt snow. Before assimilation, the monthly SMMR snow depth data were sliced to an interval of 20 minutes so that the snow depth calculated in CCM3 could be replaced by SMMR data at the CCM3 time step. In the course of the replacement, snow accumulation and melt were controlled by SMMR data instead of CCM3 calculations. In other words, snowfall and snowmelt were observed variables for input in the place of model calculations. Throughout the assimilation processes, the energy and mass balances were artificially retained in the model. For the snow accumulation process, if the model calculated snowfall was larger than input, the additional part was assigned to runoff. For the opposite condition, the insufficiency could be compensated for by runoff. If the runoff still could not counterbalance the insufficiency, the deficit was obtained from total soil moisture based on 5 m thick soil.

However, this has never happened in the assimilation run because of the strong precipitation over the Rocky Mountains during the snow season (this will be discussed further later).

In the course of snowmelt, the input snow melt was first converted to heat flux. If the model calculated heat fluxes for snow melt were larger than those converted (from input snow melt), the excess heat fluxes were assigned to the soil. Under an inverse condition, the insufficient energy was manually gained from the soil. This energy balance process is vital to surface temperature simulation and will be discussed further later. Furthermore, although snowfall, snow melt, and snow depth in the model were substituted for observations, the snow model was still important to the assimilation process because the model calculated snow melt is a key variable for redistribution of energies.

The above assimilation process might have caused some errors because the interpolation of the monthly snow depth data into the 20-minute interval (CCM3 time step) probably resulted in a discrepancy of data from reality. Nevertheless, the monthly means of model output could greatly diminish the influences of data interpolation.

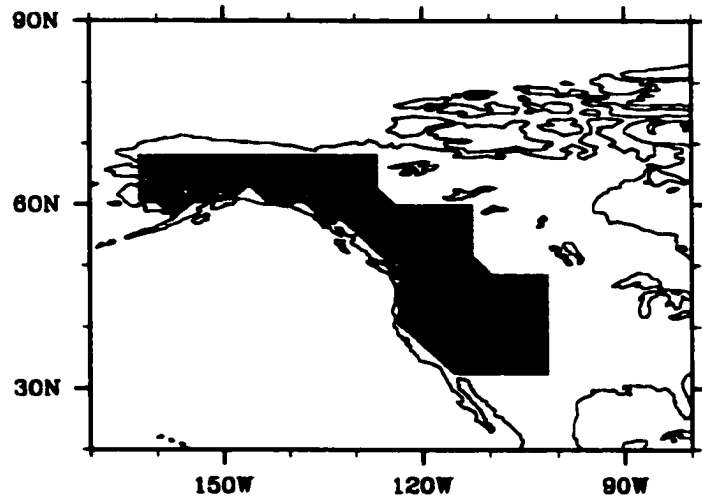


Figure 4.1 Area for the assimilation of snow depth in CCM3 over the Rocky Mountains.

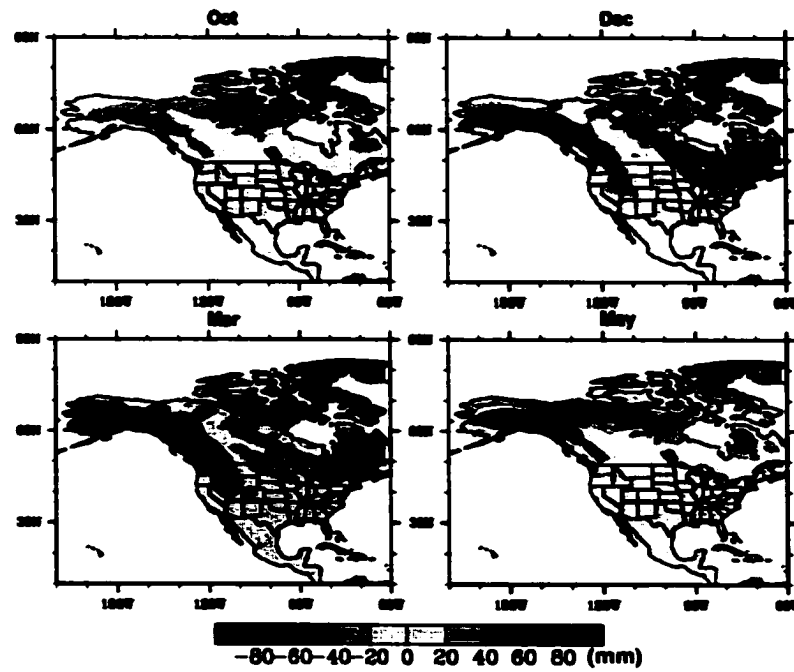


Figure 4.2 Differences in snow depth between CCM3 output and SMMR data over North America (model output minus SMMR data).

4.4 Results

4.4.1 Geographic distribution of the difference between simulated and observed snow depth over North America

Figure 4.1 shows the definition of the Rocky Mountains where the assimilation processes have been carried out. Figure 4.2 is the difference in snow depth between model output and SMMR data over North America for October, December, March, and May, where October and December stand for the snow accumulation period, March stands for the peak snow period, and May stands for the snow melt period in the Rocky Mountains. This figure indicates that snow depth was seriously overestimated in the Rocky Mountains during the entire snow season and the maximum difference averaged over the entire region is about 10 cm. In the middle part of the North American land adjacent to the east of the Rocky Mountains, snow depth was slightly underestimated during most of the snow season, which was probably caused by the drier downhill air flow. In eastern and northeastern North America, snow depth was mostly overestimated for the snow accumulation and peak periods and underestimated for the snow melt period. In comparison of SMMR dataset, the snow depth observations taken from the US Air Force Environmental Technical Applications Center (USAF/ETAC) at Scott Air Force Base in Illinois (Foster and Davy, 1988) have a different conclusion over the eastern and northeastern North America for the different snow periods. However both datasets have the same consequence in the Rocky Mountains, which is the main reason that this chapter just focuses on this region. At the same time, the snow models with different complexity (for example, SAST with three snow layers: Jin et al. 1999b and

BATS1e with one snow layer: Dickinson 1993) coupled with CCM3 commonly produced the positive biases compared with both SMMR and USAF/ETAC datasets (Figure not shown).

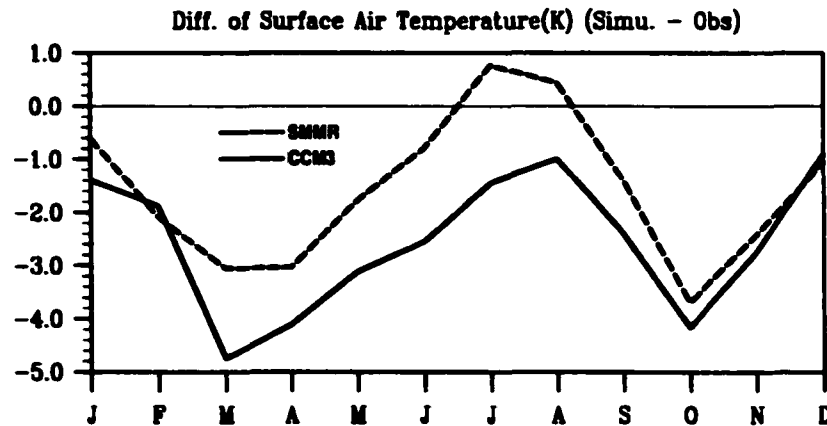


Figure 4.3 Surface air temperature differences between CCM3 output and observations before (solid line) and after (dashed line) snow depth assimilation (CCM3 output minus observations).

4.4.2 Surface air temperature at 2 m.

The air temperature at 2 m is considered one of the most important indicators of surface climate change and the accurate prediction of surface air temperature at 2 m can provide evidence of future climate conditions. Compared with the Legates and Willmott (1990) temperature climatology, our modeled surface air temperature shows a cold bias over the Rocky Mountains (Figure 4.1) for the entire period of the climate year (solid line in Figure 4.3). The greatest bias happened in the transition period of the year (cold valleys in March and October), which were about 5°C and 4°C lower than observations. Winter and late summer were simulated accurately than the other times. After the

assimilation of SMMR data into the model as discussed in section 2, the simulated surface air temperature improved for the overall year. For example, Table 4.1 shows that the average temperature for spring (MAM) had a 1.38°C increase and for summer (JJA) a 1.79°C increase, which were the most significant improvements. Nevertheless in the fall (SON) and winter (DJF), surface air temperature was not very improved with only 0.60°C and 0.14°C increases, respectively. The summer's temperature was even slightly higher than observations. Figure 4.3 also indicates that after the assimilation processes, snow-induced colder surface had been abbreviated to a great degree. However, cold valleys for the transition periods still existed, strongly suggesting that the forcings from CCM3 in the region probably have some biases.

Table 4.1 The seasonal bias between model output and observations for both runs (unit: °C). CTR is the control run and ASS is assimilation run.

	MAM	JJA	SON	DJF
CTR	-4.00	-1.66	-3.10	-1.39
ASS	-2.62	0.13	-2.50	-1.25
ASS - CTR	1.38	1.79	0.60	0.14

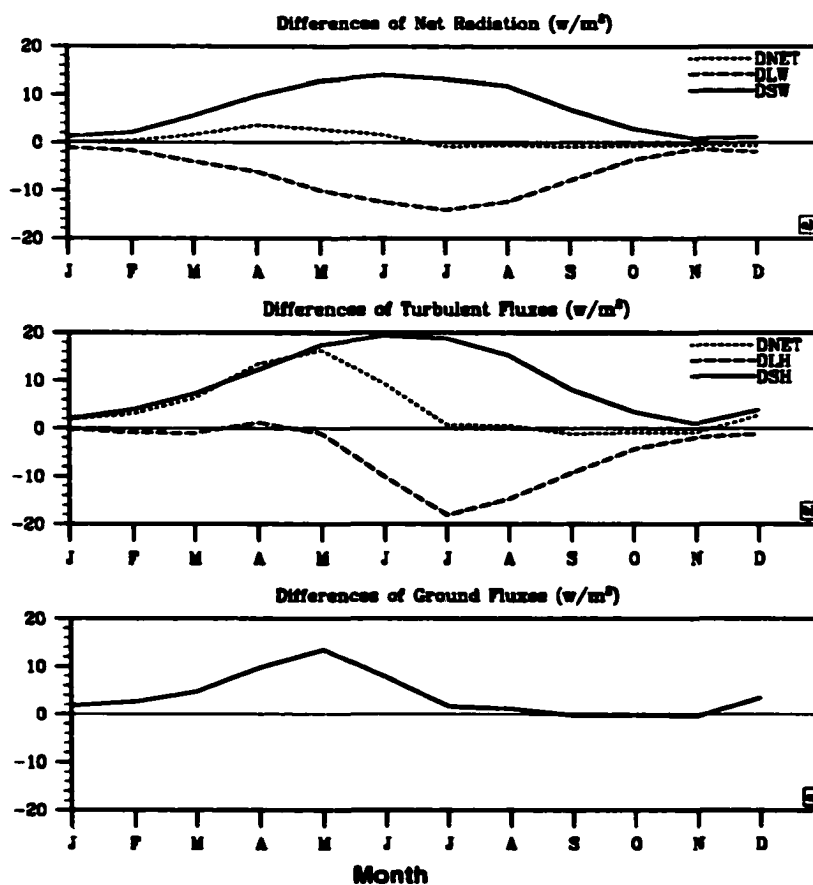


Figure 4.4 Differences between components in energy balance equation from the assimilation and control runs (assimilation minus control). a) solar (solid line), long-wave (dashed line), and net (dotted line) radiations, b) sensible (solid line), latent (dashed line) heat fluxes, and sensible plus latent (dotted line) heat fluxes, and c) ground flux to soil.

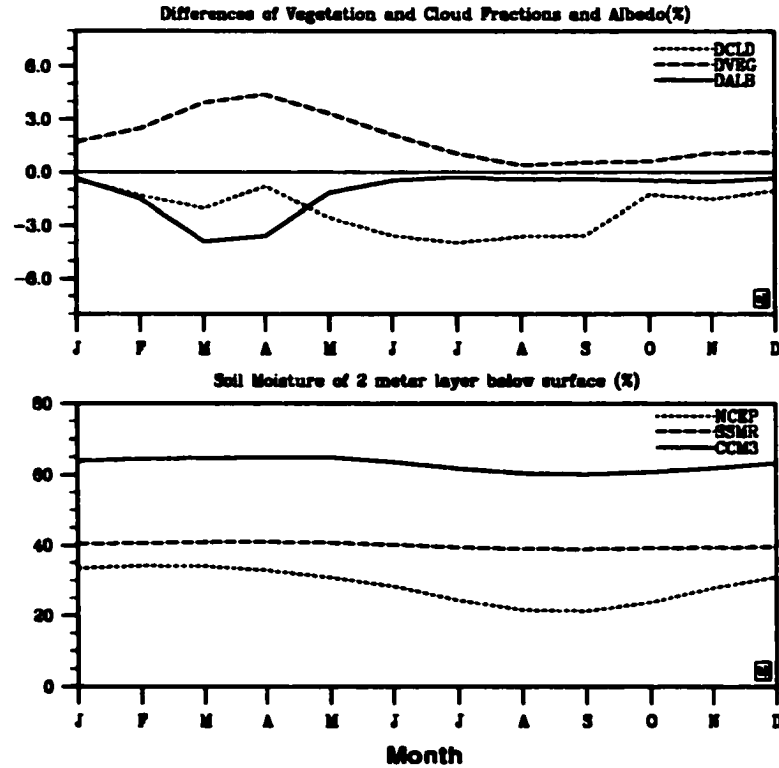


Figure 4.5 (a) Differences of vegetation and cloud fraction and albedo between the assimilation and control runs (assimilation minus control); (b) comparison of soil moisture from NCEP reanalysis data (dotted line), CCM3 control (solid line), and assimilation (dashed line) runs.

4.4.3 Energy balance

Figure 4.4 shows differences between the components of the energy balance equation from the assimilation and control runs (assimilation minus control). The sum of net radiation and turbulent fluxes is exactly equal to the ground heat flux for both runs, indicating the model's accuracy. Figure 4.4a represents that the surface radiation difference (solid line), which exhibits that the land surface absorbed more solar radiation

in the assimilation run than in the control run for spring, summer, and fall. Variations of surface albedo and cloud are two basic reasons for changes in solar radiation to the surface. The replacement of thicker snow in the control run by thinner snow in the assimilation run results in a decrease in snow fraction, a function of snow depth in the model. The decrease in snow fraction expands the vegetation fraction in the CCM3 grid boxes (dashed line in Figure 4.5a) and leads to a lower surface albedo during the snow season (solid line in Figure 4.5a), which is one reason for the stronger absorbed solar radiation in the assimilation run. The greatest changes in albedo and vegetation fraction occur in spring when snow depths had the largest differences between the two runs (Figure 4.2c). Vegetation fraction also had a small increase during the snow free season (July and August). This slight expansion was caused by the higher deep soil temperature in the assimilation run since vegetation fraction is parameterized as a function of soil temperature at 1 m deep in the model. On the other hand, cloud fraction also played an important role for the intensified absorption of solar radiation. Total cloud fraction decreased from the control run to the assimilation run for the overall period of the year, which introduced more solar radiation to the surface (Figure 4.5a). The most significant reduction of cloud fraction occurred during the warm season, which will be examined in detail later as part of the discussion of evaporation and surface heating.

Figure 4.4a shows that the net longwave radiation weakened in the assimilation run during the year and that the maximum decrease occurred in summer and the minimum in winter. Examination of the incoming longwave radiation indicates that the assimilation process did not produce much influence on the longwave radiation forcing

from the atmosphere (Figure not shown). Therefore, the land surface released energy through the longwave radiation because of the higher surface temperature, and the absorbed solar radiation was almost balanced by the outgoing longwave radiation, except for a slight remnant in spring (less than 4W/m^2 , dotted line in Figure 4.4a). Variations of net longwave radiation were mainly the result of the higher temperature instead of the reason of it.

Compared with the control run, the sensible heat flux increased in the assimilation run and had a summer maximum and a winter minimum (solid line in Figure 4.4b), which was consistent with the warmer surface (Figure 4.3 and Table 4.1). The latent heat flux decreased in summer and fall and had little change in winter and spring, and its variations were caused by surface temperature and soil moisture. As we know, snow is a major water resource for the western North America and the snow amount largely determines the soil moisture in the region. Figure 4.5b shows that after assimilating the thinner snow depth in the model, soil moisture had a 20% decrease for the entire period of the year, which greatly reduced the evaporation in the warm seasons (summer and fall). The drier soil during the snow seasons (winter and spring) did not cause much evaporation change resulted from cold land surface because of the presence of snow. These results suggest that the effects of anomalous snow cover on surface climate can last most of the year even without the presence of snow, and due to the low surface temperature, snow suppresses surface evaporation to a large degree. The variations of net turbulent fluxes (dotted line in Figure 4.4b) had positive values in the spring and early summer and nearly balanced each other for the rest of the year. Turbulent fluxes had no

significant contribution to the higher spring temperature and increased summer and early fall's surface temperature because the drier soil surface in the assimilation run suppressed evaporation (Figure 4.4b). Moreover, the areally averaged moistures for 1 m soil from the model output did not exhibit a strong seasonal variation. Soil moisture from the assimilation run was much closer to that from the NCEP reanalysis data that was even drier than that of the assimilation run. This suggests that the soil moisture might be within a reasonable range after the application of remote-sensing data. As mentioned above, decreased cloud fraction resulted in stronger incoming solar radiation in the assimilation run. Since cloud fraction usually does not favor warm (less condensation) and dry atmospheric conditions, the exaggerated surface heating from the warmer surface and the diminished evaporation due to drier soil will lead to a warmer and drier atmospheric column, thereby resulting in smaller cloud fraction. Thus, in the assimilation run, the intensified surface heating with little change in evaporation produced a 2% decrease in the cloud fraction during the spring and the intensification of both resulted in a double decrease of the cloud fraction during summer and early fall. Examination of the circulation patterns indicates that the effects of advection on cloud fraction can be ignored.

As discussed in section 4.3, throughout the assimilation process, the amount of snowmelt was an input variable. If the model calculated snowmelt was larger than input snow melt, the extra energy flux artificially was assigned to soil. This is practical to some extent because it is impossible for snow to fully cover the soil surface in a GCM grid box (220 km × 220 km at 45°N). During the snow season, there is always some bare

soil surface exposed to the air except for the Polar Regions. The overestimation of snow depth in the control run led to an unrealistic distribution of heat fluxes for snow and bare soil surfaces and resulted in more energy being consumed by snow melt. Our method was to re-distribute the heat fluxes reaching the snow and soil surfaces. In terms of input snowmelt amount, certain heat fluxes were assigned to melt the corresponding amount of snow. The remaining heat fluxes were assigned to soil as part of ground heat flux. If the model-calculated energy for snowmelt was smaller than the input snow melt, the deficient energy was taken from the soil so that the energy balance was retained. However, there is no evidence showing that ground flux has a very significant contribution to snow melt. Fortunately, the frequency and magnitude of the latter case were quite low in our study. Figure 4.4c shows the difference in ground fluxes between two cases (assimilation run minus control run). The positive values result primarily from the extra snowmelt heat flux and mainly happened in spring and early summer when extensive snow melting was occurring. We found few negative values that suggest that the deficient heat flux for snowmelt was taken from soil (Figure 4.3c).

4.4.4 Precipitation

4.4.4.1 Variations of seasonal precipitation

Figure 4.6 shows the variations of seasonal precipitation from the control run, assimilation run, and Legates and Willmott (1990b) precipitation climatology. In the control run, the model overestimated precipitation during the entire year compared with observations. In August and September, the simulations were closer to the observations

than in the other times of the year. After application of the assimilation process in the model, precipitation decreased in summer and early fall and had little change in the rest of the year. In August, precipitation was even slightly lower than the observation. Trenberth (1999) pointed out that water recycling in the atmosphere was generally weak in cold seasons due to light surface evaporation and vigorous atmospheric circulation. It is strong in the warm seasons as a result of heavy surface evaporation and weak atmospheric circulation. Figure 4.4b shows a serious decrease in latent heat flux (evaporation) in summer and early fall that locally caused a drier atmosphere and less precipitation for the same period. During the rest of the year, local evaporation-induced precipitation did not change much.

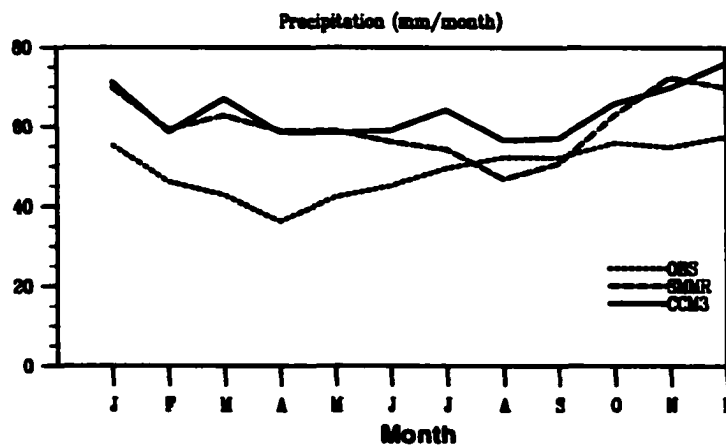


Figure 4.6 Comparison of monthly precipitation from CCM3 control (solid line) and assimilation (dashed line) runs and observations (dotted line).

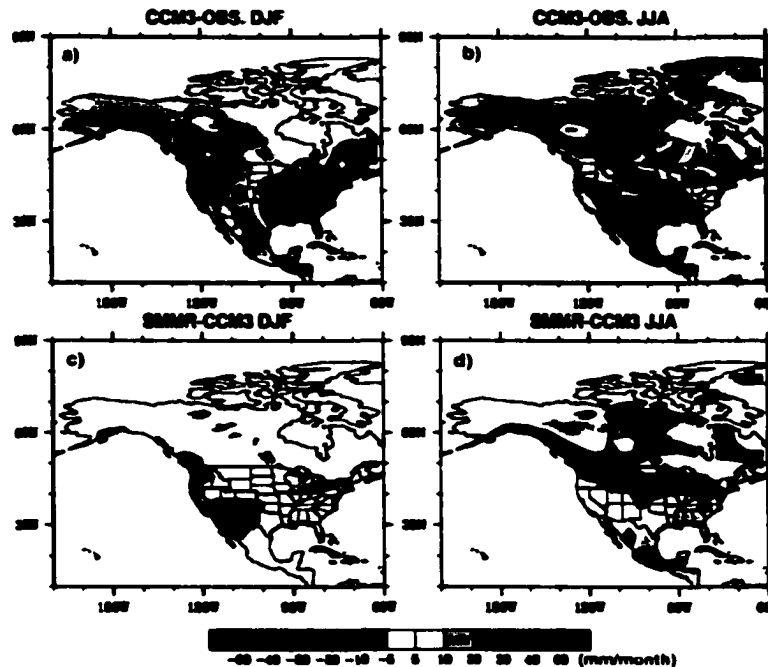


Figure 4.7 Geographic distributions of precipitation differences between CCM3 control run and observations in (a) winter and (b) summer and between CCM3 control and assimilation runs in (c) winter and (d) summer.

4.4.4.2 Geographic distribution of precipitation

Figures 4.7a and b are the two typical patterns of precipitation bias in the control run over North America compared with the Legates and Willmott (1990b) climatology during the year. Examination of these two patterns explains the anomalous snow depth during the snow season and the variations of summer precipitation after the application of the assimilation processes. Figure 4.7a is winter precipitation averaged over December, January, and February while Figure 4.7b is summer precipitation averaged over June, July, and August. In winter, precipitations over most regions of the Rocky

Mountains and northern Mexico were overestimated and underestimated over the eastern U.S. and southeastern Canada. In summer, except for some regions in southeastern Canada, precipitation over most Canada was overestimated and underestimated over the southern U.S and northern Mexico. Interestingly, the modeled precipitation over Missouri water basin had a very strong positive bias compared with observations.

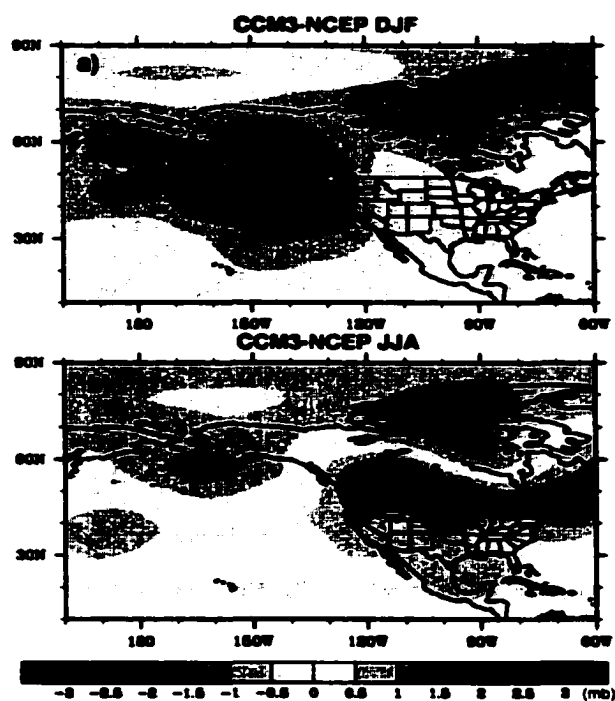


Figure 4.8 500 mb height differences between CCM3 output and NCEP reanalysis data averaged over (a) December, January, and (b) February and June, July, and August, respectively.

Figures 4.8a and b show that the 500 mb geopotential height field from the control run with the differences between the control run and the NCEP reanalysis data overlaid (control run minus NCEP reanalysis data). There is a strong positive bias center located over eastern Pacific, which intensified the westerlies on the west coast of North America

compared with the NCEP reanalysis data. Also, a negative bias center appeared at the north of Alaska, which intensified the northward pressure gradient and also resulted in stronger westerlies.. These two bias centers amplified the zonal wind on the west coast of North America, brought more air moisture from the Pacific to western North America, and led to stronger precipitation over the Rocky Mountains in winter, which is the vital reason for the anomalous snow depth. Figure 4.7a also indicates that eastern North America had stronger negative biases centered at the Great Lakes, which intensified the low pressure. Intensification of the low pressure brought drier and colder Arctic air down to the south on the west side and decreased precipitation in that region. The geographic distribution of surface air temperature (Figure not shown) indicated that the strong colder bias on the surface is the major reason for intensification of the low pressure over eastern North America in the control run.

In summer (Figure 4.8b), the western and middle Pacific had a strong positive bias for the 500 mb geopotential height compared with the NCEP reanalysis data. On the north side of the bias center, it increased the pressure gradient and strengthened the westerlies. Northern Alaska had a lessened center of geopotential height that also enhanced the westerlies on its south side. The combination of these two bias centers prolonged the intensified westerlies for northern North America and increased air moisture (Figure 4.8d). Thus, precipitation increased over northern North America compared with observations. On the south side of the bias center, the pressure gradient decreased and the westerlies were weakened. However, being far from the North American landmass, this variation did not exert much influence on precipitation. There was another strong

positive bias of geopotential height centered on the Great Lakes, which made the sub-tropical high move northward. Figure 4.8b shows that the entire southern U.S. was controlled by the sub-tropical high in the control run with drier and warmer air prevailing in this region and resulting in weaker precipitation. The geographic distribution of surface air temperature (Figure not shown) indicates that a strong warmer center underlying this positive bias is the key reason for the northward shift of the sub-tropical high. However, there are no strong atmospheric clues for the increase in precipitation over the Missouri water basin based on climate patterns. This phenomenon is discussed later with the assimilation process.

Figures 4.7c and d show the geographic distribution of the variation of precipitation between the assimilation run and control run (assimilation minus control). In winter, precipitation did not have any significant change after the assimilation except for a slight improvement over the southwestern U.S. The positive biases over the eastern Pacific (Figure 4.8a) slightly intensified because of the higher surface temperature in the assimilation case. This indicates that this bias was not relevant to the snow in the Rocky Mountains. In summer, the most significant improvement in modeling precipitation occurred between 40°N and 50°N and in southern Mexico. The decrease of precipitation is centered over the Missouri river basin and stretches northwest and east where the precipitation in the control run was overestimated. The overestimation of snow in winter and spring in the control run resulted in stronger evaporation and a colder climate in summer, which favors stronger precipitation. After the assimilation, thinner snow led to weaker evaporation and a warmer climate during the same period, which favors weaker

precipitation. Figure 4.7d also indicates that the drier and warmer air moved to the downstream region with the wind and lessened the precipitation there. Precipitation over southern Mexico greatly increased, where there was originally a negative bias in the control run. As mentioned above, the decrease in snow resulted in the warmer climate in summer over the Rocky Mountains and therefore a lower land surface pressure that favors the summer North American monsoon.

Snow, however, did not seriously affect summer precipitation outside the 40°N and 50°N region except for Mexico, although the greatest overestimation of snow occurred over the northern Rocky Mountains. Figure 4.9 shows the variations of winter and spring snow (averaged over January, February, and March) and summer downwelling solar radiation (averaged over June, July, and August) for the latitudes for the control run and the assimilation run over the Rocky Mountains. As expected, snow increased from low latitudes to high latitudes, but incoming solar radiation decreased in the same direction. The influence of snow variations on summer precipitation is closely related to the intensity of summer solar radiation (Figure 4.8). For example, at 62°N, snow depth from the control run was 20 cm higher than that from the assimilation run. The surface climate did not have very significant change in summer between the two runs because of the weak incoming solar radiation. Over the lower latitudes (below 40°N), although downward solar radiation was very strong, precipitation still did not change much because there was little difference in the snow depths between the two runs. However, summer surface precipitation changed seriously due to the strong incoming solar

radiation and the large variations in snow depths between the two runs over the middle latitudes (40°N and 50°N).

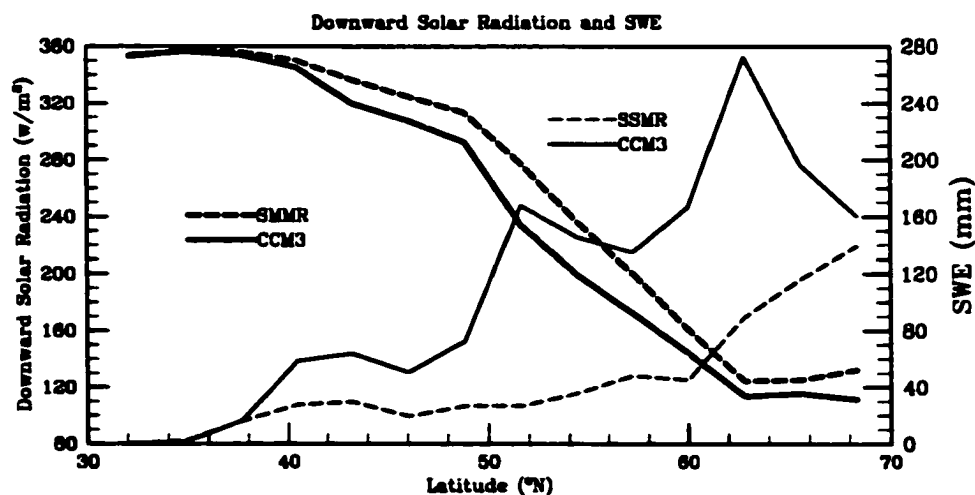


Figure 4.9 Downward solar radiation (thick lines) and SWE (thin lines) from CCM3 control (solid lines) and assimilation (dashed lines) runs.

4.5. Conclusions and discussions

An examination of the assimilation of remotely-sensed data with a GCM provide much new information, including consideration of energy and mass balances. Although this method is not completely accurate due to the coarse temporal resolution, a general trend between simulations and observations at a climate favored temporal scale (above monthly) were seen. The effects of snow on surface temperature and precipitation were isolated by using SMMR data and CCM3 output. The cold bias over the Rocky Mountains was improved by the decrease in surface albedo, snow melt, and surface

evaporation after the assimilation processes. The effects of surface albedo and snow mass were seen mainly during winter and spring and surface evaporation reached its maximum influence after the snow duration. Since most of the Rocky Mountains are covered by evergreen needle leaf forests, with a maximum fraction of 80% in summer and a minimum fraction of 70% in winter in the model, the modification of surface albedo caused by the change of snow was only a 3% decrease because the snow is concealed under such a large degree. Viterbo and Betts (1999) also indicated that the surface albedo was very close to that of vegetation over the forest regions even when an abundance of snow existed. For example, in April the increase in the absorption of solar radiation caused by surface albedo was 6 W/m^2 , but the increase in ground flux to the soil was 10 W/m^2 from the redistribution of snowmelt energy in the assimilation run. Hence, the redistribution of snowmelt energy played a vital role in the improvement of cold biases for spring. Without the presence of snow in summer, soil moisture induced reduction of evaporation was the crucial factor affecting surface temperature. Furthermore, the variations of evaporation led to changes of cloud fractions and thus to changes of incoming solar radiation, another significant factor affecting the simulation of surface air temperature in summer. It can be clearly seen that the incorporation of SMMR snow data with the GCM also caused the redistribution of the components in the energy balance and a new balance was reached at a higher temperature level.

Precipitation in the region has a strong seasonality; most areas of the Rocky Mountains have a winter maximum and a summer minimum. Snow is the major source for soil water recharge because 50% - 70% of the annual precipitation falls as snow

(Serreze et al. 1999). The variability of snow amount affects summer soil moisture, evaporation, and summer precipitation, to some extent, because of the strong atmospheric recycling (Trenberth 1999). The snow effects on summer precipitation occur not only locally but in the downstream regions as well. An overestimation of snow results in a wet and cold climate that favors precipitation. The most significant effects of snow on summer precipitation occur between 40°N and 50°N. The atmospheric responses to modification in land surface are closely related to the intensity of incoming solar radiation. The strong atmospheric responses come from significant changes of land surface with the strong incoming solar radiation. These two conditions were just satisfied in the region between 40°N and 50°N where a significant change in precipitation occurred. Snow has little influence on winter precipitation due primarily to light evaporation and vigorous atmospheric circulation.

5. CORRELATION BETWEEN SNOWPACK IN THE WESTERN U.S. AND TROPICAL PACIFIC SST

5.1. Introduction

The importance of snow over the western U.S. to climate variation and water resources has been addressed by many researchers (McCabe and Legates 1995; Serreze et al. 1999; Clark et al. 2001). Serreze et al. (1999) found that 50% - 70% of the annual precipitation falls as snow in the mountainous region of the western U.S. 75% - 85% of annual discharge in the region is derived from the snowpack (Grant and Kahan 1974; Palmer 1988). An accurate forecast of snow mass is essential to managing the water supply in the region.

Snow variability is strongly related to variations in climate. McCabe and Legates (1995) indicate that temporal and spatial distributions of the April 1 snowpack over the western U.S. have strong correlations with the 700 mb height circulation patterns. They claim that an above than normal April 1 snowpack occurred in the western U.S. when negative 700 mb anomalies appeared in the North Pacific south of the Aleutian Islands; conversely, a below than normal snowpack was associated with positive 700 mb height anomalies in the western U.S. Cayan (1996) studied the same issue by using a principal component analysis (PCA). He found that the loadings of the first five components of PCA could represent five different snow regions in the western U.S. Snow variations in these five regions resulted from anomalous precipitation, which was associated with the different climate circulation patterns, and temperature had a secondary effect on

snowpack. Cayan and Roads (1984) also found that the precipitation variability over the western U.S. is strongly correlated with sea level pressure. Changnon et al. (1993) indicate that the frequency of seven 500 mb winter synoptic patterns could interpret 90% of the annual snowpack anomalies.

In general, snowpack variability in the western U.S., largely caused by anomalous precipitation, is closely associated with variations in climate patterns. Climate change is closely associated with the variability of SST, especially in the tropical Pacific region. Lau and Nath (1994) performed GCM experiments to investigate the effects of tropical Pacific SST variation on midlatitude atmospheric circulation, which have a strong influence on surface hydro-climatological changes in the western U.S. They found that the model could reproduce the Pacific-North-America (PNA) circulation patterns (Barnston and Liveszey 1987; Wallace et al. 1990) only when forced by the strong tropical Pacific SST anomalies during the ENSO epoch. The extratropical SST anomalies had minor effects on the midlatitude atmospheric circulation patterns (Lau and Nath 1994, 1996, and 2001). Some observational (Horel and Wallace 1981; among others) and modeling (Sardeshmukh and Hoskins 1988; among others) studies also found a strong relationship between tropical Pacific SST anomalies and midlatitude atmospheric variations. Clark et al. (2001) investigated the historic effects of El Niño and La Niña events on seasonal snowpack evolution in the Columbia and Colorado River basins. They found that the ENSO exerted influences on the snowpack in both basins through midlatitude circulation anomalies.

Generally, connections between tropical Pacific SST anomalies and snowpack variations in the western U.S. are fulfilled by the anomalies of the midlatitude atmospheric circulation. However, these studies do not illustrate the overall connection between ENSO-related SST anomalies and variations in the midlatitude atmospheric circulation, which strongly affects snowpack changes in the western U.S. The effects of interannual variations of the tropical Pacific SST anomalies on variations of atmospheric circulation patterns have not been investigated thoroughly. For example, the positions and intensities of atmospheric patterns in midlatitudes produced by strong El Niño events might be different from those generated by weak El Niño events. Variations of atmospheric patterns strongly affect snow amount and its geographic distributions in the western U.S.

CCM3 is used to simulate the relationship between ENSO-related SST anomalies and variations in snow amount and distribution in the western U.S. NCEP reanalysis data and observations from the Climate Research Unit (CRU), University of Anglia, United Kingdom, are applied to validate model output. Our results show that variations in the observed and simulated SWEs over the northwest and the southwestern U.S. have different relationships with tropical Pacific SST anomalies. The same conclusion was also drawn by Cayan (1996), McCabe and Dettinger (2001), Clark et al. (2001), and others. Both observed and simulated SWEs are classified into four types in the western U.S., which are the above and below normal SWEs over the northwestern U.S. (NWA and NWB, respectively) and above and below normal SWEs over the southwestern U.S. (SWA and SWB, respectively). Based on this classification, we found that the strong and

weak ENSO-related SST anomalies correspond to different anomalous SWEs in the western U.S.

Descriptions of the model and data for both observations and simulations are presented in sections 5.2 and 5.3. The detailed analyses of model output and observations are in section 5.4 and discussions and conclusions are in section 5.5.

5.2 Model

The GCM used in this study is NCAR's CCM3 (Kiehl et al. 1996) with 18 vertical atmospheric levels extending from the surface boundary layer to the 2.9 mb level, and a horizontal grid of approximately $2.8^\circ \times 2.8^\circ$. This model is driven by the prescribed monthly global SSTs from December, 1945 to May, 1995, which have the same resolution as the model.

The original land surface model (Bonan 1996) in CCM3 has been replaced by SAST model (Sun et al. 1999; Jin et al. 1999b) in which the sophisticated physical processes of snow and soil are addressed. The SAST model, as discussed before, has three snow layers used for simulation complied with the energy and mass balances. Within the snowpack, liquid water is treated as the concept of liquid water holding capacity parameterized as a function of snow density, and water vapor is ignored. The grain size of snow used for calculating liquid water transfer is also treated as a function of snow density. The less than 5 mm snow depth is lumped with soil. In addition, the soil is divided into 10 layers in which temperature and moisture is also solved in terms of the energy and mass balance equations. Frozen soil is introduced through modifying the

thermal conductivity and heat capacity of soil when the temperature is below the freezing point. The vegetation mode is taken from BATS version 1e (Dickinson et al. 1993).

Vegetation, soil, and snow are mixed in a grid square with a size of 2.8° by 2.8° . The methodology of fraction calculations is adopted from BATS. Maximum and minimum vegetation fractions are prescribed and the variations between them are a function of the soil temperature at 1 meter deep. Snow fraction is a function of the roughnesses of vegetation and soil and the bare soil fraction is the part excluding snow and vegetation in the grid box.

5.3. Data

The 2.8° by 2.8° global model outputs were generated by a model integration from December 1949 to May 1995, which was driven by the prescribed global SST data during the same period. This SST dataset is almost identical to the NCEP reanalysis data (Figure not shown). Data for the 500mb geopotential height and wind fields are also NCEP/NCAR reanalysis data, which are treated as observations in the paper. These data have a 2.5° by 2.5° horizontal resolution and the same time length with that of the model outputs.

The observed SWE depths for the first days of January, February, March, and April in the western U.S. are obtained from Clark et al. (2001) and more than 300 snowcourse locations are selected in the region. The observed precipitation (Hulme et al. 1998) and the surface air temperature (Jones 1994), in a gridded format of 5° by 5° horizontal resolution, are from CRU, University of East Anglia, United Kingdom.

In this chapter, November, December, January, and February (NDJF) represent the winter snow accumulation stage. Although the observed SWEs usually reach their peaks on April 1 (McCabe 1996; Serreze et al. 1999; Borhr and Aguado 2001; Clark et al. 2001) in the western U.S., the simulated SWEs in CCM3 start to decrease over the southwestern U.S. in March because of the warm biases of the model. Thus, the data for March (April 1 data for the observed SWEs) are not included in our study. All data, except for precipitation and observed SWE, are averaged over NDJF. Precipitation for observations and simulations are the total of these months. The observed SWE on January 1, February 1, and March 1 are averaged to approximately represent winter snow in the accumulation stage.

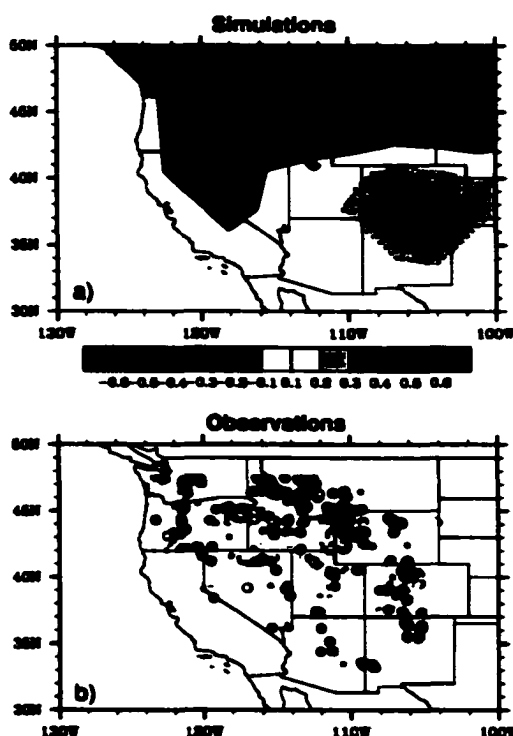


Figure 5.1 Correlation coefficients between Niño-3.4 SST and (a) SWEs from CCM3 output and (b) observed snowcourse data in western U.S. Values in stippled areas pass the 95% significance Student's *t* test.

5.4. Results

5.4.1. Relationship between snow depth in the western U.S. and tropical Pacific SST

As mentioned above, Cayan (1996), Clark et al. (2001), and McCabe and Dettinger (2001) pointed out that the snowpack in the northwestern and southwestern U.S. exhibits different characteristics during El Niño and La Niña episodes. Figure 5.1 illustrates the correlations between Niño-3.4 SSTs (the average of SSTs over 120°W-170°W and 5°S-

5°N in the tropical Pacific region) (Trenberth 1997), and snowpack from model output and observations. The results indicate that the simulated SWE (Figure 1a) was negatively correlated with the Nino-3.4 SSTs in the northwestern U.S. The negative contours are centered over the ridges of mountains on the border between Idaho and Montana. The dotted area shows that the correlation coefficients passed the 95% significance level based on the Student's *t* test. A relatively weak positive correlation coefficient center is over the border between Colorado and New Mexico, where mountains are the typical landscape. The correlation coefficients in this region also significantly passed the 95% *t* test. The observations based on snow course data (Figure 5.1b) demonstrate the consistent pattern with simulations, which indicate that the northwestern U.S. had strong negative correlation coefficients and most stations in the southwestern U.S. had positive ones. The correlations in Colorado varied from negative to positive values southwardly, which is also illustrated in Clark et al. 2001. However, the model did not have an accurate simulation over this transition area. Generally, the basic patterns for simulations and observations were consistent. At the same time, the positive correlation coefficients are relatively weak compared with the negative values over the northwestern U.S. This will be explained later.

5.4.2 SST anomaly patterns corresponding to the SWE anomalies in the western U.S.

As discussed above, the variations of tropical Pacific SSTs have a relationship with the anomalous SWE in the western U.S. The simulated and observed SWEs in the northwestern and southwestern U.S. shows different characteristics in Figure 5.1. To

show the SST anomaly patterns which are connected with the anomalous SWEs in the western U.S., simulated and the observed SWE anomalies were averaged as a 45-year time series over the northwestern U.S. (defined as 44°N-50°N and 102°W-122°W), and over the southwestern U.S. (defined as 33°N-39°N and 102°W-110°W), respectively, based on correlation patterns (Figure 5.1). With these time averages, we can define above and below normal SWEs in the northwestern U.S. (NWA and NWB) and the southwestern U.S. (SWA and SWB). If SWEs from both observations and simulations in the northwestern U.S. had above or below normal SWEs and passed the 95% significance Student's *t* test, the corresponding years were defined as NWA or NWB years. The same method was employed to define SWA and SWB years in the southwestern U.S. The sample numbers for these four cases are sufficient for statistical purposes (Table 5.1).

Table 5.1 Sample numbers for NWA, NWB, SWA, and SWB.

	NWA	NWB	SWA	SWB
Sample numbers	11	15	12	15

Using these four cases, the global SST anomalies during the snow accumulation period (NDJF) in the western U.S. were averaged over the corresponding years and defined the NWA, NWB, SWA, and SWB SST anomaly patterns (Figure 5.2a-d).

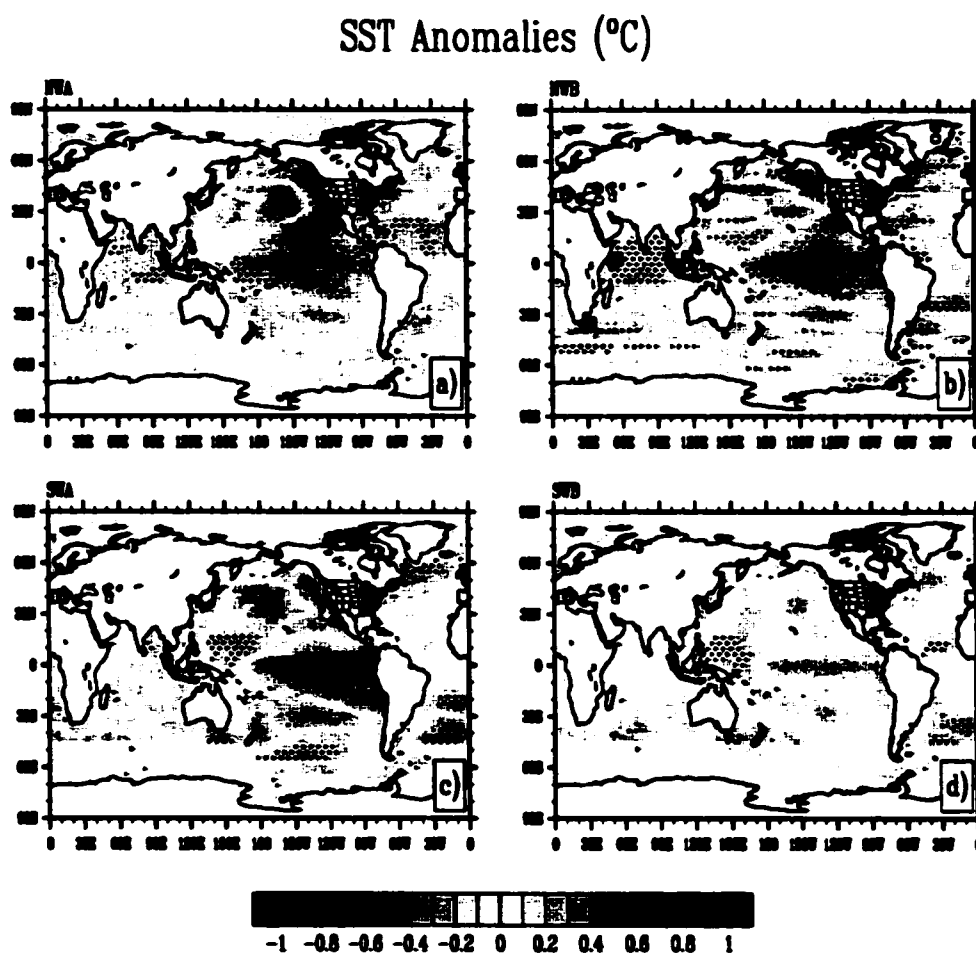


Figure 5.2 SST anomalies during the years of (a) NWA, (b) NWB, (c) SWA, and (d) SWB. Stippled areas pass the 90% significance Student's t test.

For NWA, the anomalous pattern of SST strongly resemble the typical La Niña pattern (Trenberth 1997). The SST anomalies in the most regions over the central and eastern North Pacific passed the 90% significance Student's *t* test. However, variations in the tropical winter SSTs were relatively weak and the averaged SST anomaly for the Niño-3.4 region was -0.38 °C (Table 5.2). For NWB, the pattern of anomalous SST anomalies mimicked the typical El Niño pattern. The averaged winter SST anomaly over the Niño 3.4 region was 0.45 °C. Variations of SST anomalies over the central and eastern North Pacific also significantly passed the 90% Student's *t* test.

Table 5.2 Anomalies of Niño 3.4 SST.

	NWA	NWB	SWA	SWB
SSTA (°C)	-0.38	0.45	0.61	-0.22

Variations of tropical SST anomalies for SWA were very strong and the Niño-3.4 SST anomaly was 0.61 °C, but variations of SST anomalies over the North Pacific were relatively weak. Snow did not show the expected relationship with SST anomalies for SWB because SST anomalies in the Pacific did not pass the 90% Student's *t* test. Thus, the above normal SWEs over the southwestern U.S. are strongly related to the anomalies of tropical SSTs. However, the below normal SWEs over the southwestern U.S. are not related to SST anomalies, which is why the SWEs over the southwestern U.S. had relatively weak correlations with Niño-3.4 SSTA when compared with the SWEs over northwestern U.S.

5.4.3 500 mb geopotential height anomalies during the years of anomalous snow in the western U.S.

The 500 mb geopotential height plays an important role in weather and climate forecasts and studies. Usually, indications for variations of surface variables can be found from 500 mb height field. Thus, the averaged anomalous 500mb heights for these four cases were constructed analogous to the SST anomaly patterns presented above.

Simulated 500mb Height Anomalies (mb)

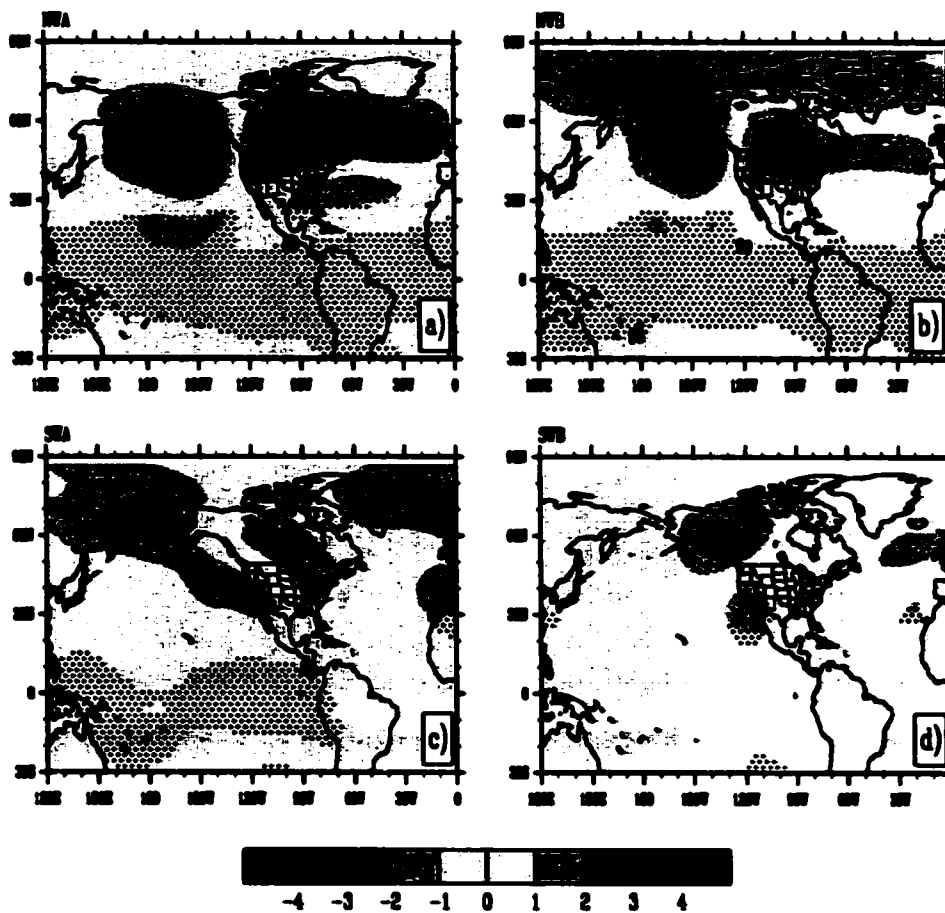


Figure 5.3 Simulated 500 mb height anomalies during the years of (a) NWA, (b) NWB, (c) SWA, and (d) SWB. Stippled areas pass the 90% significance Student's *t* test.

Observed 500mb Height Anomalies (mb)

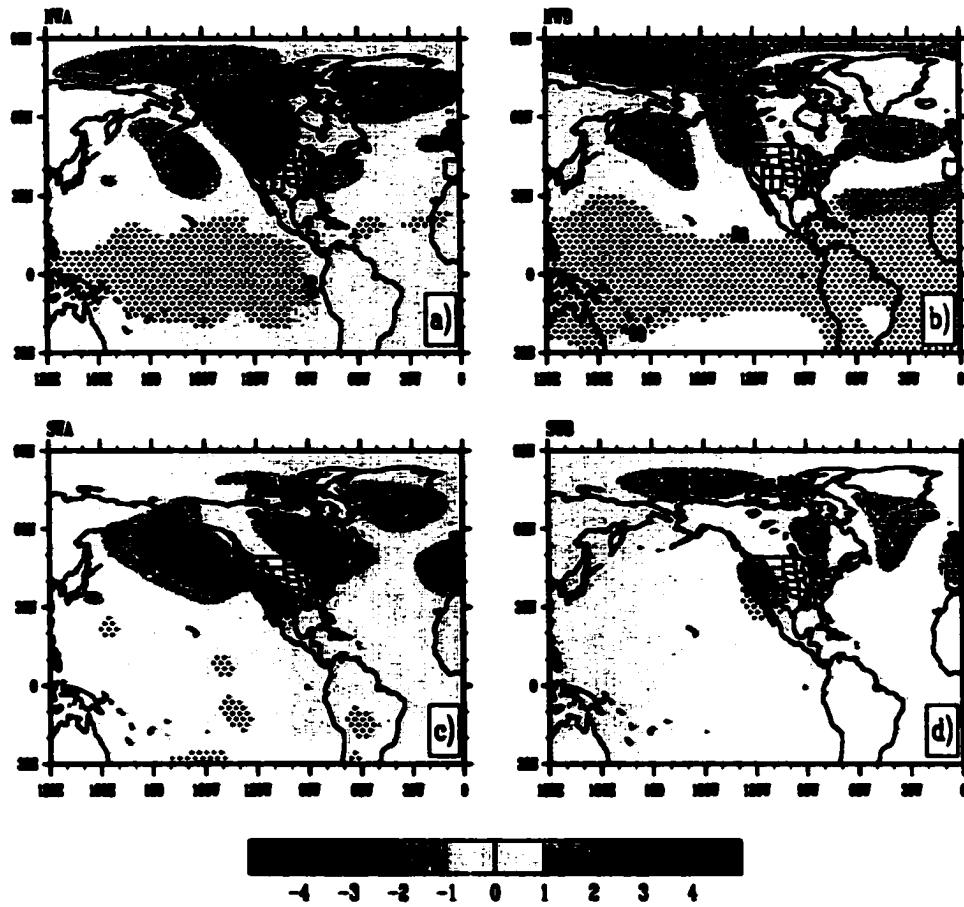


Figure 5.4 Observed 500 mb height anomalies during the years of (a) NWA, (b) NWB, (c) SWA, and (d) SWB. Stippled areas pass the 90% significance Student's *t* test.

5.4.3.1 NWA and NWB

For NWA, the anomalous atmospheric height patterns (Figures 5.3a and 4a) for simulations and observations produced by the corresponding SSTA pattern (Figure 5.2a) are very similar in many respects. For example, a positive 500 mb height anomaly center appeared in the central North Pacific south of the Aleutians, which weakens the Aleutian Low, while there is a negative center over northern North America for both simulations and observations. The observed anomaly centers in the midlatitudes had northwest-to-southeast orientations (Figure 5.4a) while the simulations exhibited zonal structures (Figure 5.3a). Specifically, the simulated negative center over northern North America extended zonally to the east and formed another sub-center over the northern Atlantic, which did not significantly show on the observed map. The intensity of both positive and negative centers for simulations were much stronger than those for observations. Over the tropical Pacific region there were very weak negative anomalies which still passed the 90% significance level t test for both simulations and observations. These negative anomalies are due to the contraction of the atmospheric column resulting from colder SSTs, which were consistent between simulations and observations.

Anomalous 500 mb heights for simulations and observations for NWB are just opposite to those for NWA. There is a negative anomaly center south of the Aleutian Islands, which appeared to deepen the Aleutian Low, while a positive anomaly center is located in northern North America (Figures 5.3b and 5.4b). The observed negative anomaly center was fairly weak in magnitude compared with the simulated one and the observed positive anomalies were centered on the west coast of Canada while the

simulated ones were displaced to the middle of the U.S.-Canadian border and had a stronger intensity. The tropical Pacific region had positive 500 mb height anomalies for simulations and observations due to expansion of the atmospheric column caused by warmer SSTs

5.4.3.2 SWA and SWB

When snow was above normal (SWA) in the southwestern U.S., corresponding 500 mb height anomalous patterns for simulations and observations (Figures 5.3c and 5.4c) were generated by the strong warmer tropical Pacific SSTs. In the observed map (Figure 5.4c), a negative 500 mb height anomaly center is located in the North Pacific south of the Aleutian Islands, extending to the southwestern U.S. and having a strong dipolar structure. In the simulated map, the anomaly center is displaced to the northeast coast of Russia west of the Bering Strait, also extending to the southwestern U.S. (Figure 5.3c), but over the ocean, the anomaly is quite weak and does not pass the 90% significance level t test. However, both the simulated and observed negative anomaly centers on land in the southwestern U.S. significantly passed the 90% t test. In the observed map (Figure 5.4c), there is a positive anomaly center in western Canada with a strong northwest-to-southeast orientation, while the simulated positive anomaly center located in the same place (Figure 5.3c) is much weaker and even does not pass the 90% t test. Disturbances due to the warmer SSTs in the tropical Pacific for simulations are significant, and are much weaker in the observed 500 mb height map.

As mentioned above, there is no evident connection between the anomalous SSTs and below normal SWEs in the southwestern U.S. There were positive anomaly centers in the region for both simulations and observations, which passed the 90% t test and a simulated negative anomaly center was located on the west coast of Canada, which did not appear in the observations. Explanations for the 500 mb height anomalies during the years of SWB are given later.

5.4.4 500 mb wind field anomalies during the periods of anomalous snow in the western U.S.

Although wind field is largely determined by geopotential height, it can give a better understanding of air mass and moisture transport than the height field and how atmospheric circulation patterns affect variations in surface climate such as precipitation and temperature.

5.4.4.1 NWA and NWB

A transition region between the positive anomaly center in the North Pacific and the negative one in North America in the simulated map (Figure 5.3a) for NWA is located over the northwestern U.S. Large height gradients, which are the reason for the strong anomalous wind, are formed in this transition region. For NWA, the zonally oriented structure of the simulated 500 mb height anomalies in the midlatitudes resulted in strong northerlies in the northwestern U.S. (Figure 5.5a), which controlled most parts of the region and brought the cold and dry air there. The wind anomalies gradually

became easterlies on the east of Idaho. This hinders moist air from entering the northwestern U.S. from the Pacific. The observed negative anomaly center over North America was displaced to the west coast of Canada, encouraging easterlies with moist air to enter the northwestern U.S. from the south. The northwest-to-southeast orientation of the positive anomaly center located in the North Pacific strengthened the eastward wind component from the ocean and weakened the southward wind component from Canada. Figure 5.6a shows that a significant amount of observed moist air entered the northwestern U.S. from the Pacific compared with the simulations (Figure 5.4a) where the northerlies mainly prevailed in the region.

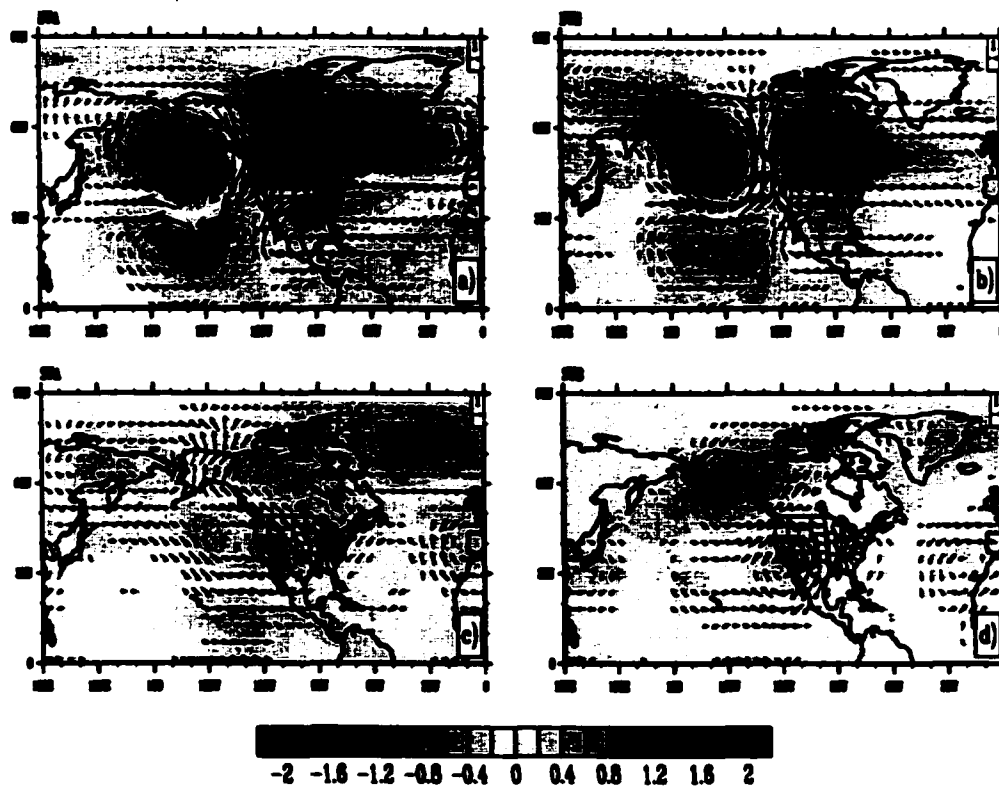
Simulated 500mb Wind and Temperature Anomalies ($^{\circ}\text{C}$)

Figure 5.5 Simulated 500 mb wind and temperature anomalies during the years of (a) NWA, (b) NWB, (c) SWA, and (d) SWB. Stippled areas pass the 90% significance Student's *t* test.

Observed 500mb Wind and Temperature Anomalies ($^{\circ}\text{C}$)

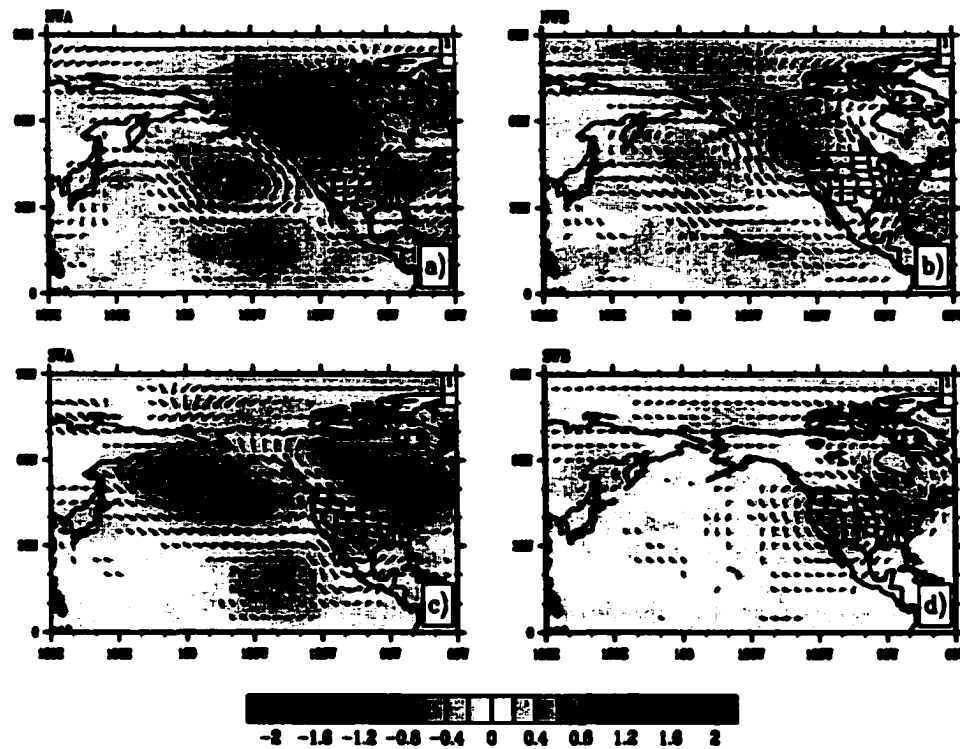


Figure 5.6 Observed 500 mb wind and temperature anomalies during the years of (a) NWA, (b) NWB, (c) SWA, and (d) SWB. Stippled areas pass the 90% significance Student's t test.

The anomalous 500 mb height patterns for NWB are just opposite to NWA. These opposite patterns bring strong southerlies and southeasterlies to the northwestern U.S. (Figure 5.5b) in simulations because of its zonally oriented structure. For observations, the positive anomalies located on the west coast of Canada lead to prevailing easterlies and northeasterlies at the U.S. border.

5.4.4.2 SWA and SWB

The dipolar negative anomaly center generated by the strong tropical Pacific SST anomalies has a northwest-to-southeast structure and protrudes into the southwestern U.S. during the SWA (Figure 5.3c). This center introduces moist southeasterlies from the Gulf of Mexico to the southwestern U.S. (Figure 5.5c) in both simulations and observations. A positive 500 mb height anomaly center for SWB is found in the southwestern U.S. in both simulations and observations, but has no connection with SST anomalies as mentioned above. This anomalous circulation pattern, which usually bring dry air from the north and encourages downward air motion, does not favor precipitation. A negative anomaly center is simulated on the west coast of Canada, but is not observed. The negative center intensifies the magnitude of the wind entering the northwestern U.S. and southwestern Canada and have little effect on precipitation and temperature in the southwestern U.S. The reasons for the formation of the anomalous circulation pattern in Figures 5.5d and 5.6d are discussed later.

5.4.5 Precipitation and temperature

As we know, variations of precipitation and temperature determine anomalies of SWE during the winter season. Thus, the analyses of precipitation and temperature anomaly patterns in the western U.S. can provide us with clues for the variations of SWE.

Simulated Precipitation Anomalies (mm/month)

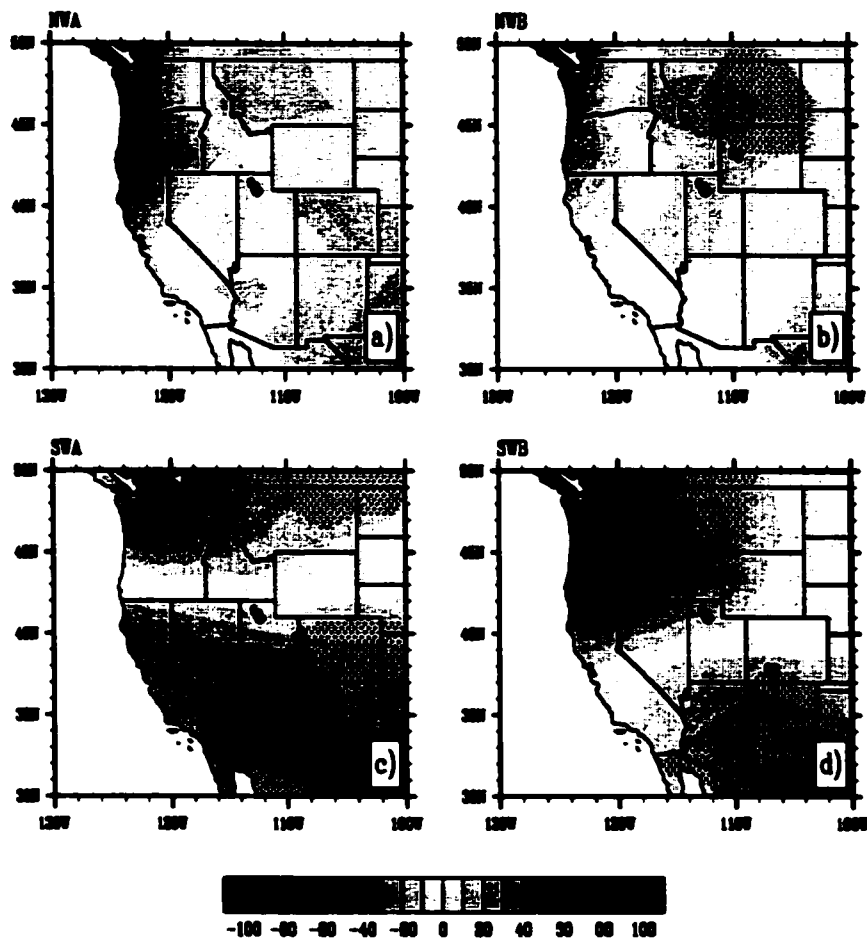


Figure 5.7 Simulated precipitation anomalies during the years of (a) NWA, (b) NWB, (c) SWA, and (d) SWB. Stippled areas pass the 90% significance Student's *t* test.

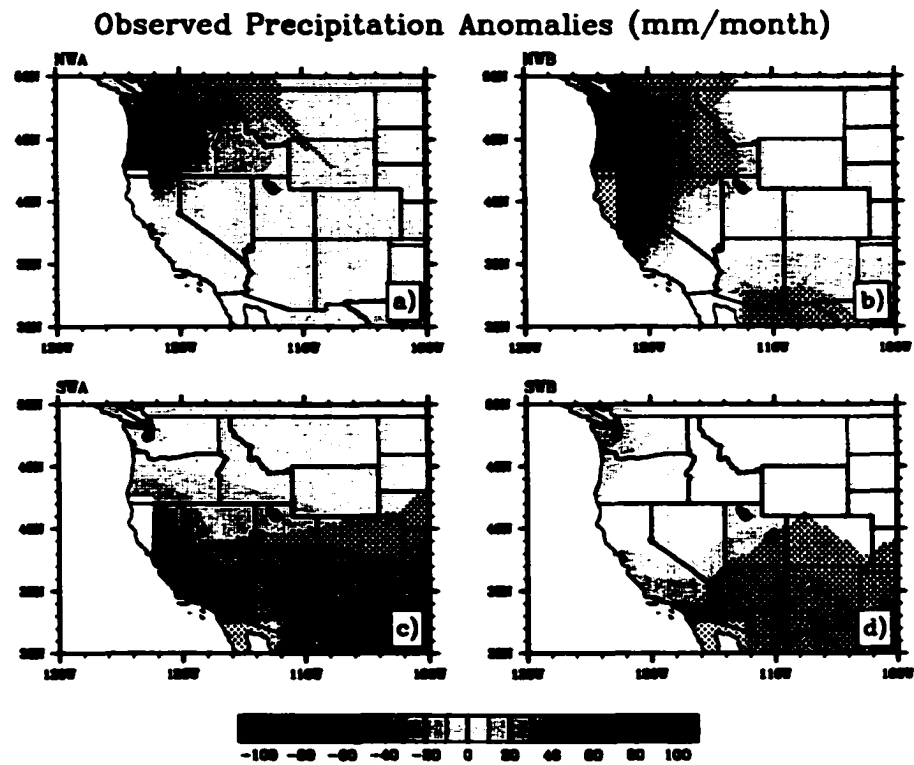


Figure 5.8 Observed precipitation anomalies during the years of (a) NWA, (b) NWB, (c) SWA, and (d) SWB. Stippled areas pass the 90% significance Student's *t* test.

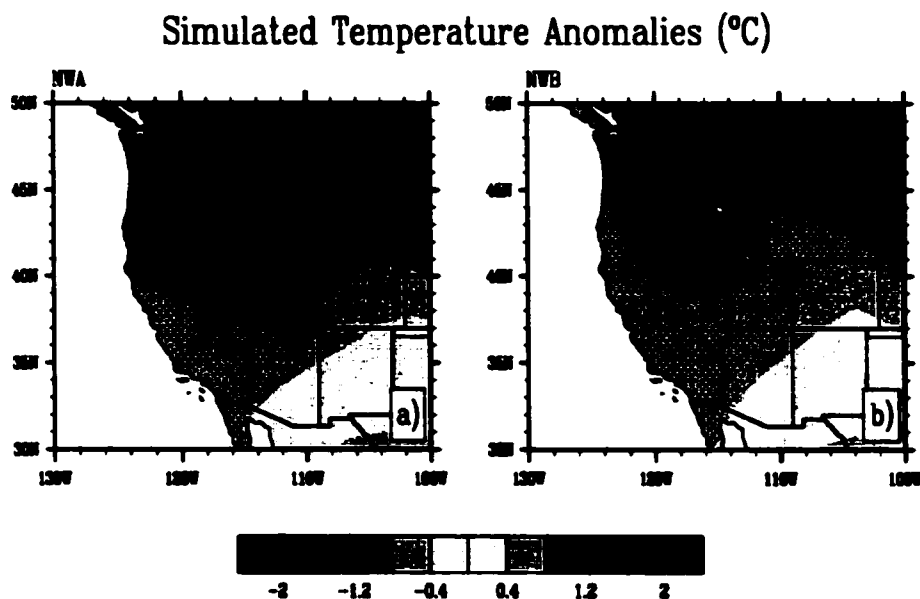


Figure 5.9 Simulated temperature anomalies during the years of (a) NWA and (b) NWB. Stippled areas pass the 90% significant Student's t test.

5.4.5.1 NWA and NWB

Figure 5.7a shows the simulated precipitation anomaly pattern during the period of the snow above normal (NWA), which shows that there were no significant variations of precipitation in the northwestern U.S. except for the west coast area where negative anomalies occurred significantly, as a result of the strong dry northerlies (Figures 5.3a and 5.5a). Although the westrelies created a light positive precipitation anomaly center in Montana, it did not pass the 90% t test (Figure 5.5a). Therefore, the anomalies of precipitation had little contribution to the positive SWE anomalies, and even tended to slightly reduce them in western Idaho. Significant positive precipitation anomalies were

observed in most areas of the northwestern U.S., which led to thicker than average SWEs. The heavier precipitation was mainly caused by the transportation of moist air with the intensified westerlies from the North Pacific (Figure 5.6a). A trough formed in the northwestern U.S. resulted in the convergence of air mass and upward motions and heavier precipitation occurred in the region. Although both observations and simulations have positive SWE anomalies in the same years, the simulated precipitation had a strong bias caused by the displacement of simulated height and wind field patterns. A possible factor affecting the simulated SWE anomalies in the model is temperature. Figure 5.9a shows that the negative surface air temperature anomalies for simulations appeared in the northwestern U.S. during the NWA for two reasons. First, the strong northerlies brought cold air to the region and led to a decrease in temperature. Second, a bias in the simulated circulation patterns (Figures 5.3a and 5.5a) reduced the warm moist air mass entering the northwestern U.S. which also resulted in colder temperatures. The cold bias led to less snow melt and therefore, thicker than normal snow.

Positive precipitation anomalies for simulation NWB appear in the northwest corner of the U.S., caused by warm and moist airflow from the Pacific. Although a negative anomaly center in Montana (Figure 5.5a), caused by the dry southerlies and southeasterlies inland U.S. is fairly weak, most of it passed the 90% significance t test. The negative precipitation anomalies contribute to thinner than normal snow in the region during winter to some extent. Strong positive temperature anomalies caused by the warm southerlies and southeasterlies primarily from the continental U.S. (Figure 5.5b), controlled the entire the northwestern U.S. (Figure 5.9b). The warmer climate in the

region strengthened snowmelt and led to the negative SWE anomalies, which are the main reason for the thinner snow in the northwestern U.S. Dry northerlies and northeasterlies are observed in the northwestern U.S. and decrease precipitation in the region, leading to thinner than normal snow. Based on this analysis, snow anomalies in the northwestern U.S. during the winter are consistent between simulations and observations, but for very different reasons. For observations, the variations of precipitation are the major contributor to snow anomalies; however, temperature fluctuations largely determine the variations of the simulated SWEs, which result from the drifted climate patterns in the model.

5.4.5.2 SWA and SWB

Figure 5.7c shows the anomalous precipitation pattern for simulations when the SWEs were above normal in the southwestern U.S. The positive precipitation anomalies appear in most part of the southwestern U.S., resulting in thicker than average simulated SWEs in the area. Responding to the strong warmer tropical Pacific SSTs, a negative anomaly center extends to the southwestern U.S. (Figure 5.3c), which introduces moist air mass from the Mexican Gulf (Figure 5.5c) and increases precipitation in the region. The negative 500 mb height anomaly pattern usually encourages upward motion, which intensify the positive precipitation anomalies. The trend of observed precipitation in the southwestern U.S. (Figure 5.8c) is consistent with that simulated and its water source is also from the Mexican Gulf .

For SWB, the positive anomaly center in the southwestern U.S. brought dry northwesterlies to the region and decreased precipitation in both simulations and observations. This center also favors downward air motion that weakens precipitation. A strong positive precipitation anomaly center is simulated in the northwestern U.S., but is particularly weak in the observations. The simulated transportation of moist air from the Pacific to the northwestern U.S. were intensified by a negative anomaly center located on the west coast of Canada, which does not appeared in the observations.

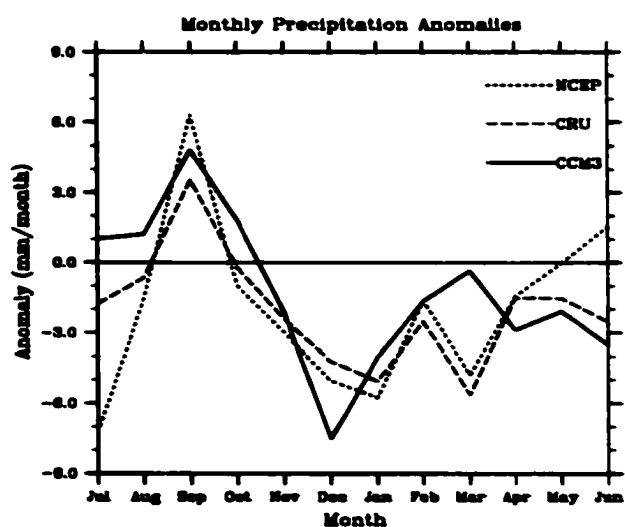


Figure 5.10 Comparison of precipitation anomalies from CCM3 output, observations from Climate Research Unit (CRU), United Kingdom, and NCEP reanalysis data.

As mentioned above, thinner than average SWEs in the southwestern U.S. are not correlated with SST variations. The winter 500 mb height anomaly pattern indeed contained significant anomalies over the southwestern U.S. Thus, fluctuations of 500 mb

height field most possibly are aroused by local climate variability. In order to explore the mechanism of these anomalies, the time series of anomalous precipitation from CRU, NCEP reanalysis, and model output data are compared in Figure 5.10. These precipitations were areally averaged over the southwestern U.S. from July to June of the next year if the SWE over the southwestern U.S. averaged over NDJF was below normal. When compared, the three datasets matched each other, implying that the model output and reanalysis data are reliable. Precipitation from all three datasets were less than average from November to February, consistent with the thinner than normal SWE in the same period, but above normal peak values occurred in September for all three datasets. This anomalous precipitation can explain the formation of the positive height anomaly center over the southwestern U.S., which had no connection with the SST variations. In the fall, the positive anomalous precipitation releases extra latent heat fluxes that heat up the atmosphere from the low level where the major part of air moisture exists. The heating process resulted in the expanding of the atmosphere column and led to positive anomalous 500 mb geopotential height, which continued through the winter without external forces to change them (SSTs were under their average conditions). Then, eastern parts of the positive height anomaly centers in both observations and simulations introduced dry northwestlies to the southwestern U.S. and reduced the precipitation, leading to thinner SWE in the region. These positive anomaly centers also favored the downward air motions, lowering precipitation. The thinner SWE decreased surface albedo and increased solar radiation absorption, thereby exaggerating the surface

temperature. The warmer surface intensified the positive height anomalies, which was a positive feedback for the interaction between land surface and atmosphere.

5.5 Discussions and conclusions

Lau and Nath (1994) used the observed SST field, which had monthly varying conditions in the tropical Pacific region ($25^{\circ}\text{S} - 25^{\circ}\text{N}$) and a climatological annual cycle without year-to-year variability outside of this region, to drive their GCM. They found that the model generated wave-like 515 mb height anomalous patterns in the midlatitudes when compared with observations, which were not reproduced when they used monthly varying SST conditions in the North Pacific, $25^{\circ}\text{N} - 55^{\circ}\text{N}$, and SST climatology in the other regions. Their results strongly suggest that the tropical Pacific is a thermal source for the anomalous atmospheric patterns in the North Pacific/North America sector while the North Pacific plays a secondary role in this respect. The theoretical study performed by Hoskins and Karoly (1981) also has the same conclusions, which indicate that a low-latitude thermal source produces long wavelengths propagating strongly polewards as well as eastwards. The relationship between SWE anomalies in the western U.S. affected by the midlatitude atmospheric patterns and the tropical SST anomalies showed by this paper (Figure 5.1) and many others also verify the above conclusions (Lau and Nath 1994; Hoskins and Karoly 1981). Although the basic atmospheric anomaly patterns in the North Pacific/North America sector from simulations were in a good agreement with the observations, the accuracy of their intensities and locations still had some distance from the observed results, which are crucial to climate simulations in a small area like the

western U.S. For example, in our observed results, the midlatitude atmosphere had a strong response to a strong El Niño episode (Figure 5.4c) while the response was relatively weak as a weak El Niño was happening, which CCM3 did not simulate well, possibly because of unrealistic heat flux exchanges between sea surface and atmosphere boundaries in CCM3 (figure not shown). This issue is not in the scope of this study.

Based on the above analyses, we can conclude our results as follows. In the northwestern U.S., the above normal SWE is a response to the weak La Niña event while the below normal SWE is the result of a weak El Niño event. In the southwestern U.S., the above normal SWE corresponds to a strong El Niño event and the below normal SWE, which is caused by local climate variability, had no connections with SST anomalies. Therefore, the SWEs in the southwestern U.S. have relatively weaker correlations with the Niño-3.4 SST than they do in the northwestern U.S. Although the resulting SWE anomalies in the northwestern U.S. are consistent between simulations and observations, the reasons that cause them are different. In the observations, during the years of a weak La Niña, the anomalous atmospheric circulation transported a moist air mass to the northwestern U.S., which increased the precipitation and resulted in the above normal SWEs. For the simulations, drifted climate patterns resulted in strong cold northerlies prevailing and also blocking warm air from entering the northwestern U.S. from the North Pacific during the years of a La Niña event, which decreased the local surface temperature. Above normal SWEs in the model are caused by less snowmelt due to the colder climate. During the years of a weak El Niño event, observed dry anomalous easterlies and northeasterlies prevail in the northwestern U.S., weakening local

precipitation and leading to below normal SWE. Simulated anomalous southerlies and southeasterlies bring warmer air to the region, strengthening snow melt and resulting in below normal SWE. A strong El Niño results in negative 500 mb height anomalies located in the North Pacific and extending to the southwestern U.S. in both simulations and observations. This introduces air moisture from the Mexican Gulf and exaggerates precipitation, leading to the above normal SWE. However, below normal SWE in the southwestern U.S. is connected to local climate variability. Under climatological SST conditions, positive local precipitation anomalies in the fall can result in below normal snow in the southwestern U.S. The excess latent heat due to the positive precipitation anomalies is released into the atmosphere and can form a positive 500 mb height anomaly center in the fall, which continues through the winter without further external forces. This center transports the dry northwesterlies to the region and favors downward air motions, thereby reducing local precipitation and leading to the below normal SWE in the southwestern U.S.

6. CONCLUSIONS

This dissertation has several contributions to literature for hydro-climatological studies. The major conclusions for the development of the sophisticated SAST model and its evaluations are given in Chapter 2 and in Jin et al. (1999a, b), Sun et al. (1999), and Yang et al. (1999). The model performances in PILPS 2e are concluded in Chapter 3 and also in Jin et al. (2002), Bowling et al. (2002), and Nijssen et al. (2002). The applications of the SAST model in CCM3 are summarized in Chapters 4 and 5 and will also be addressed in two manuscripts that are in preparation for peer-reviewed journals. The general conclusions can be drawn as follows.

The development of the SAST land surface scheme and its off-line evaluations at several field sites with snow measurements indicate that the SAST model includes significant physical processes of snowpack and provides efficient computational skill (i.e., the three layers of snow and their configuration scheme), which makes the new land surface scheme better describing energy and water exchanges between the atmosphere and the land surface and suitable to be coupled with the global climate models. Introducing parameterization of subgrid heterogeneity into the snow model is proved a proper way of extending the point physical snow models such as SNTHERM to an areal model. Simulated snow depths agree well with observations and the variability of simulated snow surface temperature due to the diurnal thawing and refreezing indicate the necessity of representing the compaction mechanisms and two-phase (liquid and ice) components of snow into the SAST model. Except for high-frequency variations in

observed albedo, the modeled surface albedo as a function of snow age and subgrid fractional coverage of snow, soil and vegetation shows reasonable variations in most sites. However, because observed albedo data are rare and not very reliable, further adjustment of the model to match the observed albedo is needed.

In the PILPS 2e experiment, the SAST land-surface scheme was found difficult to accurately simulate the patterns and quantities of runoff resulted from heavy snowmelt in the Tome/Kalix River basins in high latitudes. It is because the model lacked the subsurface runoff mechanisms and the prescribed model parameters of vegetation and soil were different from the values recommended by the PILPS 2e description. After model modification in runoff formulations and the calibration of the model parameters, the capability of runoff prediction is improved substantially and the model validation results in the PILPS 2e experiments are consistent and reasonably well. However, it is found that the calibrated parameters and many modeled variables (such as soil moisture) are diverse from the results of other PILPS 2e models, which indicates that without sufficient observed data to determine the real physical properties and processes in the basin, the calibrated results could be highly “model dependent”.

Using the coupled CCM3-SAST model, the results show that snow depths are greatly overestimated over the Rocky Mountains while surface temperature is underestimated. To study the reasons and impacts of these biases, the satellite remotely sensed snow data are assimilated into the land-surface scheme over the Rocky Mountains. After the assimilation of the remote-sensing data, the Rocky Mountains are covered with less snow, which greatly alleviates the cold bias over the Rocky Mountains

in the model by decreasing surface albedo, snow melt, and surface evaporation. The effects of changing snow amount and land-surface albedo occur mainly during winter and spring, and surface evaporation reaches its maximum influence after the snow duration. The albedo of the land surface with satellite snow cover only has a mild change because of the large vegetation coverage in the Rocky Mountains. Hence, the increase in surface temperature is mainly attributed to the less energy spending on snowmelt during the snow season. The lessened snowpack in the region reduces the soil moisture. The drier soil in summer suppresses evaporation, thereby resulting in a warmer surface. The weakened evaporation causes a smaller cloud fraction and increases incoming solar radiation and thus, the summer surface temperature. This feedback chain results in a drier and warmer atmospheric column and slight reduction of summer precipitation. Generally, the snow assimilation process over the Rocky Mountains exerts strong effects on surface temperature, but modest effects on precipitation in CCM3.

The tropical Pacific SST variability used to define an ENSO cycle is one of the most significant external forces affecting snow anomaly patterns in the western U.S. Based on observations and CCM3-SAST simulations in the northwestern U.S., the warm tropical Pacific phase of the ENSO is found to associate with diminished snowpack while its cool phase is related to enhanced snowpack. This relationship is largely determined by winter precipitation variability for observations in the northwestern U.S.; however, it relies heavily on the variations of temperature due to the biases in atmospheric patterns for the model output. In the southwestern U.S., positive snowpack anomalies for both

observations and simulations result from the strong warm phase of the ENSO, and negative ones are connected with exaggerated local precipitation in the fall.

APPENDIX A. Surface albedo formulation

Snow Surface Albedo

$$\alpha = 0.5(\alpha_{VIS} + \alpha_{IR}),$$

$$\alpha_{VIS} = 0.95 \cdot (1 - 0.2 f_{age}) + 0.4 \cdot f_z \cdot [1 - 0.95 \cdot (1 - 0.2 f_{age})],$$

$$\alpha_{IR} = 0.65 \cdot (1 - 0.5 f_{age}) + 0.4 \cdot f_z \cdot [1 - 0.65 \cdot (1 - 0.5 f_{age})],$$

Factor of snow age:

$$f_{age} = \tau_s / (1 + \tau_s),$$

$$\tau_s^{N+1} = (\tau_s^N + \Delta \tau_s) [1 - \max(0, P_o \gamma_t \Delta t) / 10],$$

$$\Delta \tau_s = (r_1 + r_2 + r_3) \Delta t / \tau_0,$$

$$\tau_0 = 1 \times 10^6 \text{ s}; r_1 = \exp[5000(\frac{1}{273.16} - \frac{1}{T_s})]; r_2 = (r_1)^{10} \leq 1; r_3 = \begin{cases} 0.01 & \text{Antarctica} \\ 0.30 & \text{elsewhere} \end{cases}$$

Factor of solar zenith angle:

$$f_z = \frac{1}{2} \left[\frac{3}{1 + 4 \cos \theta_z} - 1 \right], \text{ when } \cos \theta_z \geq 0.5, f_z = 0 \text{ and } \cos \theta_z = 0, f_z = 1.$$

APPENDIX B. Nomenclature

C_D = surface drag coefficient

C_l = specific heat of water (4217.7) ($\text{J kg}^{-1} \text{K}^{-1}$)

c_p = specific heat of air ($\text{J kg}^{-1} \text{K}^{-1}$)

C^R = liquid water-holding capacity

C_v = volumetric specific heat of snow ($\text{J m}^{-3}\text{K}^{-1}$)

d_s = grid-average snow depth (m)

E = rate of evaporation (upward is positive) ($\text{kg s}^{-1} \text{m}^{-2}$)

f_g = wetness factor (1.0 at snow surface)

f_{ice} = ice mass fraction

f_{snow} = snow fractional coverage

f_{veg} = vegetation fractional coverage (without snow)

H = heat content for unit volume of snow (Jm^{-3})

I_{sen} = sensible heat flux (Wm^{-2})

I_{prec} = heat flux of precipitation (Wm^{-2})

$I_s \downarrow$ = downwelling solar radiation (Wm^{-2})

K = snow thermal conductivity ($\text{Wm}^{-1}\text{K}^{-1}$)

K_{soil} = soil thermal conductivity ($\text{Wm}^{-1}\text{K}^{-1}$)

L_{AI} = leaf area index

L_{li} = the heat of fusion (J kg^{-1})

L_{lv} = latent heat of evaporation (J kg^{-1})

L_{net} = net long-wave radiation (W m^{-2})

m_{ice} = ice mass in a snow layer Δz (kg)

P_0 = the rate of precipitation (downward is positive) ($\text{kg m}^{-2}\text{s}^{-1}$)

P_s = snow load mass or overburden (kg m^{-2})

q_{af} = specific humidity in the canopy

q_{air} = air specific humidity above the canopy

q_{sn} = air specific humidity at the snow surface

R_f = liquid flow ($\text{kg m}^{-2}\text{s}^{-1}$)

R_{ough} = surface roughness (m)

R_s = net radiation at depth (Wm^{-2})

R_s^n = net surface solar radiation (W m^{-2})

t = time (s)

T_{af} = canopy air temperature (K)

T_{air} = air temperature (K)

T_f = leaf temperature (K)

T_p = precipitation temperature (K)

T_{sn} = snow surface temperature (K)

$U_{af} = V_a C_D^{1/2}$, wind speed within the canopy (m s^{-1})

V_a = wind speed at reference height (m s^{-1})

$W_C = 0.004 U_{af}$ (m s^{-1})

$$W_G = V_a C_D \text{ (m s}^{-1}\text{)}$$

z = vertical coordinate (upward positive)

α = snow surface albedo

$\gamma_i = \rho_s f_{ice}$ = partial density of ice (kg m^{-3})

$\gamma_l = \rho_s (1 - f_{ice})$ = partial density of liquid water (kg m^{-3})

ϵ_f = thermal emissivity of leaf

ϵ_{air} = thermal emissivity of air

σ = Stefan-Boltzmann constant ($5.669 \times 10^{-8} \text{ Wm}^{-2}\text{K}^{-4}$)

η_0 = snow viscosity coefficient at $T = 273.15 \text{ K}$ ($3.6 \times 10^6 \text{ kg s m}^{-2}$)

θ_z = solar zenith angle (radians)

ρ_a = density of air (kg m^{-3})

ρ_l = density of liquid water (1000 kg m^{-3})

ρ_s = density of snow (kg m^{-3})

Δt = time step (s)

Δz = snow node thickness (m)

APPENDIX C. Publications

- (1) **Jin, J., X.Gao, S.Sorooshian, 2002:** Impacts of model calibration on high-latitude land-surface processes: PILPS phase 2e calibration/validation experiments. Submitted to *Global and Planetary Change*.
- (2) **Bowling, L.C., D.P. Lettenmaier, B. Nijssen, P.L. Graham, D. Clark, M.E. Maayar, R. Essery, S. Goers, F. Habets, B.V. Hurk, J. Jin, D. Kahan, D. Lohmann, S. Mahanama, D. Mocko, O. Nasonova, P. Samuelsson, A.B. Shmakin, K. Takata, D. Verseghy, P.V. Viterbo, X. Ma, Y.K. Xue and Z. Yang, 2002:** Simulation of high latitude hydrological processes in the Torne-Kalix basin: PILPS phase 2e 1: Experiment description and summary intercomparison. Submitted to *Global and Planetary Change*.
- (3) **Nijssen, B., D.P. Lettenmaier, Bowling, L.C., P.L. Graham, D. Clark, M.E. Maayar, R. Essery, S. Goers, F. Habets, B.V. Hurk, J. Jin, D. Kahan, D. Lohmann, S. Mahanama, D. Mocko, O. Nasonova, P. Samuelsson, A.B. Shmakin, K. Takata, D. Verseghy, P.V. Viterbo, X. Ma, Y.K. Xue and Z. Yang, 2002:** Simulation of high latitude hydrological processes in the Torne-Kalix basin: PILPS phase 2e 2: Comparison of model results with observations. Submitted to *Global and Planetary Change*.
- (4) **Jin, J., X. Gao, Z. Yang, R. C. Bales, S. Sorooshian, R. E. Dickinson, S. Sun, and G. Wu, 1999a:** Comparative analyses of physically based snowmelt models for climate simulations. *J. Climate*, 12, 2643-2657.
- (5) **Jin, J., X. Gao, Z. Yang, R. C. Bales, S. Sorooshian, R. E. Dickinson, S. Sun, and G. Wu, 1999b:** One-dimensional snow water and energy balance model for vegetated surfaces. *Hydrological Processes*, 13, 2467-2482.
- (6) **Yang, Z.-L., R.E. Dickinson, A.N. Hahmann, G.-Y. Niu, M. Shaikh, X. Gao, R.C. Bales, S. Sorooshian, and J. Jin, 1999:** Simulation of snow mass and extent in general circulation models, *Hydrological Processes*, 13, 2097-2113.
- (7) **Sun, S.F., J. Jin, and Y. Xue, 1999:** A simple Snow-Atmosphere-Soil Transfer (SAST) Model. *J. Geophys. Res.*, 104 (D16), 19 587- 19 597.

REFERENCES

- Anderson, E.A., 1976: A point energy and mass balance model of a snow cover. Office of Hydrology, National Weather Service.
- Barnston, A.G., and R.E. Livezey, 1987: Classification, seasonality, and persistence of low-frequency atmospheric circulation patterns. *Mon. Wea. Rev.*, **115**, 1083-1126.
- Bonan, G.B., 1996: A Land Surface Model (LSM version 1.0) for Ecological, Hydrological, and Atmospheric Studies: Technical Description and User's Guide. NCAR Technical Note, NCAR/TN-417+STR, Boulder, Colorado, 150 p.
- Bonan, G.B., 1998: The land surface climatology of the NCAR land surface model coupled to the NCAR Community Climate Model. *J. Climate*, **11**, 1307-1326.
- Berry, J.A., 1998: Personal communication.
- Bohr, G.S., and E. Aguado, 2001: Use of April 1 SWE measurements as estimates of peak seasonal snowpack and total cold-season precipitation. *Water Resour. Res.*, **37**, 51-60.
- Bowling, L.C., D.P. Lettenmaier, B. Nijssen, P.L. Graham, D. Clark, M.E. Maayar, R. Essery, S. Goers, F. Habets, B.V. Hurk, J. Jin, D. Kahan, D. Lohmann, S. Mahanama, D. Mocko, O. Nasonova, P. Samuelsson, A.B. Shmakin, K. Takata, D. Verseghy, P.V. Viterbo, X. Ma, Y.K. Xue and Z. Yang, 2002: Simulation of high latitude hydrological processes in the Torne-Kalix basin: PILPS phase 2e 1: Experiment description and summary intercomparison. Submitted to *Global and Planetary Change*.
- Brun, E., P. David, M. Sudul, and G. Brunot, 1992: A numerical model to simulate snow cover stratigraphy for operational avalanche forecasting. *J. Glaciol.*, **38**(128), 13-22.
- California Department of Water Resources (CDWR), 1988: Update to the California Water Plan. Bulletin 160-98, Sacramento, California.
- Campbell, G.S., 1974: A simple method for determining unsaturated conductivity from moisture retention data, *Soil Science*, **117**, 311-314.
- Cayan, D.R., 1996: Interannual climate variability and snowpack in the western United States. *J. Climate*, **9**, 928-948.
- Cayan, D.R., and J.O. Roads, 1984: Local relationships between United States west coast precipitation and monthly mean circulation parameters. *Mon. Weather Rev.*, **112**, 1276-1282.

Cess, R.D., and coauthors, 1991: Interpretation of snow-climate feedback as produced by 17 general circulation models. *Science*, **253**, 888-892.

Clapp, R.B. and G.M. Hornberger, 1978: Empirical equations for some soil hydraulic properties, *Water Resour. Res.*, **20**, 682-690.

Chang, A.T.C., J. L. Foster, and D. K. Hall, 1990: Satellite estimates of Northern Hemisphere snow volume. *Rem. Sens. Lett.*, **11**, 167-172.

Changnon, D., T.B. Mckee, and N.J. Doesken, 1993: Annual snowpack patterns across the Rockies: Long-term trends and associated 500-mb synoptic patterns. *Mon. Wea. Rev.*, **212**, 633-647.

Cohen, J., 1994: Snow cover and climate. *Weather*, **49**, 150-156.

Cohen, J. and Rind, D., 1991: The effect of snow cover on the climate. *J. Climate*, **4**, 689-706.

Chen, M., R. E. Dickinson, X. Zeng, and A. N. Hahmann, 1996: Comparison of precipitation observed over the continental United States to that simulated by a climate model. *J. Climate*, **9**, 2233-2249.

Clapp, R.B. and G.M. Hornberger, 1978: Empirical equations for some soil hydraulic properties, *Water Resour. Res.*, **20**, 682-690.

Clark, M.P., M.C. Serreze, and G.J. McCabe, 2001: The historical effect of El Nino and La Nina events on the seasonal evolution of the montane snowpack in the Columbia and Colorado River basins. *Water Resour. Res.*, **37**, 741-756.

Coughlan, J. and S.W. Running, 1994: First results of BOREAS modeling exercise #1 for workshop at Prince Albert, Saskatchewan, 23-25 July 1994. Appendix A, 13-18.

Cosby, B.J., G.M. Hornberger, R.B. Clapp, and T.R. Ginn, 1984: A statistical exploration of the relationship of soil moisture characteristics to the physical properties of soil, *Water Resour. Res.*, **14**, 601-604.

Dai, Y., X. Zeng, R. E. Dickinson, I. Baker, G. Bonan, M. Bosilovich, S. Denning, P. Dirmeyer, P. Houser, G. Niu, K. Oleson, C. A. Schlosser, and Z.-L. Yang, 2001: The common land model (CLM). Submitted to *Bull. Amer. Meteor. Soc.*

Dickinson, R.E., 1988: The force-restore model for surface temperatures and its generalization. *J. Climate*, **1**, 1086-1097.

Dickinson, R.E., A. Henderson-Sellers, and P.J. Kennedy, 1993: Biosphere Atmosphere Transfer Scheme (BATS) Version 1e as Coupled to the NCAR Community Climate Model. NCAR Technical Note, NCAR/TN-387+STR, 72 pp. [Available from NCAR, P.O. Box 3000, Boulder, CO 80307-3000.]

Douville, H., J.-F. Royer, and J.-F. Mahfouf, 1995: A new snow parameterization for the Meteo-France climate model. part I: validation in stand-alone experiments. *Climate Dyn.*, **12**, 21-35.

Duan, Q., S. Sorooshian, and V. Gupta, 1992: Effective and efficient global optimization for conceptual rainfall runoff models, *Water Resour. Res.*, **28**, 1015-1031.

el-Ashry, M., and D. Gibbons, 1988: *Water and Arid Lands of the Western United States*, Cambridge Univ. Press, New York.

Eric, M., 1998: Personal communication.

FAO, 1995: The digital soil map of the world, version 3.5, Food and Agricultural Organization, Rome, Italy.

Foster, J. L., A.T.C. Chang, and D.K. Hall, 1987: Remote sensing of snow, *Eos Trans. AGU*, **68**, 681-684.

Foster, J. L., R. D. Davy, 1988: *Global snow depth climatology*. USAF publication USAFETAC/TN-88/006, Scott Air Force Base, Illinois.

Foster, J. L., G. Liston, R. Koster, R. Essery, H. Behr, L. Dumenil, D. Verseghy, S. Thompson, D. Pollard, J. Cohen, 1996: Snow cover and snow mass intercomparisons of general circulation models and remotely sensed datasets. *J. Climate*, **9**, 409-426.

Frei, A., D.A. Robinson, 1998: Evaluation of snow extent and its variability in the atmospheric model intercomparison project. *J. Geophys. Res.*, **103** 8859-8871.

Gao, X., S. Sorooshian, and V.K. Gupta, 1996: Sensitivity analysis of the biosphere-atmosphere transfer scheme. *J. Geophys. Res.*, **101**(D3), 7279-7289.

Gao, X. and S. Sorooshian, 1994: A stochastic precipitation disaggregation scheme for GCM application", *J. Climate*, **7**(2), 238-247.

Gerakis, A., 1999: A computer program for soil textural classification, *Soil Sci. Am. J.*, **63**(4).

Giorgi, F., B. Hewitson, J. Christensen, M. Hulme, H. von Storch, P. Whetton, R. Jones, L. Mearns, and C. Fu, 2001: Regional climate information-evaluation and projects. In:

Climate Change 2001: the scientific basis. Contribution of working group I to the third assessment report of the intergovernmental panel on climate change {Houghton, J.D., Y. Ding, D.J. Griggs, M. Noguer, P.J. van der Linden, X. Dai, K. Maskell, and C.A. Johnson (eds.)}. Cambridge University Press, Cambridge, United Kingdom and New York, NY, USA, 881.

Gleick, P.H. 1986. Methods for evaluating the regional hydrologic impacts of global climatic changes. *J. Hydrology*, **88**, 97-116.

Gleick, P.H. 1987a: The development and testing of a water-balance model for climate impact assessment: Modeling the Sacramento Basin. *Water Resour. Res.*, **23**, 1049-1061.

Gleick, P.H. 1987b: Regional hydrologic consequences of increases in atmospheric carbon dioxide and other trace gases. *Climatic Change*, **10**(2), 137-161.

Grant, L.O., and A.M. Kahan, 1974: Weather modification for augmenting orographic precipitation. *Weather and Climate Modification*, W.N. Ness, Ed., John Wiley and Sons, 282-317.

Gray, D.M., and D.H. Male, 1981: *Handbook of Snow*. Pergamon Press, New York.

Groisman, P., T.R. Karl, and R.W. Knight, 1994: Observed impact of snow cover on the heat balance and the rise of continental spring temperatures. *Science*, **263**, 198-200.

Hahmann, A.N and R.E. Dickinson, 2000: A fine-mesh land approach for general circulation model and its impact on regional climate, *J. Climate*, **14**, 1634-1646.

Hahn, D.G. and J. Shukla, 1976: An apparent relationship between Eurasian snow cover and Indian monsoon rainfall. *J. Atmos. Sci.*, **33**, 2461-2462.

Hamlet, A.F. and D.P. Lettenmaier. 1999. Effects of climate change on hydrology and water resources objectives in the Columbia River basin. *J. American Water Resources Association*, **35**, 1597-1624.

Hardy, J.P., R.E. Davis, R. Jordan, X. Li, C. Woodcock, W. Ni, and J.C. McKenzie, 1997: Snow ablation modeling at the stand scale in a boreal jack pine forest, *J. Geophys. Res.* **102**, 29397-29405.

Horel, J.D., and J.M. Wallace, 1981: Planetary scale atmospheric phenomena associated with the Southern Oscillation. *Mon. Wea. Rev.*, **109**, 813-829.

Hoskins, B.J., and D.J. Karoly, 1981: The steady linear response of a spheric atmosphere to thermal and orographic forcing. *J. Atmos. Sci.*, **38**, 1179-1196.

- Hulme, M., Osborn, T.J., and T.C. Johns, 1998: Precipitation sensitivity to global warming: Comparison of observations with HadCM2 simulations. *Geophys. Res. Letts.*, **25**, 3379-3382.
- Jin, J., X. Gao, Z. Yang, R. C. Bales, S. Sorooshian, R.E. Dickinson, S. Sun, and G. Wu, 1999a: One-dimensional snow water and energy balance model for vegetated surfaces. *Hydrological Processes*, **13**, 2467-2482.
- Jin, J., X. Gao, Z. Yang, R. C. Bales, S. Sorooshian, R.E. Dickinson, S. Sun, and G. Wu, 1999b: Comparative analyses of physically based snowmelt models for climate simulations. *J. Climate*, **12**, 2643-2657.
- Jones, P.D., T.J. Osborn, and K.R. Briffa, 1997: Estimating sampling errors in large-scale temperature averages. *J. Climate*, **10**, 2548-2568.
- Jordan, R., 1991: A one-dimensional temperature model for a snow cover. U.S. Army Corps of Engineers, Cold Regions Research and Engineering Laboratory, Special Report 91-16, 49 p.
- Keil, J.T., J.J. Hack, G.B. Bonan, B.A. Boville, B.P. Briegleb, D.L. Williamson, and P.J. Rasch, 1996: Description of the NCAR Community Climate Model (CCM3). NCAR Tech. Note, NCAR/TN-420+STR, 152 pp. [Available from National Center for Atmospheric Research, Boulder, CO 80307].
- Klein, W.H., 1985: Space and time variations in specifying monthly mean surface temperature from the 700mb height field. *Mon. Wea. Rev.*, **113**, 227-290.
- Kondo, J. and T. Yamazaki, 1990: A prediction model for snowmelt, snow surface temperature and freezing depth using a heat balance method. *J. Appl. Meteor.*, **29**, 375-384.
- Kripalani, R. H., and A. Kulkarni, 1999: Climatology and variability of historical Soviet snow depth data: Some new perspective in snow-Indian monsoon teleconnections. *Climate Dyn.*, **15**, 475-489.
- LaChapelle, E.R., 1969: *Properties of Snow*. Prepared for Hydrologic Systems course presented by College of Forest Resources, Nov. 17-18, University of Washington, Seattle, 21 pp.
- Lamb, H.H., 1972: Climate: Present, past and future. Vol.I. *Fundamentals and climate now*. Methuen, London, 613pp.

- Lau, N.-C., and M.J. Nath, 1994: A modeling study of relative roles of tropical and extratropical SST anomalies in the variability of the global atmosphere-ocean system. *J. Climate*, **7**, 1184-1207.
- Lau, N.-C., and M.J. Nath, 1996: The role of the "atmospheric bridge" in linking tropical Pacific ENSO events to extratropical SST anomalies. *J. Climate*, **9**, 2036-2057.
- Lau, N.-C., and M.J. Nath, 2001: Impact of ENSO on SST variability in the North Pacific and North Atlantic: Seasonal dependence and role of extratropical sea air coupling. *J. Climate*, **14**, 2846-2866.
- Leese, J.A., 1997: Major Activities Plan for 1998, 1999 and Outlook for 2000 for the GEWEX Continental-Scale International Project (GCIP), IGPO Publication Series, No. 26, Silver Spring, Maryland.
- Legates, D. R. and C. J. Willmott (1990a) Mean Seasonal and Spatial Variability Global Surface Air Temperature. *Theoretical and Applied Climatology* , **41**, 11-21.
- Legates, D. R. and C. J. Willmott(1990b) Mean Seasonal and Spatial Variability in Gauge-Corrected, Global Precipitation. *Int. J. Climatology*, **10**, 111-127.
- Li, X., A.H. Strahler, and C.R. Woodcock, 1995: A hybrid geometric optical-radiative transfer approach for modeling albedo and directional reflectance of discontinuous canopies, *IEEE Trans. on Geoscience and Remote Sensing*, **33**(2), 466-480.
- Loth, B., H.-F. Graf, and J.M. Oberhuber, 1993: Snow cover model for global climate simulations. *J. Geophys. Res.*, **98**, 10451-10464.
- Lynch-Stieglitz, M., 1994: The development and validation of a simple snow model for GISS GCM. *J. Climate*, **7**, 1842-1855.
- Marshall, S., J.O. Roads, and G. Glatzmaier, 1994: Snow hydrology in a general circulation model. *J. Climate*, **7**, 1251-1269.
- McAvaney, B., C. Covey, S. Joussame, V. Kattsov, A. Kitoh, W. Ogana, A. J. Pitman, A. J. Weaver, R. A. Wood, and Z.-C. Zhao, 2001: Model evaluation. In *Climate Change 2001: The Scientific Basis. Contribution of Working Group I to the Third Assessment Report of the Intercontinental Panel on Climate Change*, J. T. Houghton, Y. Ding, D. J. Griggs, M. Noguer, P. J. van der Linden, X. Dai, K. Maskell, and C. A. Johnson, Eds, Cambridge Univeristy Press, United Kingdom and New York, NY, USA, 471-524.
- McCabe, G.J. and D.M. Wolock, 1999: General-circulation-model simulations of future snowpack in the western United States. *J. American Water Resources Association*, **35**(6), 1473-1484.

- McCabe, G.J., and D.R. Legates, 1995: Relationships between 700 hPa height anomalies and 1 April snowpack accumulations in the western USA. *Int. J. Climatology*, **15**, 517-530.
- McCabe, G.J., and M.D. Dettinger, 1999: Decadal variations in the strength of ENSO teleconnections with precipitation in the western United States. *Int. J. Climatology*, **19**, 1399-1410.
- McCabe, G.J., and M.D. Dettinger, 2002: Primary modes and predictability of year-to-year snowpack variations in the western United States from teleconnections with Pacific Ocean climate. *J. Hydrometeorology*, **3**, 13-25.
- McFadden, J.D. and Ragotzkie R.A., 1967: Climatological significance of albedo in central Canada. *J. Geophys. Res.*, **72**, 1135-1143.
- Mitchell, K., P. Houser, E. Wood, J. Schaake, D. Tarpley, D. Lettenmaier, W. Higgins, C. Marshall, D. Lohmann, M. Ek, B. Cosgrove, J. Entin, Q. Duan, R. Pink, A. Robock, F. Habets, and K. Vinnikov, 1999: GCIP land data assimilation system (LDAS) project now underway, *GEWEX News*, **9**(3), 3-6.
- Morris, E. A., 1982: Sensitivity of the European hydrological system snow models. *Hydrological Aspects of Alpine and High Mountain Areas*, Proceedings of the Exeter Symposium, IHAS Publ no 138, 221-231.
- Myneni, R.B., R.R. Nemani, and S.W. Running, 1997: Estimation of global leaf area index and absorbed PAR using radiative transfer model, 1980-1993, *J. Climate.*, **14**, 1790-1808.
- Namias, J., 1964: Seasonal persistence and recurrence of blocking during 1958-1960. *Tellus*, **16**, 394-407.
- Namias, J., 1985: Some empirical evidence for the influence of snow cover on temperature and precipitation. *Mon. Wea. Rev.*, **113**, 1542-1553.
- Nijssen, B., D.P. Lettenmaier, Bowling, L.C., P.L. Graham, D. Clark, M.E. Maayar, R. Essery, S. Goers, F. Habets, B.V. Hurk, J. Jin, D. Kahan, D. Lohmann, S. Mahanama, D. Mocko, O. Nasonova, P. Samuelsson, A.B. Shmakin, K. Takata, D. Verseghy, P.V. Viterbo, X. Ma, Y.K. Xue and Z. Yang, 2002: Simulation of high latitude hydrological processes in the Torne-Kalix basin: PILPS phase 2e 2: Comparison of model results with observations. Submitted to *Global and Planetary Change*.
- Nijssen, B., R. Schnur, and D.P. Lettenmaier, 2001: Global retrospective estimation of soil moisture using the VIC land surface model, 1980-1993, *J. Climate.*, **14**, 1790-1808.

- Niu, G.-Y. and Z.-L. Yang, 2001: Versatile Integrator of Surface and Atmosphere processes (VISA) and its calibration in PILPS phase 2e, submitted to *Global and Planetary Change*:
- Oki, T., T. Nishimura, and P. Dirmeyer, 1999: Assessment of Annual Runoff from land surface models using total runoff integrating pathways (TRIP), *J. Meteor. Soc. Japan*, **77**, 235-255.
- Palmer, P.L., 1988: The SCS snow survey water supply forecasting program: Current operations and future directions. *Proc. Western Snow Conf.*, Kalispell, MT, 43-51.
- Panagoulia, D. and G. Dimou, 1996: Sensitivities of groundwater-streamflow interactions to global climate change. *Hydrological Sciences J.*, **41**, 781-796.
- Pitman, A.J., M. Zhao, and C.E. Desborough, 1999: Investigating the sensitivity of a land surface scheme's simulation of soil wetness and evaporation to spatial and temporal leaf area index variability within the global soil wetness project, *J. Meteor. Soc. Japan*, **77**, 281-290.
- Pollard, D. and S.L. Thompson, 1995: Use of a land-surface-transfer scheme (LSX) in a global climate model: the response to doubling stomatal resistance. *Global and Planetary Change*, **10**, 129-161.
- Rawls, W.J., D.L. Brakensiek, K.E. Saxton, 1982: Estimation of soil water properties, *Trans, ASAE*, **25**(5), 131-1320.
- Rhodes, S.L., D. Ely, and J.A. Dracup, 1984: Climate and the Colorado River: The limits of management, *Bull. Am. Meteorol. Soc.*, **65**, 682-691.
- Sardeshmukh, P.D., and B.J. Hoskins, 1988: The generation of global rotational flow by steady idealized tropical divergence. *J. Atmos. Sci.*, **45**, 1228-1252.
- Serreze, M.C., M.P. Clark, R.L. Armstrong, D.A. McGinnis, and R.S. Pulwarty, 1999: Characteristics of western U.S. snowpack from SNOTEL data. *Water Resour. Res.*, **35**, 2145-2160.
- Solley, W.R., R. Pierce, and H.A. Perlman. 1998. Estimated Use of Water in the United States in 1995. U.S. Geological Survey Circular 1200. Denver, CO.
- Sorooshian, S., Q. Duan, and V. K., Gupta, 1993: Calibration of rainfall-runoff models: Application of global optimization to the Sacramento soil moisture accounting model. *Water Resour. Res.*, **29**, 1185-1994.

Sun, S.F., J. Jin, and Y. Xue, 1999: A simple Snow-Atmosphere-Soil Transfer (SAST) Model. *J. Geophys. Res.*, **104**(D16), 19 587- 19 597.

Tarboton, D.G. and C.H. Luce, 1996: Utah Energy Balance Snow Accumulation and Melt Model (UEB). Computer model technical description and user's guide, Utah Water Research Laboratory and USDA Forest Service Intermountain Research Station.

Trenberth, K. E., 1999: Atmospheric moisture recycling: Role of advection and local evaporation. *J. Climate*, **12**, 1368-1381.

Trenberth, K. E., 1997: The definition of El Nino. *Bull. Amer. Meteor. Soc.*, **78**, 2771-2777.

Verseghy, D.L., 1991: CLASS --A Canadian Land Surface Scheme for GCMs. part I: soil model. *Int. J. Climatol.*, **11**, 111-133.

Viterbo, P., and A. K. Betts, 1999: Impact on ECMWF forecasts of changes to the albedo of the boreal forests in the presence of snow. *J. Geophys. Res.*, **104** (D22), 27803-27810.

Walland, D.J. and I. Simmonds, 1996: Sub-grid-scale topography and the simulation of Northern Hemisphere snow cover. *Int. J. Climatol.*, **16**, 961-982.

Wagner, A.J., 1973: The influence of average snow depth on monthly mean temperature anomaly. *Mon. Wea. Rev.*, **101**, 624-626.

Wallace J. M., C. Smith, and Q. Jiang, 1990: Spatial patterns of atmosphere-ocean interaction in the northern winter. *J. Climate*, **3**, 990-998.

Walsh, J.E. and Ross, B., 1988: Sensitivity of 30 day dynamical forecasts to continental snow cover. *J. Climate*, **1**, 739-754.

Way, J., R. Zimmermann, E. Rignot, K. McDonald, and R. Oren, 1997: Winter and spring thaw as observed with imaging radar at BOREAS. *J. Geophys. Res.*, **102**, D24, 29673-29648.

WCRP, 1999: Report of the GEWEX/ACSYS workshop on cold regions hydrological modeling, Quebec City, Canada, 25-27 August 1998, WCRP Informal Report No.13, 1999

Wu, G.-X., J. -S. Xue, Z. -Z. Wang, H. Liu, A. -G. He, and Y.-C. Zhao, 1995: The impacts of the snow-melt timing of the Tibetan Plateau on the seasonal variation in Southern China. *Gansu Meteorology*(in Chinese), **13**(1), 1-8.

Yang, Z.-L., R.E. Dickinson, A. Robock, and K.Y. Vinnikov, 1997: Validation of the snow sub-model of the Biosphere-Atmosphere Transfer Scheme with Russian snow cover and meteorological observational data. *J. Climate*, **10**, 353-373.

Yeh, T.-C., R. T. Wetherald, and S. Manabe, 1983: A model study of the short-term climate and hydrologic effects of sudden snow-cover removal. *Mon. Wea. Rev.*, **111**, 1013-1024.

Yen, Y.C., 1965: Heat transfer characteristics of naturally compacted snow. U.S. Army Cold Regions Research and Engineering Laboratory, Research Report 166, Hanover, NH, 9 pp.

Zeng, X., R.E. Dickinson, A. Walker, M. Shaikh, R.S. DeFries, and J. Qi, 2000: Derivation and evaluation of global 1-km fractional vegetation cover data for land modeling. *J. Appl. Meteor.*, **39**, 826-839.